DOCTORAL THESIS

SHIBAURA INSTITUTE OF TECHNOLOGY

Advancing Hybrid Vertical Axis Wind Turbines: Computational, Experimental, and Smart Technology Innovations for Wind Energy Optimization

2025/September

Elysa Nensy Irawan

ACKNOWLEDGEMENTS

The completion of this dissertation is the result of the support, guidance, and encouragement from many individuals and institutions. I am deeply grateful to everyone who has contributed to this research journey, whether through academic mentorship, technical assistance, or personal encouragement.

First and foremost, I would like to express my deepest gratitude to my academic advisor, Prof. Goro Fujita, for his invaluable guidance, encouragement, and unwavering support throughout this research. His insightful advice and constructive feedback have been instrumental in shaping the direction and quality of this thesis.

I would like to express my gratitude to Prof. Ken-Ichiro Yamashita from Meisei University for his role as another supervisor, offering valuable insights and engaging in thought-provoking discussions that have enriched my research. His expertise and guidance have been invaluable in refining the scope and depth of my work.

I am also profoundly grateful to the faculty members and researchers at Shibaura Institute of Technology, Power System Laboratory, for providing me with the necessary resources, technical expertise, and research facilities to conduct my experiments. Their generous support and collaboration have significantly contributed to the success of this study. Additionally, I would like to extend my sincere appreciation to Shibaura Institute of Technology for awarding me a scholarship, which has been essential in enabling me to pursue my doctoral research.

I would also like to express my sincere gratitude to Universitas Pendidikan Indonesia for providing me with the opportunity to pursue my Ph.D. studies. This opportunity has been instrumental in shaping my academic and professional growth.

A special thanks to Mr. Maulana Putra from BMKG Indonesia for providing access to wind speed data in Indonesia. This crucial data has greatly contributed to the accuracy and relevance of my research findings.

My heartfelt gratitude extends to my family and friends, whose unwavering belief in my capabilities has been a constant source of motivation. Their patience, sacrifices, and emotional support have given me the strength to persevere during challenging times. I am truly fortunate to have such a loving and supportive circle of people around me.

Furthermore, I would also like to acknowledge my fellow graduate students and colleagues at Shibaura Institute of Technology, whose friendship, collaboration, and stimulating discussions have made this academic journey an enjoyable and enriching experience. Their diverse perspectives and constructive feedback have helped broaden my understanding and approach to research.

Finally, I extend my gratitude to all those who, in one way or another, contributed to the completion of this dissertation. This achievement would not have been possible without their collective support and encouragement.

Once again, my deepest thanks to everyone who has supported me throughout this journey.

Elysa Nensy Irawan

September 2025

ABSTRACT

Wind energy has emerged as a crucial component of sustainable power generation, with vertical axis wind turbines (VAWTs) gaining attention due to their adaptability to varying wind conditions. However, optimizing VAWTs for improved efficiency and self-starting capability remains a challenge. To address this, this dissertation investigates the optimization of hybrid Savonius-Darrieus VAWTs using computational fluid dynamics (CFD) and experimental validation to enhance performance across different operational conditions.

Building upon the fundamental principles of hybrid Savonius-Darrieus wind turbines, a comprehensive analysis is conducted to understand their advantages and challenges. The combination of Savonius (drag-based) and Darrieus (lift-based) designs aims to improve self-starting capability while maintaining a high-power coefficient. CFD simulations indicate that a hybrid turbine with an optimal rotor radius ratio of 0.5 achieves a 12.5% increase in power coefficient compared to a conventional Darrieus turbine. These findings establish the groundwork for further optimization and experimental validation.

To validate the numerical findings, an experimental study on hybrid wind turbine performance at high tip speed ratios (TSR) is conducted. Various design modifications, including blade shape, rotor radius ratio, and solidity, are tested to assess their impact on power output. The results demonstrate that a hybrid model with a Savonius overlap ratio of 0.2 improves self-starting torque by 18.7% while maintaining a power coefficient (C_P) of 0.34 at TSR 1.6. This confirms the effectiveness of hybrid configurations in improving turbine startup and performance.

Building on these results, an innovative smart hybrid VAWT with an adaptive rotor-switching mechanism is introduced. This system transitions between hybrid and pure Darrieus modes based on wind conditions, optimizing efficiency at different TSRs. Experimental validation confirms that the smart hybrid turbine achieves a 21% increase in efficiency at higher TSRs compared to conventional hybrid designs, ensuring stable performance under fluctuating wind speeds. These advancements further highlight the potential of adaptive wind turbine systems in enhancing energy capture.

To assess real-world applicability, the wind energy potential of the proposed smart hybrid turbine in Banjarmasin, Indonesia, is evaluated. The study analyzes local wind conditions and

turbine adaptability, demonstrating a 347.46% higher power output than conventional hybrid models. These results emphasize the feasibility of deploying hybrid VAWTs in regions with variable wind patterns.

Overall, this research advances the design and implementation of hybrid Savonius-Darrieus VAWTs, contributing to the development of more efficient and adaptable wind energy solutions. By integrating computational analysis with experimental validation, the findings provide a robust foundation for future improvements. Future work will focus on refining control strategies and exploring advanced materials to further enhance turbine performance and sustainability.

Keywords: *Computational fluid dynamics, Darrieus, moment coefficient, power coefficient, Savonius, smart hybrid, tip speed ratio, vertical axis wind turbines, wind power potential, wind speed*.

CONTENTS

LIST OF FIGURES

LIST OF TABLES

LIST OF ABREVIATIONS AND SYMBOLS

AI	=	Artificial Intelligence	P	=	Mechanical power of the wind turbine [W]
Δs	=	First layer thickness [m]	p	=	Pressure [Pa]
Δt	=	Time step [s]	P_{copper}	=	Copper loss [W]
∇	=	Gradient differential operator	P_{iron}	=	Iron loss [W]
∇^2	=	Laplacian operator	P_O	=	Output power [W]
A	=	Rotor swept area [m^2]	P_T	=	Wind turbine extracted power [W]
a	=	Induction factor	PIV	=	Particle Image Velocimetry
B	=	Magnetic flux density [T]	Pr	=	Prandtl number
BMKG	=	Badan Meteorologi, Klimatolog, dan Geofisika	PVC	=	Polyvinyl Chloride
c	=	Airfoil chord length [m]	P_w	=	Wind Power [W]
C_n	=	Normal coefficient	r	=	Radius/ length of the rotor blade [m]
C_P	=	Power coefficient	R	=	Resistance [Ω]
C_t	=	Tangential coefficient	$\frac{R_S}{R_D}$	=	Rotor Radius Ratio
C_d	=	Drag coefficient	Re	=	Reynolds number
CFD	=	Computational Fluid Dynamic	SCADA	=	Supervisory Control And Data Acquisition
C_l	=	Lift coeffcient	SST	=	Single Stream Tube
C_M	=	Moment coefficient	T	=	Thrust
CO_2	=	Carbon dioxide	t	=	Time [s]
D	=	Drag forces [N]	TSR	=	Tip Speed Ratio
DC	=	Dirrect Current	U	=	Air velocity at the disc [m/s]
dF_D	=	Incremental drag force	u	=	Mean wind speeds [m/s]
dF_L	=	Incremental lift force	U_{rel}	=	Velocity of the relative wind [m/s]
dF_N	=	Incremental normal force	v	=	Wind velocity [m/s]
dF_T	=	Incremental tangential force	ϑ	=	Air's kinematic viscosity [m^2/s]
DMST	=	Double Multiple Stream Tube	V	=	Free stream velocity [m/s]
dQ	=	Differential torque	V_a	=	Induced velocity [m/s]
e	=	Overlap	V_{ua}	=	Upwind velocity [m/s]
f	=	Frequency of magnetic reversals [Hz]	V_{ad}	=	Downwind velocity [m/s]
h	=	Height [m]			

HAWT	=	Horizontal Axis Wind Turbines	V_e	=	Velocity at the downstream equilibrium [m/s]
I	=	Current [A]	V_G	=	Generator voltage [V]
I_G	=	Generator current [A]	V_M	=	Motor voltage [V]
I_M	=	Motor current [A]	V_O	=	Output voltage [V]
I_O	=	Output current [A]	VAWT	=	Vertical Axis Wind Turbine
IEA	=	International Energy Agency	V_R	=	Relative airflow velocity [m/s]
IoT	=	Internet of Things	WTRS	=	Wind Turbine Research Station
IRENA	=	International Renewable Energy Agency	α	=	Angle of attack [°]
K_c	=	Copper loss coefficient	β	=	Pitch angle [°]
k_e	=	Eddy current loss coefficient	γ	=	Shear exponent
K_f	=	Friction loss coefficient	δ	=	Blade height ratio
k_h	=	Hysteresis loss coefficient	θ	=	Azimuth angle [°]
K_i	=	Iron loss coefficient	λ	=	Tip speed ratio
L	=	Lift forces [N]	μ	=	Air's dynamic viscosity [N·s/m²]
l	=	Airfoil span [m]	ρ	=	Air density [kg/m^3]
l	=	Length scale [m]	σ	=	Solidity
$\frac{L}{D}$	=	Lift-to-drag ratio	τ	=	Torque [N.m]
$\dot{m}$	=	Mass flow rate [kg/s]	τ_{wall}	=	Wall shear stress [Pa]
MPPT	=	Maximum Power Point Tracking	φ	=	Angle of the relative wind [°]
MST	=	Multiple Stream Tube	ω	=	Rotor speed [rad/s]
NACA	=	National Advisory Committee for Aeronautics	Ω	=	Tangential speed [m/s]
NREL	=	National Renewable Energy Laboratory			

CHAPTER 1
INTRODUCTION

1.1 RESEARCH BACKGROUND

The environmental effects of carbon dioxide contribute to global warming, primarily driven by the excessive use of fossil fuels [1]. Nearly 80% of the world's population resides in nations that rely on importing fossil fuels. According to the International Energy Agency (IEA), the transportation sector contributes to approximately one-third of the total global carbon dioxide emissions [2]. Consequently, the rising carbon footprint from transportation places a substantial strain on the global environment [3]. This situation raises significant concerns regarding both economic stability and sustainable development [4].

Worldwide, there has been a transition toward using renewable energy sources to address environmental crises caused by global warming [5]. Renewable energy has become a crucial solution in tackling these challenges, providing a cleaner and more sustainable substitute for fossil fuels [6]. According to the International Renewable Energy Agency (IRENA), renewable sources could and should supply 90% of the world's energy by 2050 [7]. Unlike traditional energy sources, renewable options like solar, wind, hydro, and biomass depend on naturally replenished resources that emit little carbon [8]. The widespread use of renewable energy technologies can drastically cut global reliance on fossil fuels, helping to lower CO_2 emissions and other harmful pollutants that drive climate change [9].

Among various renewable energy sources, wind power stands out as the only one with a well-established technology, strong commercial potential, and widespread use in large-scale electricity generation [10]. Wind power technology has been extensively researched and developed over the past several decades, making it one of the most mature and reliable renewable energy sources available today. Compared to other renewables such as solar, hydro, and biomass, wind energy has demonstrated remarkable efficiency and scalability, making it a preferred choice for many countries striving to reduce carbon emissions and transition toward sustainable energy systems. Wind power technology saw significant growth during the oil crisis of the 1970s but later declined [11]. However, in the past decade, supportive policies for the wind industry in various countries have driven rapid market expansion, leading to substantial advancements in wind turbine technology growth as shown in Fig. 1.1.

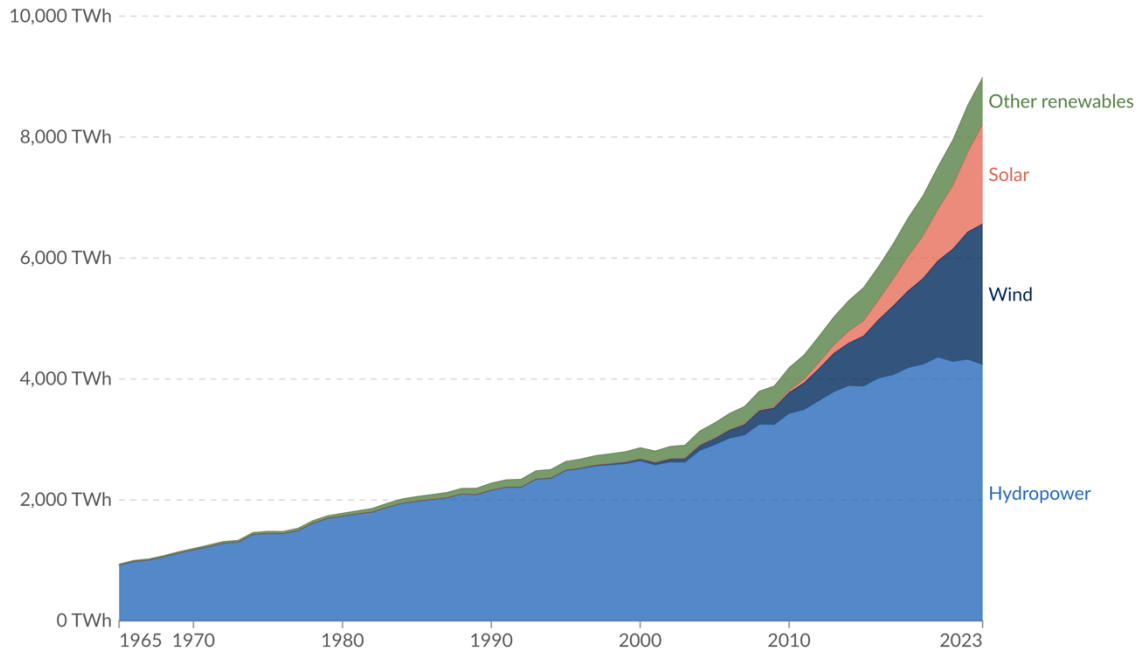

Fig. 1.1 Renewable Energy Growth [7]

Vertical axis wind turbines (VAWTs) offer an attractive alternative to horizontal axis wind turbines (HAWTs) due to their ability to operate efficiently at low wind speeds [12]. With a rotor axis oriented vertically, these turbines do not require alignment with the wind, making them particularly beneficial for locations with frequently changing wind directions [13]. VAWTs operate much more quietly than horizontal axis wind turbines, making them ideal for residential and urban environments [14]. However, their efficiency is lower than HAWTs due to the extra drag generated as the blades move against the wind [15]. Thus, advancements in design and control mechanisms are necessary to improve the performance of VAWTs.

An advanced solution involves the creation of Smart VAWT, a vertical axis wind turbine integrated with cutting-edge technologies like sensors, the Internet of Things (IoT), and AI-driven control algorithms. Research by S. Le Fouest and K. Mulleners [16] utilized a genetic algorithm optimizer in conjunction with automated experiments on a scaled-down turbine model to identify optimal pitching kinematics under both design and off-design operating conditions. The optimized pitching strategy resulted in a significant increase in power coefficient, achieving a 20% improvement compared to the fixed-pitch baseline. This enhancement was consistent across a range of tip-speed ratios, demonstrating the robustness of the optimized control strategy.

Additionally, the study found that the optimized pitch motion reduced torque ripple by 15%, contributing to smoother turbine operation and potentially extending the lifespan of turbine components. These findings underscore the potential of advanced control strategies in improving the efficiency and operational stability of vertical-axis wind turbines.

Another study by Harmjanz et al. [17] evaluated start-up, active flow control, and overspeed protection strategies for VAWTs. Results showed that optimized pitch control increased power extraction by 20% and reduced torque ripple by 15%, leading to smoother operation. Advanced braking enhanced overspeed protection without efficiency loss. Supervisory control and data acquisition (SCADA) and electrical control systems further improved monitoring and energy capture, highlighting the importance of advanced control methods for reliable VAWT performance.

Eriksson et al. [18] introduced a novel control method for a fixed-pitch, variable-speed vertical-axis wind turbine (VAWT). Using the turbine as an anemometer, the system estimated wind speed based on absorbed power and rotational speed, enabling tip speed ratio (TSR) control without external wind measurements. The control method adjusted DC voltage to maintain an optimal TSR, enhancing efficiency. Experimental results from a 200 kW VAWT (40 m height, 13 m radius, 33 rpm nominal speed) demonstrated effective regulation, with measured power closely matching theoretical predictions. The system achieved stable operation across varying wind speeds, confirming the feasibility of TSR-based control for improved wind energy conversion.

Another interesting study was performed by Hosseini and N. Goudarzi [19]. They examined a hybrid wind turbine that combined a Savonius-type Bach rotor for high start-up torque and a 3-bladed H-Darrieus turbine for improved efficiency. They used computational fluid dynamics (CFD) and control algorithms to analyze an electromagnetic switch mechanism that disengaged the Bach rotor at higher tip speed ratios (TSR) to reduce drag. Results showed that the hybrid turbine achieved a power coefficient over 40% and operated efficiently up to TSR 6. The control algorithm successfully optimized turbine transitions, enhancing energy capture.

Based on previous research conducted by other scholars, this study aims to improve Smart VAWT by implementing a simpler method while maintaining optimal performance. This technology enables VAWT to adapt to environmental conditions in real-time, improving energy

conversion efficiency and extending the operational lifespan of the system. With this innovation, Smart VAWT is expected to become a more efficient, reliable, and sustainable renewable energy solution.

1.2 PROBLEM STATEMENT

Wind energy has emerged as a significant renewable energy source, with vertical axis wind turbines (VAWTs) gaining attention due to their adaptability to urban environments and variable wind conditions. However, despite their advantages, VAWTs still face several critical challenges that hinder their widespread adoption and efficiency improvement.

One of the primary challenges of VAWTs, particularly Darrieus turbines, is their poor self-starting capability. Unlike horizontal axis wind turbines (HAWTs), which can efficiently capture wind energy even at lower speeds, Darrieus-type VAWTs require a minimum wind speed threshold to initiate rotation. This limitation reduces their operational effectiveness in regions with low or inconsistent wind speeds. Although Savonius turbines offer better self-starting capabilities, their lower aerodynamic efficiency results in reduced power output.

Another major issue is the optimization of hybrid Savonius-Darrieus VAWTs. While the combination of drag-based Savonius and lift-based Darrieus designs aims to enhance self-starting capability while maintaining a high-power coefficient, existing designs still fall short in achieving optimal efficiency. The interaction between the two turbine types creates aerodynamic losses, and the ideal design parameters such as rotor radius ratio, solidity, and blade configurations are yet to be fully determined.

Furthermore, conventional hybrid VAWT designs lack adaptability to changing wind conditions. In fluctuating wind environments, the fixed configuration of hybrid turbines limits their efficiency across different wind speeds and tip speed ratios (TSRs). This necessitates the development of an adaptive mechanism that can switch between hybrid and pure Darrieus modes based on real-time wind conditions.

Moreover, limited experimental validation of computational findings presents another challenge. While computational fluid dynamics (CFD) simulations provide valuable insights into turbine performance, real-world testing is essential to confirm the feasibility of proposed designs. The gap between numerical predictions and experimental results often leads to discrepancies in performance estimations. In this research, a systematic approach is adopted to

address discrepancies between theoretical predictions and the actual performance of the hybrid Savonius-Darrieus vertical axis wind turbine (VAWT).

The first step involves **experimental validation** of the CFD outcomes. Key performance parameters such as power coefficient (C_P), moment coefficient (C_M), and self-starting torque are empirically tested using scaled turbine prototypes. CFD simulations predicted a 12.5% increase in C_P compared to conventional Darrieus turbines. This is corroborated by experimental results, where a hybrid model with a Savonius overlap ratio of 0.2 demonstrated an 18.7% improvement in starting torque and a C_P of 0.34 at a tip speed ratio (TSR) of 1.6.

To ensure consistency, the turbine geometry used in simulations is accurately reproduced in physical form. **Experiments** are conducted in a controlled environment using an open-loop wind tunnel, minimizing external variables such as atmospheric turbulence and pressure fluctuation factors which are not typically captured in CFD models.

Furthermore, the development of the **Smart Hybrid VAWT** with an adaptive rotor-switching mechanism reinforced the link between theoretical modeling and practical implementation. This intelligent system, designed to switch between hybrid and single Darrieus modes in real-time based on wind conditions, achieved a 21% increase in efficiency at higher TSRs, in line with simulation forecasts. Through this comprehensive approach, the gap between numerical simulations and experimental findings can be effectively narrowed, leading to more robust, efficient, and field-ready wind turbine designs.

Lastly, the feasibility of implementing hybrid VAWTs in specific geographic regions, such as Banjarmasin, Indonesia, remains uncertain. Despite the potential for wind energy utilization in this region, the lack of detailed assessments on wind conditions, energy capture efficiency, and economic viability poses a significant barrier to deployment.

Given these challenges, this research aims to address the fundamental issues of hybrid Savonius-Darrieus VAWT design by optimizing key parameters, developing an adaptive smart switching mechanism, and conducting extensive experimental validation. By overcoming these limitations, the study seeks to contribute to the advancement of more efficient and adaptable wind energy solutions for sustainable power generation.

1.3 DIFFERENCES BETWEEN CFD AND EXPERIMENT APPROACH

In this research, both numerical and experimental approaches were employed to investigate and optimize the performance of hybrid Savonius-Darrieus vertical axis wind turbines. Although both methods serve the common objective of evaluating turbine behavior, there are fundamental differences in their methodology, assumptions, and outcomes as shown in Table 1.1. This section outlines the key differences and the role of each approach within the research.

Table 1.1 Key Differences

Aspect	Numerical Analysis (CFD)	Experimental Testing
Environment	Simulated, ideal conditions	Physical, real-world conditions
Input Variables	Fully controlled, no disturbances	Subject to physical variabilities
Assumptions	Steady-state flow, uniform wind, no losses	Includes friction, electrical losses, etc.
Output Parameters	C_P, C_M, velocity/pressure contours	Torque, RPM, voltage, power output
Losses Considered	Not modeled	Included and measured
Flow Visualization	Full field visualization (CFD post-processing)	Limited to external observation

The numerical analysis, conducted using computational fluid dynamics (CFD), was utilized as the first step in the design and optimization process. Through systematic simulation studies, several design parameters such as rotor radius ratio, Savonius overlap ratio, and blade solidity were evaluated to determine their effects on turbine performance indicators such as power coefficient (C_P) and moment coefficient (C_M). These simulations provided a cost-effective and controlled environment for identifying the most promising configurations under idealized flow conditions.

Once the optimal design parameters were identified through CFD analysis, the selected configurations were implemented in the form of physical prototype models and subjected to experimental testing. The objective of this stage was to verify the real-world applicability of the numerically optimized models by evaluating their actual performance under controlled

laboratory conditions. The experiments focused on measuring torque, rotational speed, and electrical output, while also accounting for real-world losses such as friction and generator inefficiencies that are typically neglected in simulation.

1.4 STUDY CONTRIBUTIONS

The study contributions of this thesis are organized by chapters and are supported by their respective publications:

1.4.1 Chapter 2: Advancing Hybrid Savonius-Darrieus Wind Turbine Performance through Computational Fluid Dynamics

This chapter contributes to the field of renewable energy research by utilizing computational fluid dynamics (CFD) to optimize the aerodynamic performance of hybrid Savonius-Darrieus vertical axis wind turbines (VAWTs). The study introduces a novel approach to improving self-starting capabilities while maintaining a high-power coefficient, which is crucial for enhancing the efficiency of VAWTs in urban and low-wind-speed environments. The CFD simulations demonstrate a 12.5% increase in power coefficient compared to conventional Darrieus turbines, providing valuable insights for future wind turbine designs. These findings have significant technological implications, offering a foundation for the development of more efficient hybrid wind turbine models that can operate effectively in varying wind conditions. Environmentally, the study supports the broader adoption of small-scale wind energy solutions, reducing dependency on fossil fuels and lowering carbon emissions.

Journal:

[J.1] E. N. Irawan, S. Sitompul, K.-I. Yamashita, and G. Fujita, “The Effect of Rotor Radius Ratio on The Performance of Hybrid Vertical Axis Wind Turbine Savonius-Darrieus NREL S809,” Journal of Energy and Power Technology, vol. 5, no. 1, Art. no. 1, Jan. 2023, doi: 10.21926/jept.2301001.

[J.2] E. N. Irawan et al., “Analyzing the growth and trends of vertical axis wind turbine research: Insight from a bibliometric study,” Journal of Mechatronics, Electrical Power, and Vehicular Technology, vol. 14, no. 1, Art. no. 1, Jul. 2023, doi: 10.14203/j.mev.2023.v14.55-61.

International Conference Proceedings:

[C.1] E. N. Irawan, S. Sitompul, K.-I. Yamashita, and G. Fujita, "Computational Fluid Dynamics Analysis on the Improvement of Hybrid Savonius-Darrieus NREL S809 at Various Fluid Flows," in 2023 4th International Conference on High Voltage Engineering and Power Systems (ICHVEPS), Aug. 2023, pp. 389–394. doi: 10.1109/ICHVEPS58902.2023.10257308.

[C.5] E. Nensy Irawan, K.-I. Yamashita, and G. Fujita, "Comparison of Non-Overlap and Overlap Savonius Wind Turbines in the Physics Aspect Using Computational Fluid Dynamics Method," J. Phys.: Conf. Ser., vol. 2780, no. 1, p. 012031, Jun. 2024, doi: 10.1088/1742-6596/2780/1/012031.

1.4.2 Chapter 3: Experimental Validation of Hybrid Wind Turbine Performance at High Tip Speed Ratios

The experimental findings in this chapter provide critical advancements in the practical application of hybrid wind turbines. By testing various design modifications, such as blade shape, rotor radius ratio, and solidity, the study confirms that a hybrid model with a Savonius overlap ratio of 0.2 enhances self-starting torque by 18.7% while maintaining a power coefficient of 0.34 at a tip speed ratio (TSR) of 1.6. From a technological perspective, these results validate the feasibility of hybrid turbine configurations for real-world applications, ensuring stability and efficiency under diverse wind conditions. In the broader context of renewable energy, this research contributes to the ongoing development of small and medium-scale wind energy systems, promoting their integration into decentralized power generation. By optimizing turbine performance, the study supports a cleaner and more sustainable energy future, reducing greenhouse gas emissions and enhancing energy security.

International Conference Proceedings:

[C.2] E. N. Irawan et al., "Development of a Simple Open-Loop Wind Tunnel for Small-Scale Wind Turbine Testing," in The 18th Southeast Asian Technical University Consortium (SEATUC), Feb. 2024, pp. 38–42.

[C.3] E. N. Irawan, K. Shibuya, K.-I. Yamashita, and G. Fujita, "Enhancing Vertical Axis Wind Turbine Performance Investigation at Low Wind Speed Using Electrical

Approach," in 2024 8th International Conference on Green Energy and Applications (ICGEA), Mar. 2024, pp. 1–5. doi: 10.1109/ICGEA60749.2024.10561142.

[C.4] E. N. Irawan, K. Shibuya, K.-I. Yamashita, and G. Fujita, "Solidity Effects on Small Hybrid Savonius-Darrieus Wind Turbine Performance: Experimental Analysis with NREL S809 Airfoil," in 2024 10th International Conference on Applied System Innovation (ICASI), Apr. 2024, pp. 163–165. doi: 10.1109/ICASI60819.2024.10547931.

1.4.3 Chapter 4: Innovations in Smart Hybrid Vertical Axis Wind Turbines for Adaptive Energy Capture

This chapter introduces a groundbreaking innovation in wind turbine technology by developing a Smart Hybrid VAWT with an adaptive rotor-switching mechanism. This intelligent system enables the turbine to transition between hybrid and pure Darrieus modes based on real-time wind conditions, maximizing efficiency at different TSRs. The experimental validation confirms a 21% increase in efficiency at higher TSRs compared to conventional hybrid models, highlighting the potential of smart wind energy systems. Technologically, this study advances the concept of adaptive renewable energy solutions, integrating control algorithms and automated adjustments to optimize power output. From an environmental perspective, the smart hybrid turbine enhances energy capture efficiency, making wind energy a more reliable and scalable solution for urban and rural settings. By improving energy conversion rates, this research contributes to reducing reliance on non-renewable energy sources, further mitigating climate change impacts.

Journal:

[J.3] E. N. Irawan, K. Shibuya, K.-I. Yamashita, and G. Fujita, "Unlocking the power of the wind: Innovations in smart hybrid vertical axis wind turbines," International Journal of Renewable Energy Development, vol. 13, no. 5, pp. 974–981, Sep. 2024, doi: 10.61435/ijred.2024.60354.

International Conference Proceedings:

[C.6] E. N. Irawan, K.-I. Yamashita, and G. Fujita, “A Novel Rotor Switching Theory for Optimizing Small Vertical Axis Wind Turbine Performance: Insights from Experimental Study,” in 2024 International Conference on Electrical, Computer and Energy Technologies (ICECET, Jul. 2024, pp. 1–5. doi: 10.1109/ICECET61485.2024.10698090.

1.4.4 Chapter 5: Assessing Wind Energy Potential with Smart Hybrid VAWTs in Banjarmasin, Indonesia

This chapter extends the research to real-world applications by evaluating the feasibility and effectiveness of Smart Hybrid VAWTs in Banjarmasin, Indonesia. The study demonstrates that the proposed turbine model generates 347.46% more power than conventional hybrid designs. These results provide strong evidence for the practical implementation of smart hybrid wind turbines in regions with variable wind conditions. From a technological standpoint, the study refines turbine control strategies, optimizing energy generation in low-wind-speed areas. Environmentally, this research emphasizes the role of wind energy in reducing fossil fuel consumption, lowering carbon footprints, and supporting regional energy independence. By demonstrating the viability of adaptive wind energy systems, this chapter contributes to the global transition toward sustainable and renewable energy infrastructure.

International Conference Proceedings:

[C.7] E. N. Irawan, M. Miyagawa, M. Putra, K.-I. Yamashita, and G. Fujita, “Estimating Wind Energy Potential: Advanced Smart Hybrid VAWT Analysis in Banjarmasin, Indonesia,” in 2024 6th International Conference on Power Engineering and Renewable Energy (ICPERE), Nov. 2024, pp. 1–6. doi: 10.1109/ICPERE63447.2024.10845584.

1.5 THESIS OUTLINE

1.5.1 Chapter 1: Introduction

The first chapter provides a comprehensive introduction to the research by outlining the background, motivation, and significance of the study. It discusses the growing need for sustainable energy solutions, particularly wind energy, and highlights the challenges faced in

optimizing vertical axis wind turbines (VAWTs). The chapter presents the problem statement, emphasizing the inefficiencies in self-starting capability and energy conversion of hybrid Savonius-Darrieus wind turbines. The research objectives are clearly defined, focusing on improving turbine performance through computational and experimental methods. Additionally, this chapter explains the study's scope and limitations, ensuring a well-structured research framework. It concludes with a brief outline of the thesis structure, providing a roadmap for the reader to understand the research flow.

1.5.2 Chapter 2: Unleashing the Potential of Hybrid Savonius-Darrieus Vertical Axis Wind Turbines – A Computational Fluid Dynamics (CFD) Approach

This chapter delves into the theoretical and computational foundations of hybrid wind turbine design. It begins by introducing the fundamental principles of wind energy and comparing horizontal axis wind turbines (HAWTs) with VAWTs, justifying the choice of a hybrid Savonius-Darrieus configuration. The study then explores the use of computational fluid dynamics (CFD) to analyze turbine aerodynamics, detailing the simulation methodology, including preprocessing (model design and meshing), processing (boundary conditions and simulation setup), and validation of numerical results. The chapter presents key performance metrics, such as power coefficient improvements and optimized rotor radius ratios, demonstrating a 12.5% increase in efficiency compared to conventional designs. The discussion highlights how these computational insights contribute to developing more efficient wind turbines suitable for varying wind conditions.

1.5.3 Chapter 3: Hybrid Wind Turbine Testing in High Tip Speed Ratio Experimental Analysis

The third chapter shifts from computational studies to experimental validation, ensuring that theoretical improvements translate into practical performance gains. It introduces the importance of real-world testing and describes the experimental setup for assessing hybrid wind turbines at high tip speed ratios (TSRs). The chapter outlines key methodologies, including regenerative testing, iron loss assessments, and DC generator loss analysis. Through a series of controlled experiments, the study evaluates the impact of design modifications such as blade shape, rotor radius ratio, and solidity. The results confirm that a hybrid model with a Savonius overlap ratio of 0.2 enhances self-starting torque by 18.7% while maintaining a power coefficient of 0.34 at TSR 1.6. This chapter reinforces the reliability of hybrid wind turbine

configurations, demonstrating their viability for improving small and medium-scale wind energy systems.

1.5.4 Chapter 4: Innovations in Smart Hybrid Vertical Axis Wind Turbines

This chapter presents a major technological innovation: the development of a Smart Hybrid VAWT with an adaptive rotor-switching mechanism. The study introduces the concept of intelligent wind turbines that can dynamically transition between hybrid and pure Darrieus modes based on real-time wind conditions. The methodology focuses on designing and testing the control algorithms that govern this transition, ensuring optimal energy conversion at different TSRs. Experimental validation reveals a 21% efficiency improvement at higher TSRs compared to conventional hybrid models. The discussion underscores the potential of smart wind energy systems to enhance energy capture, reduce operational inefficiencies, and ensure stable performance under fluctuating wind conditions. By integrating automated control mechanisms, this chapter advances the state-of-the-art in wind turbine technology and paves the way for more adaptable and efficient renewable energy solutions.

1.5.5 Chapter 5: Estimating Wind Energy Potential – Advanced Smart Hybrid VAWT Analysis in Banjarmasin, Indonesia

Extending the study to real-world applications, this chapter evaluates the feasibility of deploying Smart Hybrid VAWTs in Banjarmasin, Indonesia. The chapter begins with an assessment of local wind power potential and analyze the challenges of harnessing wind energy in regions with highly variable wind speeds. The methodology outlines the adaptation of the turbine model to these conditions and the establishment of optimal rotor-switching intervals to maximize efficiency. Results demonstrate that the Smart Hybrid VAWT achieves 347.46% higher power output. These findings highlight the practical benefits of adaptive wind turbines in optimizing energy generation and promoting sustainable development in emerging markets. The discussion emphasizes the role of smart wind energy systems in reducing carbon footprints and supporting regional energy independence.

1.5.6 Chapter 6: Conclusion and Future Work

The final chapter summarizes the key findings of the research, reaffirming its contributions to wind turbine technology, computational analysis, and experimental validation. It revisits the research objectives, demonstrating how the integration of CFD, real-world testing, and smart control strategies has led to significant advancements in hybrid wind turbine

performance. The chapter also discusses broader implications, including how this study can influence future developments in renewable energy systems. Several recommendations for future work are provided, including the implementation of maximum power point tracking (MPPT), advanced aerodynamic optimization, AI-driven control strategies, and large-scale deployment. These suggestions aim to further enhance the adaptability, scalability, and efficiency of smart hybrid wind turbines in diverse environmental conditions, ensuring continued progress toward sustainable energy solutions.

1.6 STUDY LIMITATIONS

Despite the significant contributions of this research in optimizing hybrid Savonius-Darrieus vertical axis wind turbines (VAWTs), several limitations must be acknowledged.

A. **Computational Limitations –** The computational fluid dynamics (CFD) simulations used in this study rely on certain assumptions and ideal conditions, such as steady-state airflow and uniform wind speed distributions. In real-world scenarios, wind turbulence, gusts, and complex environmental interactions may affect turbine performance in ways not fully captured by the simulations. Additionally, computational constraints limit the resolution of mesh refinement, which could impact the accuracy of the numerical results.

B. **Experimental Constraints –** The experimental validation of the hybrid wind turbine was conducted under controlled laboratory conditions, which may not fully replicate the variability of natural wind conditions. Factors such as turbulence intensity, varying atmospheric pressure, and temperature fluctuations were not considered in the experimental setup. Additionally, the scale of the tested models was smaller than commercial-scale turbines, which may result in performance variations when applied to full-scale deployments.

C. **Material and Structural Considerations –** The study primarily focuses on aerodynamic optimization and does not extensively evaluate the impact of material selection, structural durability, and long-term wear and tear. Future research should incorporate advanced materials, fatigue testing, and structural stability assessments to ensure long-term reliability and operational efficiency.

D. **Control System Complexity –** While the Smart Hybrid VAWT introduces an adaptive rotor-switching mechanism, the study does not fully explore real-time wind sensing and

advanced control algorithms. The system currently relies on predefined switching intervals rather than AI-driven or machine-learning-based adjustments, which could further enhance efficiency. Future research should integrate more sophisticated control strategies to improve adaptability and responsiveness.

E. **Geographical and Climatic Limitations –** The wind energy potential assessment was conducted in Banjarmasin, Indonesia, and results are unlikely to be directly applicable to other regions with different wind profiles, altitudes, or seasonal variations. Additional studies are needed to evaluate performance under diverse environmental conditions, such as coastal, mountainous, and urban areas.

F. **Economic and Feasibility Analysis –** While the study focuses on performance improvements, it does not conduct a detailed cost-benefit analysis or economic feasibility study for large-scale implementation. Future research should assess production costs, maintenance requirements, and return on investment to determine the commercial viability of Smart Hybrid VAWTs.

REFERENCES

[1] N. Iqbal, K. R. Abbasi, R. Shinwari, W. Guangcai, M. Ahmad, and K. Tang, "Does exports diversification and environmental innovation achieve carbon neutrality target of OECD economies?," *Journal of Environmental Management*, vol. 291, p. 112648, Aug. 2021, doi: 10.1016/j.jenvman.2021.112648.

[2] "World Energy Outlook 2023 – Analysis," IEA. Accessed: Feb. 16, 2025. [Online]. Available: https://www.iea.org/reports/world-energy-outlook-2023

[3] S. A. Sarkodie, M. Y. Ahmed, and P. A. Owusu, "Advancing COP26 climate goals: Leveraging energy innovation, governance readiness, and socio-economic factors for enhanced climate resilience and sustainability," *Journal of Cleaner Production*, vol. 431, p. 139757, Dec. 2023, doi: 10.1016/j.jclepro.2023.139757.

[4] T. Martins, A. C. Barreto, F. M. Souza, and A. M. Souza, "Fossil fuels consumption and carbon dioxide emissions in G7 countries: Empirical evidence from ARDL bounds testing approach," *Environmental Pollution*, vol. 291, p. 118093, Dec. 2021, doi: 10.1016/j.envpol.2021.118093.

[5] T. Baležentis, D. Streimikiene, T. Zhang, and G. Liobikiene, "The role of bioenergy in greenhouse gas emission reduction in EU countries: An Environmental Kuznets Curve modelling," *Resources, Conservation and Recycling*, vol. 142, pp. 225–231, Mar. 2019, doi: 10.1016/j.resconrec.2018.12.019.

[6] D. K and L. N.h, “THE ROLE OF RENEWABLE ENERGY IN MITIGATING CLIMATE CHANGE,” *ShodhKosh: Journal of Visual and Performing Arts*, vol. 4, no. 1, Art. no. 1, Jun. 2023, doi: 10.29121/shodhkosh.v4.i1.2023.2786.

[7] M. Adaramola, *Climate Change and the Future of Sustainability: The Impact on Renewable Resources*. CRC Press, 2017.

[8] S. Fawzy, A. I. Osman, J. Doran, and D. W. Rooney, “Strategies for mitigation of climate change: a review,” *Environ Chem Lett*, vol. 18, no. 6, pp. 2069–2094, Nov. 2020, doi: 10.1007/s10311-020-01059-w.

[9] A. Maulida and Y. I. Masjud, “The Impact of Renewable Energy on Climate Change: A Literature Review,” *PACC*, vol. 1, no. 1, Feb. 2024, doi: 10.61511/pacc.v1i1.2024.621.

[10] G. M. Joselin Herbert, S. Iniyan, E. Sreevalsan, and S. Rajapandian, “A review of wind energy technologies,” *Renewable and Sustainable Energy Reviews*, vol. 11, no. 6, pp. 1117–1145, Aug. 2007, doi: 10.1016/j.rser.2005.08.004.

[11] B. Blocken, “50 years of Computational Wind Engineering: Past, present and future,” *Journal of Wind Engineering and Industrial Aerodynamics*, vol. 129, pp. 69–102, Jun. 2014, doi: 10.1016/j.jweia.2014.03.008.

[12] M. A. Al-Rawajfeh and M. R. Gomaa, “Comparison between horizontal and vertical axis wind turbine,” *International Journal of Applied Power Engineering (IJAPE)*, vol. 12, no. 1, Art. no. 1, Mar. 2023, doi: 10.11591/ijape.v12.i1.pp13-23.

[13] Z. Simic, J. G. Havelka, and M. Bozicevic Vrhovcak, “Small wind turbines – A unique segment of the wind power market,” *Renewable Energy*, vol. 50, pp. 1027–1036, Feb. 2013, doi: 10.1016/j.renene.2012.08.038.

[14] I. Khorsand, C. Kormos, E. G. MacDonald, and C. Crawford, “Wind energy in the city: An interurban comparison of social acceptance of wind energy projects,” *Energy Research & Social Science*, vol. 8, pp. 66–77, Jul. 2015, doi: 10.1016/j.erss.2015.04.008.

[15] N. A. Ahmed and M. Cameron, “The challenges and possible solutions of horizontal axis wind turbines as a clean energy solution for the future,” *Renewable and Sustainable Energy Reviews*, vol. 38, pp. 439–460, Oct. 2014, doi: 10.1016/j.rser.2014.06.004.

[16] S. Le Fouest and K. Mulleners, “Optimal blade pitch control for enhanced vertical-axis wind turbine performance,” *Nat Commun*, vol. 15, no. 1, p. 2770, Mar. 2024, doi: 10.1038/s41467-024-46988-0.

[17] J. F. Harmjanz, T. Westergaard, and D. T. Griffith, “Assessment of Control Methods for Vertical Axis Wind Turbines: Start-up, Active Flow Control, and Overspeed Control,” in *AIAA SCITECH 2023 Forum*, in AIAA SciTech Forum. , American Institute of Aeronautics and Astronautics, 2023. doi: 10.2514/6.2023-0612.

[18] S. Eriksson, J. Kjellin, and H. Bernhoff, “Tip speed ratio control of a 200 kW VAWT with synchronous generator and variable DC voltage,” *Energy Science & Engineering*, vol. 1, no. 3, pp. 135–143, 2013, doi: 10.1002/ese3.23.

[19] A. Hosseini and N. Goudarzi, “CFD and Control Analysis of a Smart Hybrid Vertical Axis Wind Turbine,” presented at the ASME 2018 Power Conference collocated with the ASME 2018 12th International Conference on Energy Sustainability and the ASME 2018 Nuclear Forum, American Society of Mechanical Engineers Digital Collection, Oct. 2018. doi: 10.1115/POWER2018-7488.

CHAPTER 2
UNLEASHING THE POTENTIAL OF HYBRID SAVONIUS-DARRIEUS VERTICAL AXIS WIND TURBINES: A COMPUTATIONAL FLUID DYNAMICS APPROACH

2.1 CHAPTER INTRODUCTION

Wind energy, a renewable resource, can be harnessed and converted into electrical energy using wind turbines [1]. These turbines are generally classified into two categories: horizontal axis wind turbines (HAWT) and vertical axis wind turbines (VAWT) [2]. HAWTs, which are more commonly seen in traditional wind farms, have blades that rotate around a horizontal axis [3]. In contrast, VAWTs, which have a vertical axis of rotation [4], are becoming increasingly popular due to their unique advantages [5].

According to research cited in [2], VAWTs offer several distinct advantages over their horizontal counterparts. For instance, VAWTs can operate effectively in turbulent and variable wind conditions, making them suitable for urban environments and locations where wind directions frequently change. Additionally, VAWTs typically require less maintenance and can be more accessible for repairs since the generator and other key components are located closer to the ground.

The two primary types of VAWTs are the Darrieus and Savonius rotors [6]. Each is designed with specific features to maximize efficiency and performance. The Savonius design operates on the principle of drag force [7], whereas the Darrieus turbine functions based on lift force [8]. Although Darrieus turbines achieve a higher power coefficient (C_P) compared to Savonius, they also require stronger winds to start rotating [9]. To capitalize on the advantages of both systems, many researchers develop hybrid turbines combining Savonius and Darrieus designs. The hybrid Savonius-Darrieus design does not significantly enhance the initial torque provided by the Savonius turbine, nor does it achieve the same power coefficient as the Darrieus turbine [10]. The overall performance of the hybrid turbine is affected by the interaction between the two turbine types.

A study by [9] explored improving the self-starting ability of Darrieus turbines by combining them with Savonius turbines. Computational fluid dynamics (CFD) simulations showed a 26.91% increase in power coefficient at a low tip speed ratio (TSR) of 1.45. However,

performance declined at higher TSRs due to the Savonius turbine's limitations. Adding front and side deflectors enhanced efficiency by 30% and 26% at an optimal TSR of 2.6, with the best results from a double deflector setup.

On the other hand, study by [11] examined the impact of adding pitch angles on the performance of a hybrid Savonius-Darrieus under varying wind speeds. The study used an experimental method with pitch angles ranging from 0º to 30º and varying wind speeds. Results showed that increasing the pitch angle affected the turbine's cut-in speed. The highest cut-in speed was 4.2 m/s at a 0º pitch, while the lowest was 3.8 m/s at a 30º pitch angle.

Another study by [12] investigated the performance of a hybrid Darrieus-Savonius by varying the Savonius blade height. Experiments conducted in a subsonic wind tunnel focused on the blade height ratio (δ) between the Savonius and Darrieus rotors. The results showed that a height ratio greater than unity (δ = 1.4) yielded the best performance, with a power coefficient of 0.20 and a moment coefficient (C_M) of 0.129. This represented a 48% increase in power and a 29% increase in torque compared to the Darrieus turbine alone, highlighting the importance of blade height ratio in turbine design.

In the research performed by [13], a novel hybrid vertical axis wind turbine with enhanced power efficiency and self-starting capability was introduced. The design combined an H-rotor with cambered blades inside and NACA0018 airfoil blades outside. Performance analysis showed that the proposed turbine achieved a maximum power coefficient of 0.486 at a tip speed ratio of 3, surpassing the H-rotor Darrieus (C_P = 0.42) and existing hybrid VAWT (C_P = 0.41). The turbine demonstrated self-starting ability at all azimuths and showed an 11%-13% improvement in performance metrics over a range of wind speeds.

A study by [14] developed a variable solidity Darrieus-type wind turbine (D-VAWT) to improve self-starting and aerodynamic performance. Simulations showed that higher solidity (σ) and lower moment of inertia enhanced self-starting. A D-VAWT with $\sigma \geq 0.417$ self-started in under 30 seconds at 7.9 m/s. It achieved a maximum power coefficient of 0.342 at an optimal tip speed ratio of 3.25, increasing maximum power output by 188%, from 53.42W to 100.39W, compared to a fixed solidity design.

Based on the aforementioned studies, numerous design parameters significantly influence the performance of hybrid Savonius-Darrieus turbines. Therefore, to achieve an optimal design, this chapter will conduct a CFD study to evaluate the performance of the hybrid Savonius-

Darrieus turbine. The analysis will focus on key design parameters such as the effect of Savonius overlap, rotor radius ratio, and solidity, with the aim of optimizing the turbine's performance.

2.2 FUNDAMENTAL OF THE WIND TURBINE

Wind energy generation relies on the capacity of harvesting energy from airflow [2]. Wind power measures the rate of kinetic energy extraction that can be described as the rate at which kinetic energy flows through airflow [15]. In general, wind turbines can be categorized into two main types: Horizontal axis wind turbines (HAWT) and vertical axis wind turbines (VAWT), with their fundamental designs depicted in Fig. 2.1 [16].

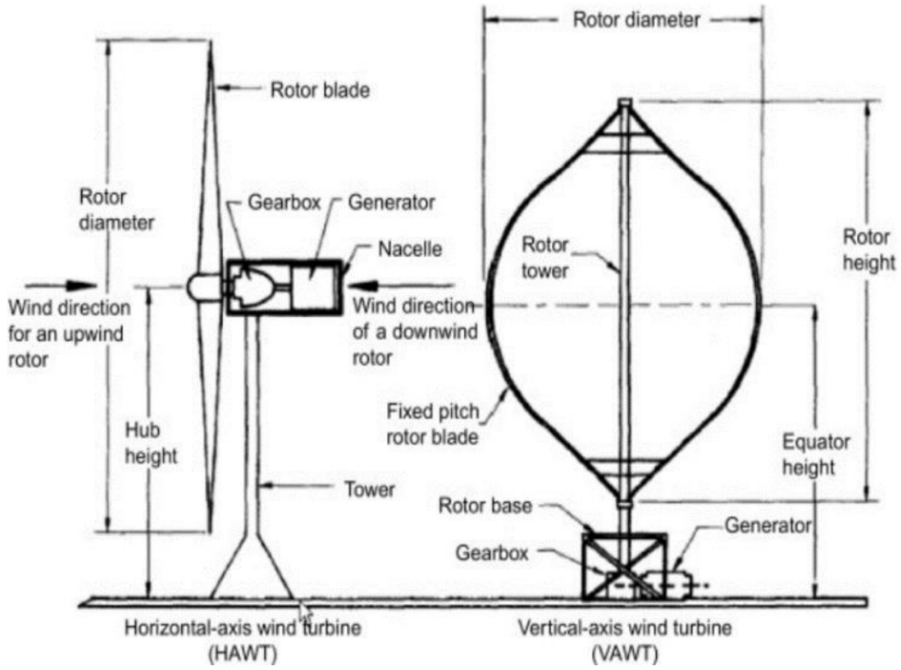

Fig. 2.1 HAWT and VAWT Fundamental Design [16]

Both types exhibit distinct advantages and disadvantages, as summarized in Table 2.1.

Table 2.1 Comparison of HAWT and VAWT [16]

Characteristics	HAWT	VAWT
Electrical energy	• Higher electric energy harvesting	• Produce up to 50% more electricity on an annual basis

Characteristics	HAWT	VAWT
	• Harvest more electric energy from a given amount of wind compared to VAWT.	versus conventional turbines with the same swept area.
Weight	• Heavier	• Lighter
Rotor orientation	• Horizontal	• Vertical
Wind direction	• Functions at specific wind direction (Not suitable for turbulent winds)	• Functions in all wind directions (Suitable for turbulent winds)
Wind speed range	• 6 m/s – 25 m/s	• 2 m/s – 65 m/s
Environmental impact	• Higher chance of bird collision • Higher noise	• Lower chance of bird collision • Lower noise
Starting function	• Higher starting torque • Self-starting	• Lower starting torque • Might require energy to initiate rotation
Variety [17]	• 2 bladed • 3 bladed	• Has two major types with many variations
Cost and construction [12]	• Higher	• Lower

One of the primary elements that directly influences a wind turbine's output power (P_w) is wind speed. Eq. (2.1) provides additional insight on this relationship [17].

$$P_w = \frac{1}{2}\rho A v^3 \tag{2.1}$$

Where ρ is the air's density [kg/m^3], v stands for wind velocity [m/s], and A for rotor swept area [m^2].

The performance of these turbines is often evaluated using a power coefficient (C_P) graph, which measures the efficiency of the turbine in converting wind energy into mechanical energy (P) as shown in Eq. (2.2) [18].

$$C_P = \frac{P}{P_w} \tag{2.2}$$

Fig. 2.2 illustrates the performance characteristics of different types of VAWTs, showcasing their respective C_P values under varying conditions [19]. Fig. 2.2 offers key insights into the performance characteristics of wind turbines. The blue curve represents the optimal efficiency

of horizontal axis wind turbines, while the other curves correspond to different types of vertical axis wind turbines.

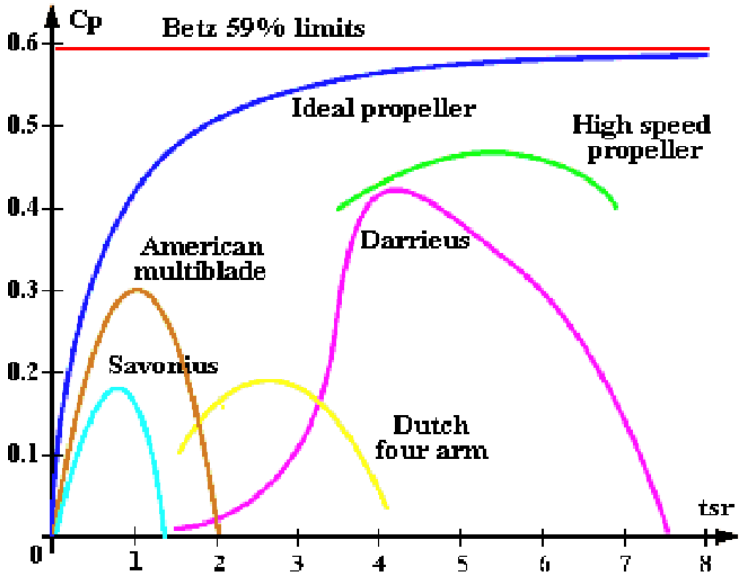

Fig. 2.2 Performance of the Various Type of VAWT [19]

German scientist Albert Betz established the "Betz Limit," or maximum efficiency of the optimal wind turbine rotor, in 1920. This limit states that no wind turbine can catch more than 59.3% of the wind energy that is available [20], but in reality, tip losses, boundary layer drags, wake, and less-than-ideal inflow circumstances cause the aerodynamic performance to decrease (C_{Pmax} = 0.593) [2].

The analysis is based on a control volume, where the boundaries are defined by the surface of a stream tube and two of its cross-sectional areas as shown in Fig. 2.3.

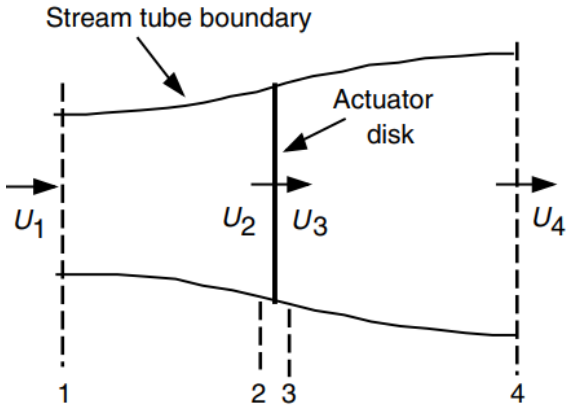

Fig. 2.3 Actuator Disc Model of a Wind Turbine

The following presumptions must be considered to reach this limit and guarantee that the disk functions as a drag device that lowers the stream velocity [21]:

(i) An actuator disc or fixed disc would take the role of a narrow rotor, drawing energy from the flowing stream.

(ii) A perfect scenario in which the wake has no rotational velocity.

(iii) There is no friction in the flow.

(iv) The general momentum theory now demonstrates that the disk performs as the following equations.

By applying the principle of conservation of linear momentum to the control volume that encompasses the entire system, the net force acting on the contents of the control volume can be determined. This net force is equal in magnitude but opposite in direction to the thrust T, which represents the force exerted by the wind on the wind turbine.

$$T = U_1(\rho AU)_1 - U_4(\rho AU)_4 \tag{2.3}$$

U represents the air velocity [m/s], with the subscripts denoting the specific values at the numbered cross-sections shown in Fig. 2.3.

For steady-state flow, $(\rho AU)_1 = (\rho AU)_4 = \dot{m}$, where $\dot{m}$ represents the mass flow rate. Therefore:

$$T = \dot{m}(U_1 - U_4) \tag{2.4}$$

Because the thrust force acts positively, the air velocity just after the rotor (U_4) decreases compared to the incoming free-stream velocity (U_1). Since no external work is added or removed from the flow before and after the turbine rotor, Bernoulli's equation can be applied separately to the flow regions before and after the actuator disc. Considering the stream tube section located upstream of the disc:

$$p_1 + \tfrac{1}{2}\rho {U_1}^2 = p_2 + \tfrac{1}{2}\rho {U_2}^2 \tag{2.5}$$

Within the stream tube section located downstream of the disc:

$$p_3 + \frac{1}{2}\rho U_3^2 = p_4 + \frac{1}{2}\rho U_4^2 \tag{2.6}$$

Thrust can alternatively be represented as the total net force resulting from the difference in forces acting on both sides of the actuator disc:

$$T = A_2(p_2 - p_3) \tag{2.7}$$

By solving for $(p_2 - p_3)$ from Eqs. (2.5) and (2.6) and then substituting the result into Eq. (2.7), the following expression is derived:

$$T = \frac{1}{2}\rho A_2(U_1^2 - U_4^2) \tag{2.8}$$

Using this simple model, the wind velocity at the rotor plane is calculated as the average of the wind speeds before and after the rotor.

$$U_2 = \frac{U_1+U_4}{2} \tag{2.9}$$

If the axial induction factor (a), is defined as the proportionate reduction in wind velocity from the free stream to the rotor plane, then

$$a = \frac{U_1-U_2}{U_1} \tag{2.10}$$

$$U_2 = U_1(1-a) \tag{2.11}$$

$$U_4 = U_1(1-2a) \tag{2.12}$$

The value $U_1 a$ is typically known as the induced velocity at the rotor plane, indicating that the wind velocity at the rotor results from a combination of the free-stream wind speed and this induced component. As the axial induction factor a grows from zero, the airflow slows increasingly behind the rotor. When a reaches 0.5, the wind speed immediately downstream of the rotor becomes zero, and beyond this point, the basic theoretical model ceases to be valid.

The output mechanical power (P) can be calculated as the product of the thrust force and the velocity at the rotor disc:

$$P = \frac{1}{2}\rho A_2(U_1^2 - U_4^2)U_2 = \frac{1}{2}\rho A_2 U_2(U_1+U_4)(U_1-U_4) \tag{2.13}$$

By replacing U_2 and U_4 using Eqs (2.11) and (2.12), the result is:

$$P = \frac{1}{2}\rho A U^3 4a(1-a)^2 \tag{2.14}$$

Here, the control volume area at the rotor (A_2), is substituted with A, the rotor's swept area, and the free-stream velocity (A_1) is replaced by U. The power coefficient is defined as:

$$C_P = \frac{P}{\frac{1}{2}\rho U^3 A} = \frac{\text{Rotor power}}{Power\ in\ the\ wind} \tag{2.15}$$

$$C_P = 4a(1-a)^2 \tag{2.16}$$

The extreme value of Eq. (2.16), which can be found as Eq. (2.17), yields the greatest value of the power coefficient, or C_P:

$$\frac{dC_P}{da} = 4(1-a)(1-3a) = 0 \tag{2.17}$$

An ideal rotor produces the most power when it is built and run so that the wind speed at the rotor is two-thirds of the free-stream wind speed. This indicates that the power coefficient reaches its maximum at 16/27. Wind turbines range in design and efficiency, resulting in varying optimal operating conditions. This section goes over the many types of turbines present.

2.2.1 Horizontal Axis Wind Turbine (HAWT)

Typically, horizontal axis turbines have their blades facing upwind instead of downwind from the supporting shaft, as shown in Fig. 2.4 [22].

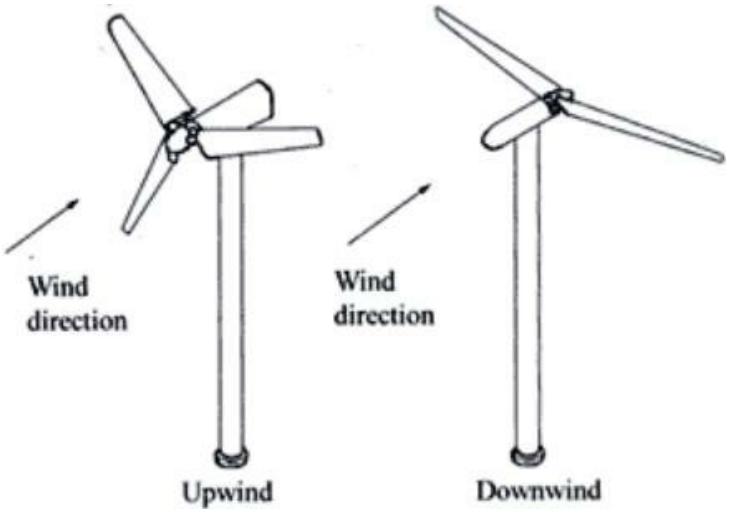

Fig. 2.4 Upwind vs Downwind HAWT [22]

Several terms are commonly used to describe the geometry and aerodynamic features of an airfoil, as illustrated in Fig. 2.5.

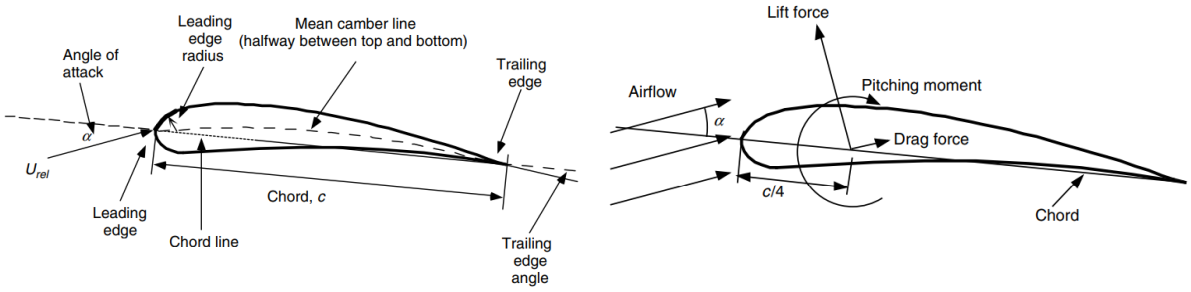

(a) (b)

Fig. 2.5 Airfoil Nomenclatur (a) and Forces (b)

The Reynolds number Eq. (2.18) expresses the Reynolds number of airflow across an airfoil [23].

$$Re = \frac{UL}{v} = \frac{\rho UL}{\mu} = \frac{\text{Inertial force}}{\text{Viscous force}} \tag{2.18}$$

U and ℓ represent a characteristic velocity [m/s] and length [m] that define the scale of the flow, while μ and υ represent air's dynamic [Ns/m^2] and kinematic viscosity [m^2/s], respectively.

Force and moment coefficients for flow around two-dimensional shapes are typically denoted using lowercase subscripts, such as C_d for the two-dimensional drag coefficient. These coefficients represent forces measured per unit span. The moment coefficient is a dimensionless parameter that represents the aerodynamic moment acting on the rotor, normalized by reference values. It is typically used to analyze and compare the performance and loading characteristics of wind turbine rotors. In contrast, lift and drag coefficients for three-dimensional bodies are usually written with uppercase subscripts, like C_D. In rotor design, two-dimensional coefficients are commonly used, obtained from wind tunnel testing over a range of angles of attack and Reynolds numbers. The two-dimensional lift coefficient (C_l) is defined as:

$$C_l = \frac{L/l}{\frac{1}{2}\rho U^2 c} = \frac{\text{Lift force/unit length}}{\text{Dynamic force/unit length}} \tag{2.19}$$

The drag coefficient for a two-dimensional flow is defined as:

$$C_d = \frac{D/l}{\frac{1}{2}\rho U^2 c} = \frac{\text{Drag force/unit length}}{\text{Dynamic force/unit length}} \tag{2.20}$$

The pitching moment coefficient for two-dimensional flow is given by:

$$C_M = \frac{M}{\frac{1}{2}\rho U^2 Ac} = \frac{\text{Pitching moment}}{\text{Dynamic moment}} \tag{2.21}$$

Here, ρ represents the air density, U is the velocity of the undisturbed (free stream) airflow, A refers to the projected area of the airfoil (calculated as chord × span), c is the chord length of the airfoil, and l denotes the span of the airfoil.

The forces acting on wind turbine blades can also be described in terms of lift and drag coefficients, along with the angle of attack. As illustrated in Fig. 2.6, this analysis treats the blade as being divided into N discrete sections (or elements). The following assumptions are applied:

- Each element operates independently, meaning there is no aerodynamic interaction or radial flow between sections.

- The aerodynamic forces on the blade are entirely determined by the lift and drag properties of the airfoil profile used in the blade design.

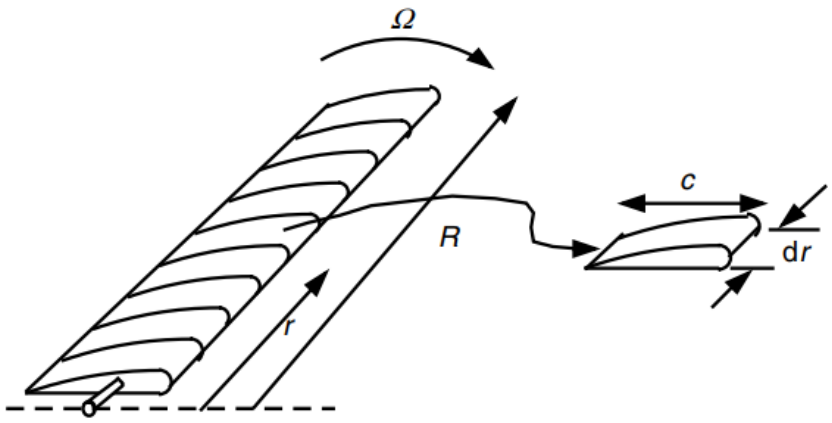

Fig. 2.6 Schematic of blade elements

When analyzing the forces on a blade section, it is important to note that the lift force acts perpendicular to the relative wind, while the drag force acts parallel to it. The relative wind itself is the vector combination of two velocities: the wind speed at the rotor plane, $U(1-a)$, where a is the axial induction factor, and the velocity caused by the blade's rotation. This rotational velocity includes the tangential speed of the blade section, Ωr, plus the induced angular velocity at the blades resulting from angular momentum conservation, which is $\omega r/2$.

$$\Omega r + (\omega/2)r = \Omega r + \Omega a' r = \Omega r(1 + a') \tag{2.22}$$

The overall flow scenario is illustrated in Fig. 2.7 (a), while Fig. 2.7 (b) shows the relationships between the various forces, angles, and velocities at the blade, viewed from above the blade tip. In this context:

- θ_p is the section pitch angle, defined as the angle between the chord line and the plane of rotation.
- $\theta_{p,0}$ represents the blade pitch angle at the tip.
- θ_T is the blade twist angle.
- α is the angle of attack, which is the angle between the chord line and the relative wind.
- φ denotes the angle of the relative wind.
- dF_L is the incremental lift force.

- dF_D is the incremental drag force.
- dF_N is the incremental force normal to the plane of rotation, contributing to thrust.
- dF_T is the incremental force tangential to the rotor's swept circle, responsible for producing useful torque.

Finally, U_{rel} is the velocity of the relative wind.

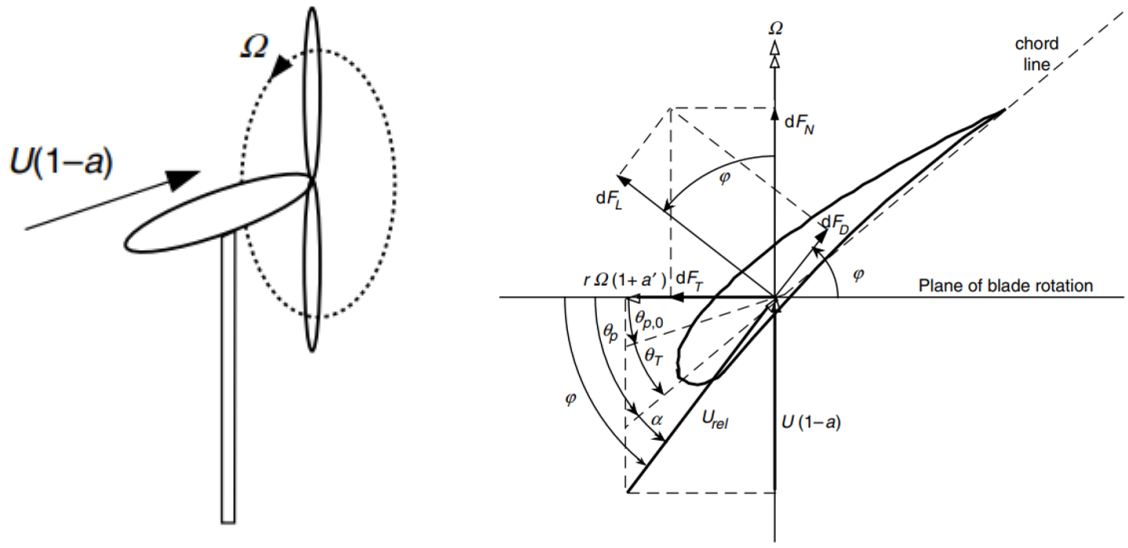

(a) (b)

Fig. 2.7 Flow Scenario (a) and Relationships Between the Various Parameters at HAWT

The angle of the relative wind is equal to the sum of the section pitch angle and the angle of attack:

$$\varphi = \theta_p + \alpha \tag{2.23}$$

Based on Fig. 2.7, the following relationships can be established:

$$\tan\varphi = \frac{U(1-a)}{\Omega r(1+a')} = \frac{1-a}{(1+a')\lambda_r} \tag{2.24}$$

$$U_{rel} = \frac{U(1-a)}{\sin\varphi} \tag{2.25}$$

$$dF_L = C_l \frac{1}{2}\rho U_{rel}^2 c dr \tag{2.26}$$

$$dF_D = C_d \frac{1}{2}\rho U_{rel}^2 c dr \tag{2.27}$$

$$dF_N = dF_L \cos\varphi + dF_D \sin\varphi \tag{2.28}$$

$$dF_T = dF_L \sin\varphi - dF_D \cos\varphi \tag{2.29}$$

If the rotor consists of B blades, the total normal force acting on the section located at a distance r from the center can be expressed as:

$$dF_N = B\frac{1}{2}\rho_{rel}^2(C_l \cos\varphi + C_d \sin\varphi)cdr \tag{2.30}$$

The differential torque (dQ) generated by the tangential force acting at a radial distance r from the center is defined as:

$$dQ = BrdF_T \tag{2.31}$$

$$dQ = B\frac{1}{2}\rho U_{rel}^2(C_l \sin\varphi - C_d \sin\varphi)cr\ dr \tag{2.32}$$

It is important to note that drag has the effect of reducing both torque and power output, while simultaneously increasing the thrust load on the rotor.

2.1.1 Vertical Axis Wind Turbine (VAWT)

Vertical axis wind rotors first appeared circa 200 BC in Sistan, Iran [28], and were utilized as windmills to collect wind energy, shown in Fig. 2.8. These early designs are considered to be among the earliest practical applications of wind power technology, primarily used for grinding grain and pumping water. The rotors consisted of simple vertical shafts with multiple blades or sails attached, allowing them to capture wind from any direction without the need for yaw mechanisms. This omnidirectional capability made them particularly suitable for regions with highly variable wind directions, such as the deserts of Persia.

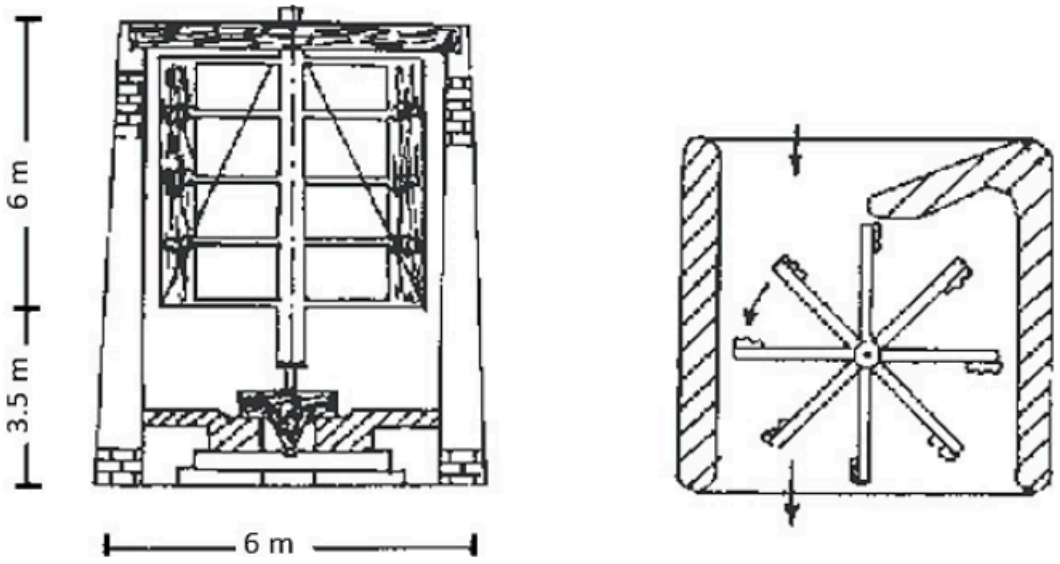

Fig. 2.8 Side view (left) and top view (right) schematic of a windmill in Sistan

In general, VAWTs are classified into two types: Savonius-Rotor and Darrieus-Rotor as shown in Fig. 2.9 [29]. Savonius operates via drag force, identical to the vertical axis windmills constructed by Sistan, and they include a self-starting function, as do HAWTs. However, the Darrieus type requires a beginning function since the blade configuration does not always provide enough torque to rotate. The Darrius type functions using lift force, identical to the 2- or 3-bladed HAWT [30].

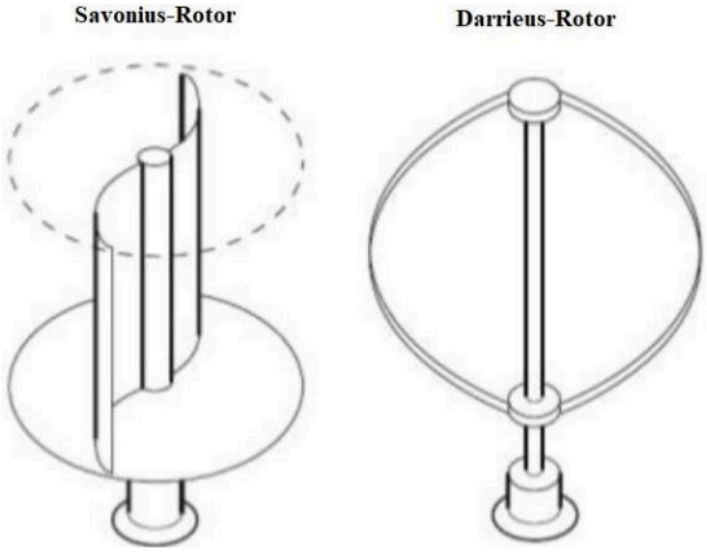

Fig. 2.9 Main types of VAWT [29]

VAWT has several advantages to HAWT, including the ability to take wind in all directions and a lower initial torque. This benefit is a key factor contributing to the greater variety of shapes and designs available for VAWTs compared to HAWTs. Similar to HAWTs, approaching the Betz limit is a critical consideration when developing new VAWT designs. Additionally, the creation of innovative or unique VAWT shapes often aims to meet specific design needs for diverse geographical environments, including areas with low or high wind speeds, urban settings, or commercial zones.

Tables 2.2 and 2.3 provide an overview of the strengths and weaknesses associated with the different configurations and designs of the Savonius and Darrieus types, respectively. These tables serve as a comparative framework to better understand the performance characteristics,

operational limitations, and practical applications of each vertical-axis wind turbine (VAWT) design. In particular, Table 2.2 highlights how Savonius turbines, with their simple structure and self-starting ability, are advantageous for low-speed wind regions and small-scale applications, but often suffer from relatively low efficiency and higher drag losses. Conversely, Table 2.3 outlines the key features of the Darrieus turbine, which, although more efficient and capable of operating at higher tip speed ratios, generally requires an external mechanism for self-starting and tends to involve higher structural complexity.

The designs of each type of turbine are shown in Figs. 2.7 and 2.8, providing a visual reference to complement the comparative data. Figure 2.7 illustrates various configurations of the Savonius turbine, including the traditional two-bucket model as well as modified versions designed to enhance aerodynamic performance and reduce turbulence. Figure 2.8, on the other hand, depicts different Darrieus configurations, such as the classic eggbeater shape and the straight-bladed H-rotor design, each with distinct aerodynamic characteristics and structural implications. By combining the tabulated data with the visual representations, a clearer understanding of the design trade-offs and performance considerations between the two turbine types can be achieved.

Table 2.2 Different configuration of Savonius VAWT advantages and disadvantages

Configuration	Advantage	Disadvantage
Conventional Savonius rotor (Fig. 2.7 A) [30]	• Low starting Torque • Low angular velocity • Generating electricity at low and high wind speeds	• Drag device • Low efficiency
Conventional Savonius rotor with curtains (Fig. 2.7 B) [18]	• Best performance at a fixed rotor position $\vartheta = 60°$ • Power coefficient increases by 38% at optimum curtain design. ($\alpha = 45°$ and $\theta = 15°$, $I_2 = 45cm$ and $I_2 = 52cm$)	• Change in the curtains angle setting creates negative torque which reduces the power coefficient of the rotor. • Fixed wind direction. • Drag device • Low efficiency
Modified Savonius rotor without shaft (Fig. 2.7 C) [15]	• Higher maximum power coefficient compared to the	• Negative torque coefficient at rotor angles ranging from 135°-165° and 315°-345°

	conventional Savonius rotor with the value of C_{pmax} = 0.21	• Drag device • Low efficiency
Conventional Savonius rotor with Combined Conventional and elliptical blade (Fig. 2.7 D) [10]	• The maximum power coefficient of the combined blade is 11% more compared to the conventional blade. • The maximum power coefficient of the combined blade is 5.5% more compared to the elliptical blade.	• Drop-in performance with the use of endplates linking shaft. • Drag device • Low efficiency
Savonius wind turbine with double wind tunnels (Fig. 2.7 F) [12]	• Generates 45-68% more voltage compared to the conventional Savonius VAWT.	• Only within a specific wind angle range. • Drag device • Low efficiency
Three-bladed and four-bladed Savonius wind rotor (Fig. 2.7 G) [13]	• Three-bladed Savonius rotor higher power coefficient compared to four bladed.	• The two-bladed Savonius rotor has better performance and a higher power coefficient. • Drag device • Low efficiency
One-stage, Two-stage, and three-stage with 12.5° twisted blade Savonius rotor (Fig. 2.7 H) [11]	• Twisted blade Savonius rotors have better performance compared to the conventional Savonius rotor due to its positive torque in all rotor angles. • Two-stage twisted Savonius with the Maximum power coefficient of C_{pmax} = 0.285 has a higher power coefficient compared to one-stage and three stage.	• Consume more material and more cost for the two-stage and three-stage. • Drag device • Low efficiency

Table 2.3 Different configurations of Savonius VAWT advantages and disadvantages

Configuration	Advantage	Disadvantage
Three straights bladed Darrieus rotors with upper and lower surface connectors. (Fig. 2. 8 A) [11]	• Exceed Betz limit 3 times during one rotor revolution.	• Lower average power coefficient compared to conventional three straight bladed Darrieus rotor.

Straight-bladed Darrieus rotor with upstream deflector (Fig. 2.8 B) [13]	• At a 90° deflector angle, the maximum power coefficient is C_{pmax} = 0.20367 which is 1.3% higher compared to the original model.	• Only suitable for wind with a specific wind direction. • Reduced power coefficient at different deflector angles.
Side by side twin straight bladed Darrieus rotor (Fig. 2.8 C) [15]	• Twin straight-bladed Darrieus rotor has a higher maximum power coefficient compared to the isolated (single) straight-bladed rotor. • Configuration A has a higher maximum power coefficient compared to configuration B. • $C_{pmax} \approx 0.493$ with a gap ratio of 1.2 and phase angle of 60° and a TSR of 1.4	• Suitable for small-scale wind turbines.
Three V-shape blade Darrieus (Fig. 2.8 D) [11]	• Both V-shape and inverted V-shape has a higher maximum power coefficient compared to th straight blade. • When ΔV = 0.6c, power coefficient increased by 20%. • The increment of the power coefficient is mostly on the middle section of the V-shape blade.	• Same as straight-bladed, the V-shape blade there is energy loss on the blade tip region.
Darrieus Phi rotor (eggbeater/curved rotor) (Fig. 2.8 E) [18]	• With the curvature ratio of 1, it has the highest maximum power coefficient of $C_{Pmax} \approx 0.5$. • Cost-effective.	• Rotor height limitation. • Uneven wind velocity on the rotor blades.
Cross axis helical Darrieus rotor (Fig. 2.8 F) [13]	• Collect wind energy from horizontal and vertical directions. • Suitable for low winds speed areas.	• Not suitable for high wind speed areas. • Suitable for small-scale wind turbines.
Helical twist Darrieus rotor (Fig. 2.8 G) [11]	• Steady output during once rotor oscillation.	• Lower Max power coefficient compared to the straight-bladed.

	• Lower noise compares tp straight-bladed, therefore more suitable, and safer for local areas.	• Darrieus and twisted bladded Darrieus rotors.
Straight blade Darrieus with wingtip devices (Fig. 2.8 H) [14]	• Higher lift with endplates, therefore better aerodynamic efficiency. • Winglets decrease the induced drag.	• The end plates make the trailing vortices weaker. • Winglets increase the total drag.
J-shaped straight Darrieus (Fig. 2.8 I) [11]	• Improves the self-starting ability. • Less turbulency and noise. • Remove the pressure side of the blades from the maximum thickness to the thrilling edge.	• Generates drag because of the J shaped blades
H-type Darrieus VAWT rotor with winglets (Fig. 2.8 J) [13]	• The power coefficient with winglet increased by 10-19% compared to the typical H-type rotor. • More output torque at all azimuth angles compared to the typical H-type rotor. • Aerodynamic performance was improved near the region of the blade tips.	• Adding the winglet could change the optimum TSR slightly. • Doesn't change the performance for every azimuth angle for each of the blades.
Darrieus Phi rotor (troposkien shape) with 50% shifted troposkien shape-VAWT & 100% shifted troposkien shape-VAWT (Fig 2.8 K) [13]	• Model A achieved a higher max power coefficient compared to model B and the conventional phi rotor. • Model A perfrms better at a higher TSR range compared to model B and the conventional phi rotor. • Model B performs better at a higher TSR range compared to the conventional phi rotor. • Lesser cost on model A and model B.	• Reduce blade wake interactions on both models compared to the conventional phi rotor.

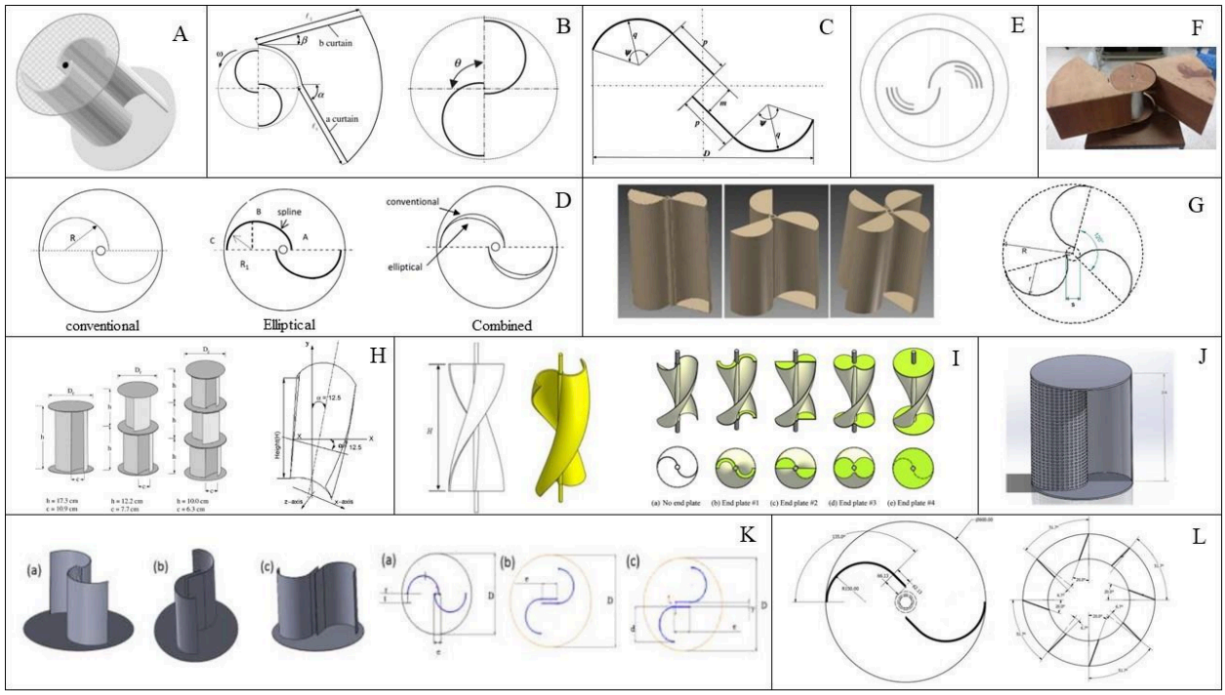

Fig. 2.10 Design of Several Types Savonius as Mentioned in Table 2.2

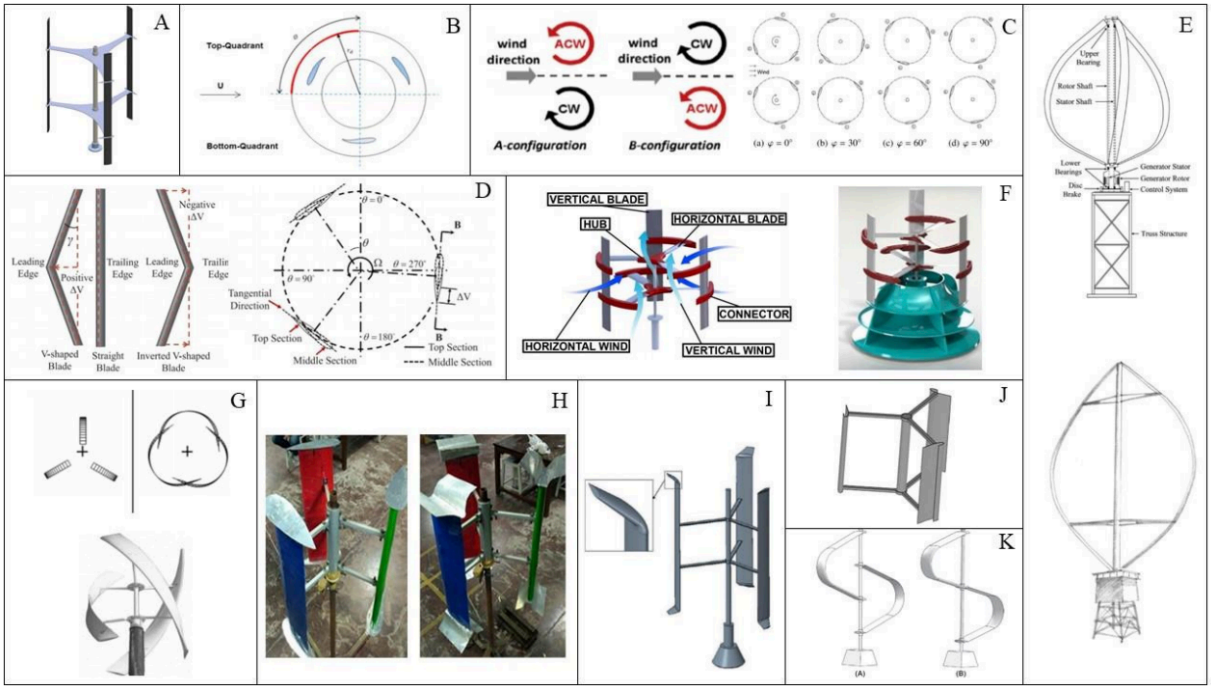

Fig. 2.11 Design of Several Types Darrieus as Mentioned in Table 2.3

Another distinction between the Savonius and Darrieus types lies in their wind speed requirements for starting. Savonius rotors can operate at lower wind speeds, whereas Darrieus rotors require higher wind speeds to begin functioning. However, when it comes to aerodynamic efficiency, the Darrieus type outperforms the Savonius type due to its higher power coefficient.

A VAWT with a lower aspect ratio can attain a higher power coefficient [31]. The aspect ratio of a VAWT blade is determined using Eq. (2.33), where h represents the height of the VAWT blade and r denotes its radius [32].

$$AR_{WT} = \frac{h}{R} \tag{2.33}$$

Fig. 2.12 illustrates the relative airflow velocity V_R and the induced velocity V_a, as described in Eqs. (2.34) – (2.36) [33]. The wind speed is utilized to represent the relative airflow velocity in a nondimensional format.

$$V_R = \sqrt{(V_a sin\theta)^2 + (\omega R + V_a cos\theta)^2} \tag{2.34}$$

$$V_a = V(1 - a) \tag{2.35}$$

$$\frac{V_R}{V} = \sqrt{((1 - a)sin\theta)^2 + (\lambda + (1 - a)cos\theta)^2} \tag{2.36}$$

The induced velocity V_a, angular velocity ω, turbine radius R, and azimuth angle θ are key parameters. Eqs. (2.37) and (2.38) define the normal coefficient C_n and tangential coefficient C_t, respectively.

$$C_n = C_l \cos\alpha + C_d \sin\alpha \tag{2.37}$$

$$C_t = C_l \sin\alpha - C_d \cos\alpha \tag{2.38}$$

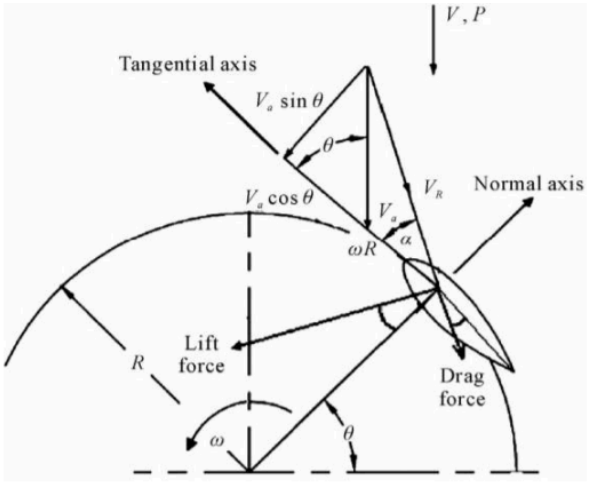

Fig. 2.12 Airfoil velocity and force diagram [33]

The angle of attack α is determined using Eq. (2.39) in these calculations.

$$\alpha = \tan^{-1}\left[\frac{V_a \sin\theta}{\omega R + V_a \cos\theta}\right] \tag{2.39}$$

By substituting Eq. (2.34) into Eq. (2.39):

$$\alpha = \tan^{-1}\left[\frac{(1-a)\sin\theta}{\lambda + (1-a)\cos\theta}\right] \tag{2.40}$$

For single-bladed Darrieus-type VAWTs, three commonly used momentum models are the steady stream tube (SST) model, the momentum stream tube (MST) model, and the double momentum stream tube (DMST) model [34]. Among these, the DMST model is considered the most comprehensive as it accounts for both vertical and horizontal velocity variations within the stream tube [35]. In contrast, the SST model assumes a constant velocity, while the MST model incorporates velocity variations but neglects the effects of the upwind and downwind sections. This makes the DMST model the most accurate and complete of the three. Fig. 2.10 illustrates the differences between these stream tube models [36].

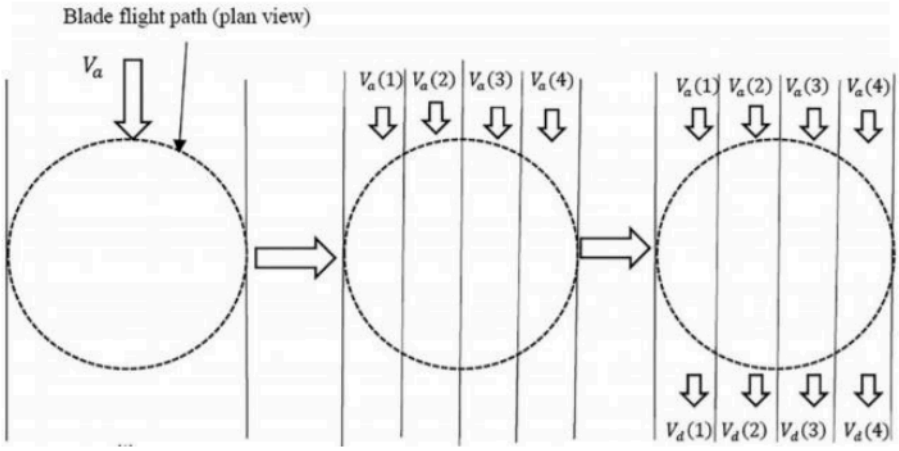

Fig. 2.13 Development of stream tube theory; SST in the (left), MST in the (middle) and DMST in the (right) [36]

Two actuator disks must be arranged in series, as depicted in Fig. 2.14. The wind velocity at the downstream equilibrium is denoted as V_e. The induced velocities for both the upwind V_a and downwind V_a^d are given by Eqs. (2.41) – (2.44) [37].

$$V_a = V(1-a) = \frac{V - V_e}{2} \tag{2.41}$$

$$V_e = V(1-2a) \tag{2.42}$$

$$V_a^d = V(1-2a)(1-a^d) = \frac{V_e+V_w^d}{2} \tag{2.43}$$

$$a^d = \frac{V_e-V_a^d}{V_e} \tag{2.44}$$

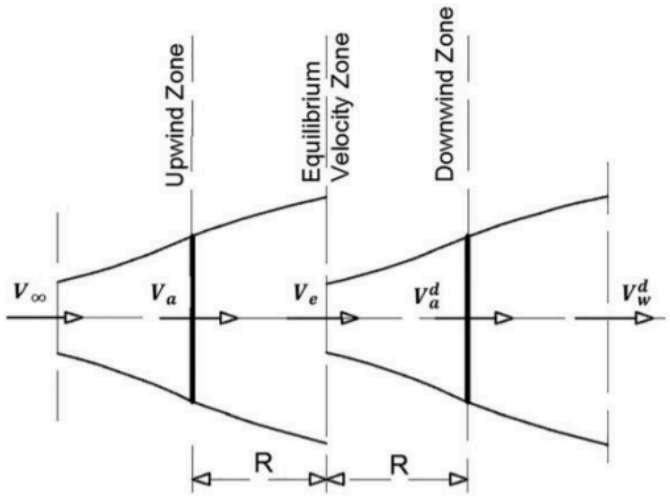

Fig. 2.14 Schematic of the two-actuator disk in tandem [37]

As shown in Fig. 2.15, the upwind and downwind sides are separated, requiring two distinct equations to calculate the power coefficients for each section [33].

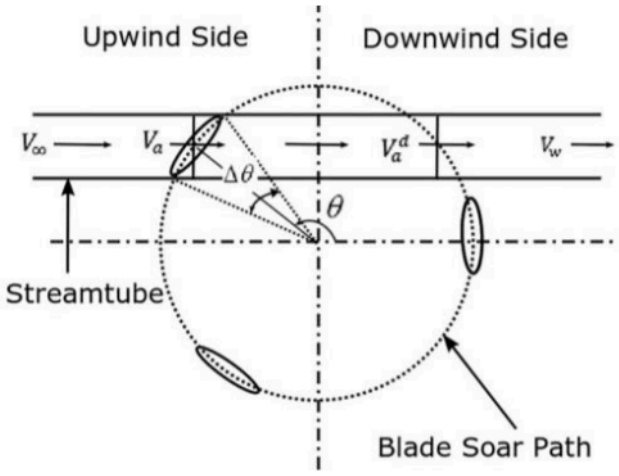

Fig. 2.15 Diagrammatic representation of DMST model [33]

The total power coefficient is the sum of these two values. For the upwind section ($\frac{\pi}{2} \leq 0 \leq \frac{3\pi}{2}$), the relative velocity V_R and the angle of attack α are given by:

$$V_R = \sqrt{(V_a \sin\theta)^2 + (\omega R + V_a \cos\theta)^2} \tag{2.45}$$

$$\alpha = \tan^{-1}\left[\frac{(1-a)\sin\theta}{\lambda+(1-a)\cos\theta}\right]^{-1} \tag{2.46}$$

For the downwind section ($\frac{3\pi}{2} \leq 0 \leq \frac{\pi}{2}$), the relative velocity V_R^d and the angle of attack are given by:

$$V_R^d = \sqrt{\left(V_a^d \sin\theta\right)^2 + \left(\omega R + V_a^d \cos\theta\right)^2} \tag{2.47}$$

$$\alpha = \tan^{-1}\left[\frac{(1-a^d)\sin\theta}{\lambda+(1-a^d)\cos\theta}\right] \tag{2.48}$$

The power coefficient of the upwind section C_{P_u}, the power coefficient of the downwind section C_{P_d}, and the total power coefficient C_P can be calculated using Eq. (2.49) – (2.51), respectively [33].

$$C_{P_u} = \frac{NcH}{2\pi A}\int_{\frac{\pi}{2}}^{\frac{3\pi}{2}} C_t \left(\frac{V_R}{V}\right)^2 d\theta, \tag{2.49}$$

$$C_{P_d} = \frac{NcH}{2\pi A}\int_{\frac{\pi}{2}}^{\frac{3\pi}{2}} C_t \left(\frac{V_R^d}{V}\right)^2 d\theta, \tag{2.50}$$

$$C_P = C_{P_u} + C_{P_d} \tag{2.51}$$

In both Eqs. (2.49) and (2.50), C_t is a key factor. Referring to Eq. (2.26), it becomes evident that airfoils with a high lift-to-drag ratio play a crucial role in the design of a VAWT Darrieus type.

2.2.2 Hybrid VAWT

While Savonius rotors are self-starting, they exhibit low aerodynamic performance as they operate based on drag forces. On the other hand, Darrieus rotors provide excellent aerodynamic efficiency but typically do not start on their own. A hybrid Savonius-Darrieus rotor combines the advantages of both designs, addressing the self-starting issue of the Darrieus rotor and improving the aerodynamic performance of the Savonius rotor [9]. Table 2.4 presents the advantages and disadvantages of the different configurations and designs of the hybrid Savonius-Darrieus rotor.

Table *2*.4 Different configuration of hybrid Savonius-Darrieus VAWT advantages and disadvantage

Configuration	Advantage	Disadvantage
Two-bladed Savonius with three-bladed straight Darrieus (Fig. 2.8 A) [33]	• Better performance compared to Darrieus rotor. • It performs well at low TSR. • Unlike the Darrieus rotor, it can function at low wind speed.	• Complex geometry. • Straight Darrieus has better performance.
Two-bladed Savonius with three-bladed helical Darrieus (Fig. 2.8 B) [36]	• 20% less starting speed compared to Helical Darrieus alone. (At 3 m/s wind speed) • Higher Performance compared to Savonius rotor alone. • Self-starting.	• 20% performance compares to the Helical Darrieus rotor alone.
Double stages two-bladed Savonius with eggbeater Darrieus (Fig. 2.8 C**)** [36]	• Type B extracts more output power from wind in small scale and long wind blowing duration, but Type A can extract better in the short wind blowing duration. • Type A is more compact and is more suitable for local areas. • Self-starting.	• Lower output power compares to the Darrieus rotor alone on both models. • Type B has a longer startup time. • Type B has lower performance
Double stages two-bladed Savonius with two, three, and four-bladed straight bladed Darrieus (Fig. 2.8 D**)** [13]	• Better efficiency with three blades compared to two and four-bladed models. • Optimum power coefficient for the hybrid device at 02. • Self-starting.	• Darrieus rotor alone has better performance and a higher power coefficient. • With 4 Darrieus blades it has better self-starting but a lower maximum power coefficient.
Three-bladed Savonius and thirteen-bladed Darius **(**Fig. 2.8 E**)** [23]	• C_P = 0.38. • Better performance compared to Darrieus rotor. Wind focusers (the orange bottom and top section) helped to increase the energy production by 8%. • Self-starting.	• Complex geometry. Costly design due to the complexity of the design and the quantity of the blades.

Combined Bach-type and H-Darrieus rotor **(**Fig. 2.8 F**)** [26]	• C_{Pmax}= 0.41 which is 54% higher than the Savonius rotor alone. • Self-starting.	• Darrieus rotor alone has 17% higher C_{Pmax} compared to the hybrid model. • Complex model and higher cost because of the multiple Darrieus and Savonius rotors.

According to Table 2.4, the self-starting issue of Darrieus rotors is addressed by combining them with Savonius rotors, though this results in a slightly lower performance compared to pure Darrieus rotors. One important consideration when designing a hybrid Savonius-Darrieus rotor is that the Savonius rotor should be positioned inside the Darrieus rotor [38]. This arrangement allows for better wind capture at short durations and makes the system more compact. Among the various hybrid configurations, the two-bladed Savonius with a three-bladed helical Darrieus rotor is the most recommended due to its relatively simple design and good performance [2].

2.3 COMPUTATIOAL FLUID DYNAMICS (CFD)

Computational fluid dynamics (CFD) is the science that studies the prediction of fluid flow patterns, heat transfer, chemical reactions, and other phenomena by solving mathematical equations or mathematical models [39]. In general, the calculation process for fluid flow is solved using the equations of energy, momentum, and continuity [40]. The equation used is the Navier-Stokes equation. This equation was discovered by G.G. Stokes in England and M. Navier in France around the early 1800s [41]. According to Versteeg (1995), the equations are as follows:

Equation of Energy:

$$\begin{aligned}&\frac{\partial(Er)}{\partial t}+\frac{\partial(uEr)}{\partial t}+\frac{\partial(vEr)}{\partial t}+\frac{\partial(wEr)}{\partial t}\\&=-\frac{\partial(\rho u)}{\partial x}-\frac{\partial(\rho w)}{\partial y}-\frac{\partial(\rho w)}{\partial z}-\frac{1}{Re_r Pr_r}(\frac{\partial q_x}{\partial x}+\frac{\partial q_y}{\partial y}+\frac{\partial q_z}{\partial z}\\&+\frac{1}{Re_r}\begin{pmatrix}\frac{\partial}{\partial x}(u\tau_{xx}+v\tau_{xy}+w\tau_{xz})+\frac{\partial}{\partial y}(u\tau_{xy}+v\tau_{yy}+w\tau_{yz})\\+\frac{\partial}{\partial z}(u\tau_{xz}+v\tau_{yz}+w\tau_{zz})\end{pmatrix}\end{aligned} \tag{2.52}$$

Equation of Momentum:

Momentum in X-axis

$$\frac{\partial(\rho u)}{\partial t}+\frac{\partial(\rho u^2)}{\partial x}+\frac{\partial(\rho uv)}{\partial y}+\frac{\partial(\rho uw)}{\partial z}=-\frac{\partial p}{\partial x}+\frac{1}{Re_r}\left(\frac{\partial \tau_{xx}}{\partial x}+\frac{\partial \tau_{xy}}{\partial y}+\frac{\partial \tau_{xz}}{\partial z}\right) \quad (2.53)$$

Momentum in Y-axis

$$\frac{\partial(\rho v)}{\partial t}+\frac{\partial(\rho uv)}{\partial x}+\frac{\partial(\rho v^2)}{\partial y}+\frac{\partial(\rho uw)}{\partial z}=-\frac{\partial p}{\partial y}+\frac{1}{Re_r}\left(\frac{\partial \tau_{xy}}{\partial x}+\frac{\partial \tau_{yy}}{\partial y}+\frac{\partial \tau_{yz}}{\partial z}\right) \quad (2.54)$$

Momentum in Z-axis

$$\frac{\partial(\rho w)}{\partial t}+\frac{\partial(\rho uw)}{\partial x}+\frac{\partial(\rho vw)}{\partial y}+\frac{\partial(\rho w^2)}{\partial z}=-\frac{\partial p}{\partial z}+\frac{1}{Re_r}\left(\frac{\partial \tau_{xz}}{\partial x}+\frac{\partial \tau_{yz}}{\partial y}+\frac{\partial \tau_{zz}}{\partial z}\right) \quad (2.55)$$

Equation of Continuity:

$$\frac{\partial \rho}{\partial t}+\frac{\partial(\rho u)}{\partial x}+\frac{\partial(\rho v)}{\partial y}+\frac{\partial(\rho w)}{\partial z}=0 \quad (2.56)$$

- x, y, and z represent the coordinates along the X, Y, and Z axes, respectively.
- u, v, and w are the velocity components in the U, V, and W directions.
- t refers to time.
- ρ stands for density.
- E_t represents the total energy.
- P denotes pressure, while Q refers to the heat flux.
- Re is the Reynolds number, and Pr is the Prandtl number.

Essentially, CFD transforms the partial differential equations of continuity, momentum, and energy into algebraic equations. The equations, initially continuous (with an infinite number of cells), are converted into a discrete model (with a finite number of cells) [38].

Broadly, the workflow in Fluent® can be divided into three main types: preprocessing, processing, and postprocessing, as shown in the block diagram in Fig. 2.16 [42]. During preprocessing, the problem is defined through geometry creation, mesh generation, and the specification of boundary conditions and material properties. This stage is crucial, as the accuracy of the simulation strongly depends on the quality of the mesh and the appropriateness of the boundary settings. The processing stage involves the actual numerical solution of the governing equations using iterative solvers, turbulence models, and convergence criteria. Here, Fluent® applies various discretization schemes and algorithms to ensure stability and accuracy of the results. Finally, the postprocessing stage enables users to visualize and interpret the results through contour plots, vector fields, streamlines, and quantitative data extraction. This step facilitates a deeper understanding of the flow characteristics, validates design choices, and provides engineering insights for optimization and decision-making.

Fig. 2.16 CFD Simulation Steps [38]

2.3.1 Preprocessing

The preprocessing stage is the initial step in the CFD process. In this stage, several processes are carried out as follows:

A. Geometry Definition of the Object

In this process, the modeling of the object will be performed. The modeling can be directly done using CFD software, but for objects with complex shapes, it is recommended to use assembly software.

B. Grid Creation (Mesh) or Meshing

Meshing is the process of dividing the component to be analyzed into small or discrete elements. The better the quality of the mesh, the higher the convergence rate. Generally, the cell shapes in the meshing process are divided into two types: two-dimensional and three-dimensional. For two-dimensional cells, there are two types of cell shapes: Triangle and Quadrilateral, as shown in Fig. 2.17.

Fig. 2.17 Triangle Cell (a) and Quadrilateral Cell (b) shape [38]

Meanwhile, the shapes of three-dimensional cells are divided into four types: Tetrahedron, Pyramid, Triangular Prism, and Hexahedron, as shown in Fig. 2.18. The tetrahedron cell is commonly used for complex geometries due to its flexibility in fitting irregular domains, although it may require a larger number of elements to achieve high accuracy. The

pyramid cell often appears as a transition element, typically used to connect tetrahedral regions with hexahedral or prismatic regions in a hybrid mesh. The triangular prism cell, also known as a wedge, is particularly useful in boundary-layer meshing, as its elongated shape allows for better resolution of flow gradients near solid surfaces, which is critical in capturing viscous effects. Finally, the hexahedron cell is generally considered the most efficient in terms of numerical accuracy and convergence, as it provides a structured grid arrangement with low numerical diffusion, but it can be more challenging to generate around complex geometries.

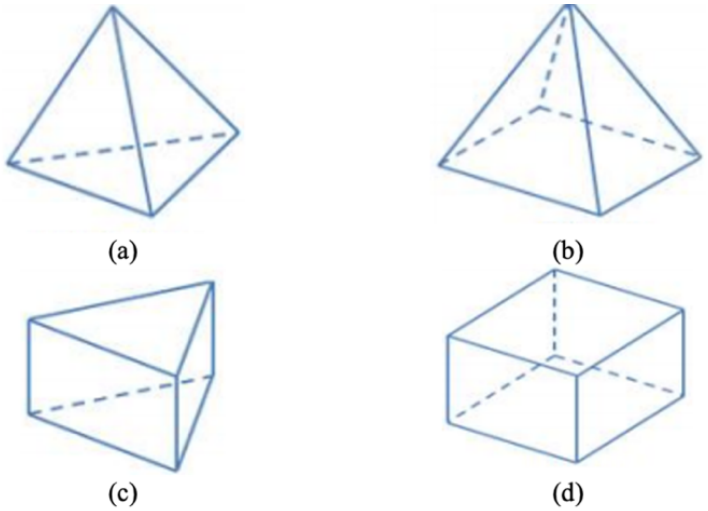

Fig. 2.18 Tetrahedron Cell (a), Pyramid Cell (b), Triangular Prism (c) and Hexahedron (d) shape [38]

2.3.2 Processing

Processing is the second step in the CFD process. In this stage, boundary conditions and initiation methods are determined. In setting boundary conditions, values for the necessary parameters are input. The parameters included as boundary conditions are:

A. Velocity Inlet

The Velocity Inlet boundary condition is used to specify the flow velocity and other scalar quantities, such as temperature, turbulence parameters, and species concentration, at the inlet of the computational domain. This condition is particularly useful when the velocity profile of the incoming flow is known or needs to be controlled directly. The Velocity Inlet boundary condition is commonly applied in problems involving internal flows (e.g., ducts, nozzles, and diffusers) as well as external flows (e.g., wind tunnels or atmospheric boundary layer studies).

B. Mass Flow Inlet

At this boundary condition, the mass flow rate or mass flux, fluid temperature (if the energy equation is activated), gauge pressure at the inlet, flow direction, and turbulence quantities must be provided.

C. Pressure Inlet

At the pressure inlet, the total (absolute) pressure, gauge pressure, temperature, flow direction, and turbulence quantities are input.

D. Pressure Outlet

This boundary condition is applied at the outlet side of the fluid when the outlet pressure is known or can be estimated. At this boundary, the static pressure, backflow temperature, and backflow turbulence quantities must be specified.

E. Outflow

This boundary condition is applied when flow data at the outlet side is unknown. The data at the outlet is extrapolated from the data available before it reaches the outlet.

F. Inlet Vent and Outlet Vent

This boundary condition is applied to inlet/outlet flow models when ventilation equipment is present at the outside of the inlet/outlet, which may cause pressure losses in the flow. The data input for this boundary condition is similar to that for the pressure inlet or pressure outlet, but with additional data for pressure losses.

G. Intake Fan and Exhaust Fan

This boundary condition is applied to inlet or outlet flow models where a fan or blower is present at the outside of the inlet or outlet to blow or suck fluid in the duct. The data required is similar to the pressure inlet/pressure outlet condition, with additional data for pressure increase after passing through the fan/blower (pressure jump).

H. Wall

This boundary condition is applied as a wall for fluid flow within a duct, also known as the duct wall. It is also used as a boundary between the fluid and solid regions.

I. Symmetry and Axis

Symmetry boundary conditions are used when the geometric model of the object and the flow pattern are symmetric. This boundary condition can also be applied to model frictionless

walls in viscous flows. The axis boundary condition is used as the centerline for 2D axisymmetric cases.

2.1.2 Post Processing

Post processing is the final step of the CFD process. In this stage, the results of the calculations based on the boundary conditions and solver methods used are displayed. Post processing provides graphical displays of the mesh, contours, vectors, and path lines. The explanations of these displays are as follows:

A. Displaying Mesh

Displaying the mesh is used to show the mesh on the model being worked on during the boundary condition setup. An example of the mesh with applied boundary conditions is shown in Fig. 2.19 (a). The mesh presented can be displayed not only in 3D but also in 2D.

B. Displaying Contours and Profiles

In this display menu, the contours and profiles of the model being studied are shown. The contours and profiles displayed can include pressure, temperature, or velocity, as shown in Fig. 2.19 (b). Contours can also be presented in other forms, such as flat, as shown in Fig. 2.29 (c).

C. Displaying Vectors

In this display menu, vector shapes of the model being studied are shown. The displayed vectors can represent pressure, temperature, or velocity. An example of the vector display is shown in Fig. 2.19 (d).

D. Displaying Path lines

Path lines are used to visualize the flow of massless particles that form the domain of the problem. An example of the path line display can be seen in Fig. 2.19 (e).

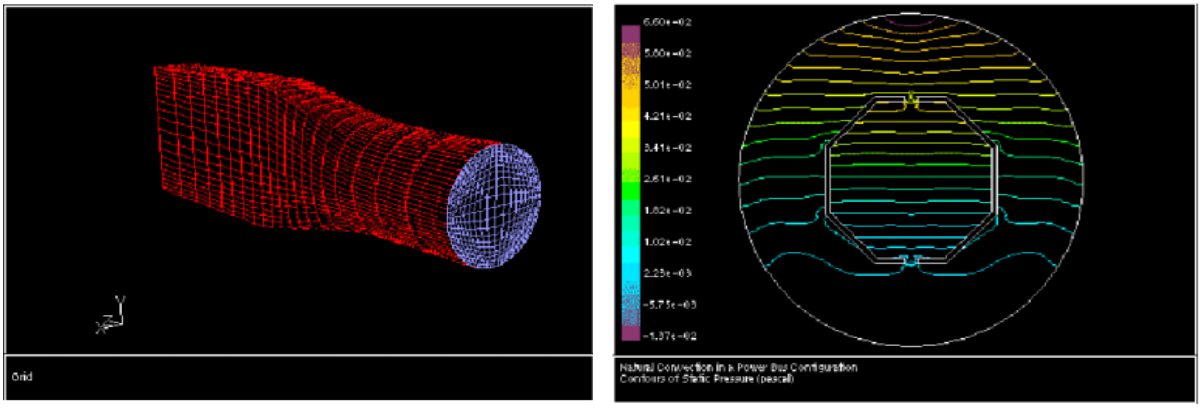

(a) Displayed Mesh

(b) Static Pressure Contour

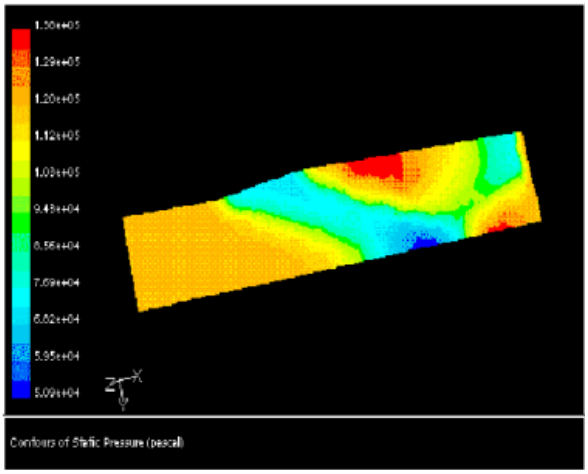

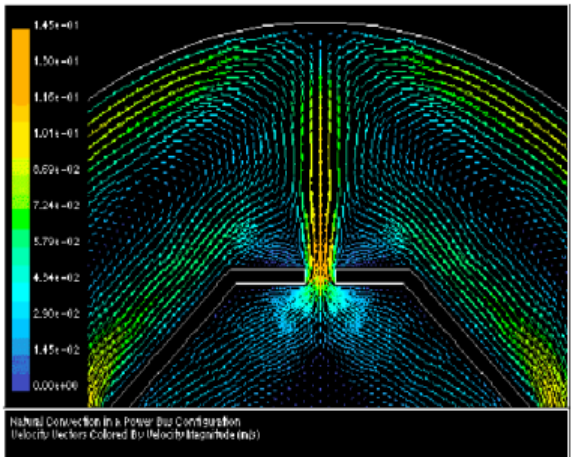

(c) Flat Static Pressure Contour

(d) Velocity Vector

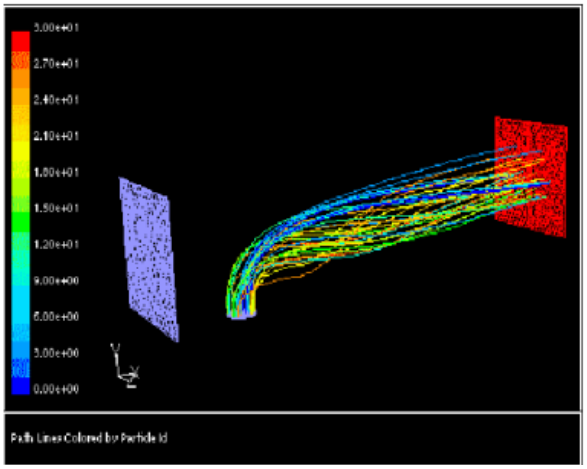

(e) Pathline

Fig. 2.19 Displayed Mesh (a), Static Pressure Contour (b), Flat Static Pressure Contour (c), Velocity Vector (d), and Pathline [42]

2.4 METHODOLOGY

This study was carried out using the two-dimensional (2D) CFD method with the aid of ANSYS Student 2023 R2 module software, which provides a comprehensive environment for fluid flow analysis. The simulation process is systematically divided into three main stages, as illustrated in Fig. 2.17. The first stage is preprocessing, where the computational domain is created, the geometry is defined, and the mesh is generated. The second stage is processing (solution phase), which involves the numerical computation of the governing equations of fluid flow, namely the continuity, momentum, and, if relevant, energy equations. The final stage is postprocessing, where the results obtained from the solver are visualized and analyzed. This

includes generating contour plots, velocity vector fields, pressure distributions, and streamlines, as well as extracting quantitative data such as lift, drag, and torque coefficients.

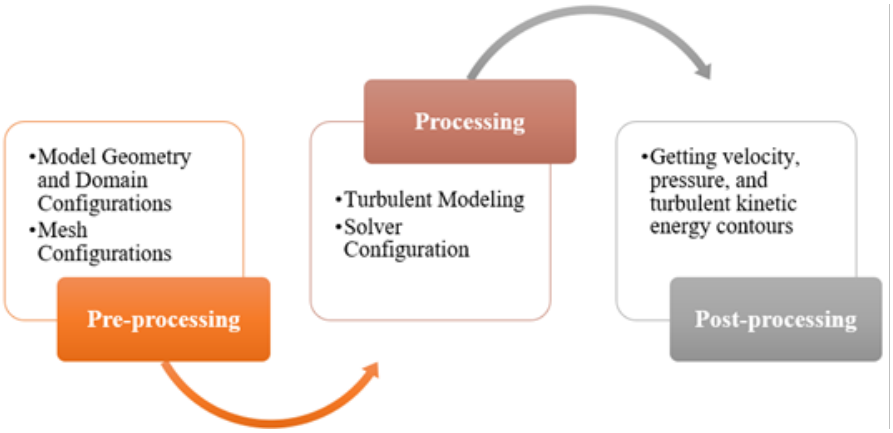

Fig. 2.20 Research Flow Diagram

Detailed steps are explained as follows.

2.4.1 Pre-Processing

The preprocessing stage includes creating geometry, creating boundary conditions, and meshing. This study simulates two types of models: a single Savonius rotor to examine the effects of overlap ratio, and a hybrid Savonius-Darrieus rotor to evaluate the impact of rotor radius ratio as well as its performance under various wind speed conditions. This hybrid model uses Savonius as an internal rotor and Darrieus as an external rotor. The configuration of the single Savonius model is presented in Table 2.5, while the configuration of the hybrid model is shown in Table 2.6.

Table 2.5 Single Savonius Configurations

Turbine model	**Savonius**
Blade Arc's Angle	135
Number of Blades	2
Rotor's Diameter (D)	10 cm
Rotor's Height (H)	7 cm
Overlap Ratio ($\frac{e}{d}$)	0 and 0.2

Table *2*.6 Hybrid Configurations

Savonius	
Number of Blades	2
Overlap Ratio ($\frac{e}{d}$)	0
Aspect Ratio $\left(\frac{h}{D}\right)$	0.7
Blade arch Angle	135º
Radius (R)	3 cm; 6cm; 9cm; 12 cm; and 15 cm
Darrieus	
Airfoil Type	NREL S809
Number of Blades	3
Radius (R)	30 cm
Solidity (σ)	0.5
Angle of Attack (α)	15º

The model design is made using the SolidWorks 2021 software, which is illustrated in Fig. 2.21.

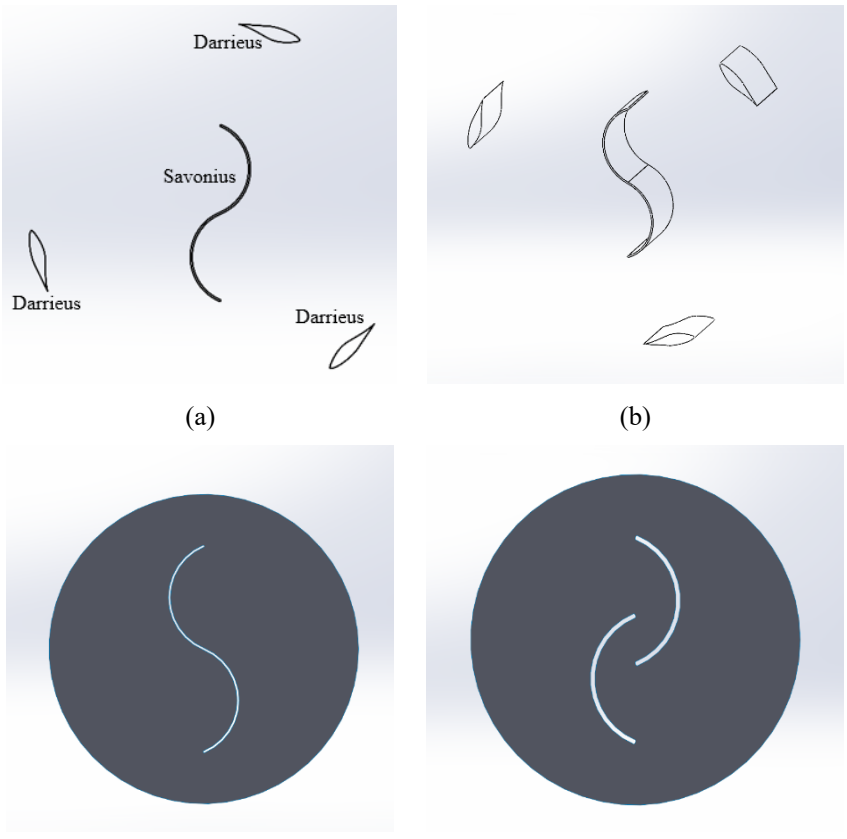

Fig. 2.21 2D (a), 3D (b) Design of the Model, Non-overlap (c), and Overlap (d) Savonius

Although the overlap ratio is occasionally defined slightly differently across articles, this general concept is shown in Eq. (2.57) [43].

$$Overlap\ Ratio = \frac{e}{d} \tag{2.57}$$

Where d and e are the turbine's diameter and overlap's distance, respectively. So, in this case, the overlap distance is 2 cm. In the case of the hybrid model, Savonius was placed in the middle of Darrieus rather than on top to save space. For this time, CFD was carried out in 2D because the turbine model in this study has a homogeneous shape from the bottom upwards.

Then, the boundary conditions are square with a+ pattern in the middle of the boundary to make it easier to form a structured mesh. The size of the boundary condition refers to research [44], i.e., the turbine rotation center is $5D$ from the inlet side, $15D$ from the outlet side, $4D$ from the top and bottom, and the rotating zone has a diameter of $1.5D$. D is the outer diameter of the turbine. The boundary condition is shown in Fig. 2.22.

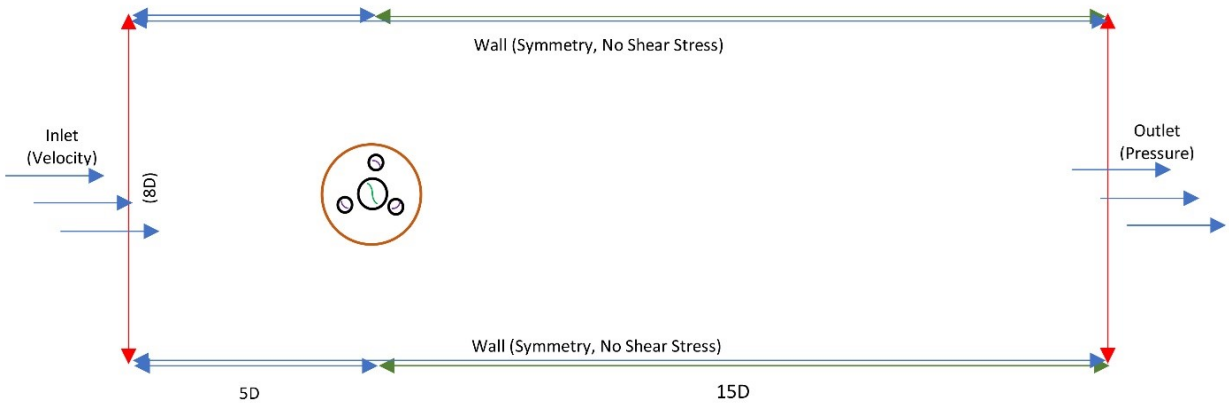

Fig. 2.22 Boundary Conditions

The velocity inlet is the area where the fluid enters. The rotating domain is the area where the turbine rotates. The outlet is the area where the fluid exits the domain. Thus, the fluid flows horizontally from the inlet to the outlet.

Then, the next stage is meshing. The mesh model is a hybrid mesh, a combination of structured and unstructured mesh [45]. It is attempted to make the number of structured meshes more than that of unstructured mesh. The mesh is arranged more tightly on the side of the turbine

blade to capture the fluid phenomenon. Then, inflation is applied. The first layer thickness (Δs) is calculated using Eq. (2.58) [44].

$$\Delta s = \frac{y^+ \mu}{U_f \rho} \tag{2.58}$$

y^+ is a non-dimensionless parameter, and the value is estimated to be 1, μ is the dynamic viscosity of air (1.79x10^{-5} kg/m·s), U_f is the velocity friction of turbine, and ρ is air density (1.225 kg/m^3). While the value of U_f is calculated using Eq. (2.59).

$$U_f = \sqrt{\frac{\tau_{wall}}{\rho}} \tag{2.59}$$

τ_{wall} is the wall shear stress which is calculated using Eq. (2.60).

$$\tau_{wall} = \frac{C_f \rho v^2}{2} \tag{2.60}$$

C_f is the skin-friction coefficient which is calculated using Eq. (2.61).

$$C_f = 0.079 {R_e}^{-0.2} \tag{2.61}$$

R_e is the Reynolds number which is calculated using Eq. (2.62) [46].

$$R_e = \frac{\rho U_\infty D}{\mu} \tag{2.62}$$

U_∞ is the wind speed, D is the diameter of the model. When D is 60 cm, and U_∞ is 5.3 m/s, the Reynold numbers value of the tunnel is 2.17x10^5. Then, the value of Δs can be obtained as 4.84x10^{-5} m using Eq. (2.58). If the experimental conditions differ from those of the simulation, the hydraulic diameter may be used to represent the characteristic diameter of the object.

The meshing results are shown in Fig. 2.23. The generated mesh represents the discretization of the computational domain into smaller elements, which serve as the foundation for solving the governing fluid flow equations numerically.

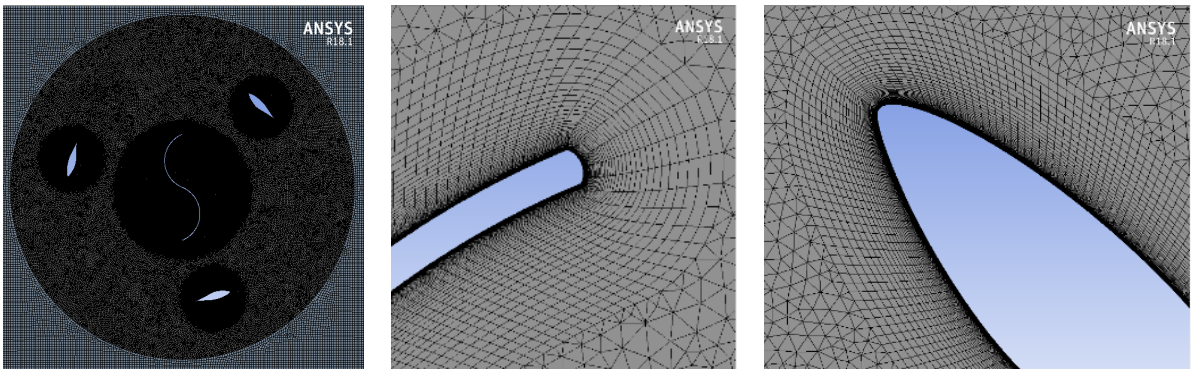

(a) (b) (c)

Fig. 2.23 Meshing of Inner Part (a), Savonius (b), and Darrieus (c)

The efficient mesh density can be assessed through a grid independence test, which is a test that involves studying several variations of mesh density and selecting an efficient mesh model from these variations. The grid independence test is applied as it is sufficient to determine the effectiveness of the mesh composition in the computational process [47]. The mesh quality in this study is an average aspect ratio of 2.108, an average skewness of 0.001, and an average orthogonal quality of 0.996. Referring to [42], the mesh quality in this study is high enough for calculation analysis. However, validation must still be carried out using experimental data to ensure that the mesh density is truly acceptable.

2.4.2 Processing

The next stage is processing. This CFD uses Reynolds-Averaged Navier Stokes (RANS) equations as follows.

Continuity

$$\frac{\partial \bar{\rho}}{\partial t} + \overline{\nabla \cdot u} = 0 \tag{2.63}$$

x-momentum

$$-\nabla \bar{p} + \mu \nabla^2 \bar{u} + \rho g = \rho \left(\frac{\partial \bar{u}}{\partial t} + \bar{u} \cdot \nabla \bar{u} \right) + \nabla RS \tag{2.64}$$

y-momentum

$$-\nabla \bar{p} + \mu \nabla^2 \bar{y} + \rho g = \rho \left(\frac{\partial \bar{v}}{\partial t} + \bar{v} \cdot \nabla \bar{v} \right) + \nabla RS \tag{2.65}$$

ρ is fluid density [kg/m^3], u is wind velocity [m/s], p is fluid pressure [Pa], μ is the dynamic fluid viscosity ($\frac{kg}{m}s$), v is the fluid kinematic viscosity ($\frac{m^2}{s}$), S is training ($\frac{N}{m}$), ∇ indicates the gradient differential operator, and ∇^2 is the Laplacian operator. The RANS equations can describe the phenomenon of fluid flow and explain the balance of forces acting on the fluid [49] so that these fit the needs of this research.

The setup calculation used is shown in Table 2.7.

Table *2*.7 Setup Calculation

Parameters	Value
Viscous Model	Realizable k-e, Enhanced Wall Treatment
TSR	0.1 – 3.5
Turbine Blade	Moving Wall, Rotational, No Slip

Inlet	Velocity Inlet (5.3 m/s)
Rotating Zone	Rotated
Turbulent Intensity	1%
Turbulent Length Scale	0.07D
Outlet	Pressure Outlet
Boundary Wall	Stationary Wall, Symmety
Temperature	288.16 K
Ratio of Specific Heat	1.4
Solution Method	SIMPLE, 2nd Order Upwind, 1st Order Implicit

A wind speed of 5.3 m/s is used based on the average wind speed in the ASEAN region [1] and the validation study [49].

The selection of the viscous model and solution method in this study is carried out by trial and error to obtain the appropriate viscous model and solution method, which could give convergent results. The convergence is set at 10^{-4}, and data collection is carried out for the 6th outer rotor rotations since the turbine starts rotating steadily after the 5th rotation. The calculation process is carried out during this stage every 1° turbine rotation. According to [50], using an increment angle of 1° is recommended because it is quite accurate and does not take long. This affects the time step (Δt) calculated using Eq. (2.66).

$$\Delta t = \frac{\theta \pi}{180 \omega} \tag{2.66}$$

where Δt is the time step $[s]$, θ is the azimuth angle [°], and ω is the rotating speed of the turbine rotor $[\frac{rad}{s}]$. Then, at this processing stage, the moment coefficient value will be generated at each azimuth angle in each tip speed ratio as shown by Fig. 2.24. To obtain the value of the total C_M in each TSR, the value of the C_M at each azimuth angle is averaged.

2.1.3 Postprocessing

The data processing stage in this research refers to the post-simulation analysis conducted after running CFD simulations in ANSYS Fluent. The primary aim was to extract and calculate aerodynamic performance parameters, specifically the moment coefficient (C_M) and power coefficient (C_P) for various rotor configurations and operational conditions, such as changes in tip speed ratio (TSR), rotor radius ratio, and overlap ratio.

In each simulation scenario, torque acting on the turbine shaft was monitored using ANSYS Fluent's in-built moment monitor as shown by Fig. 2.24.

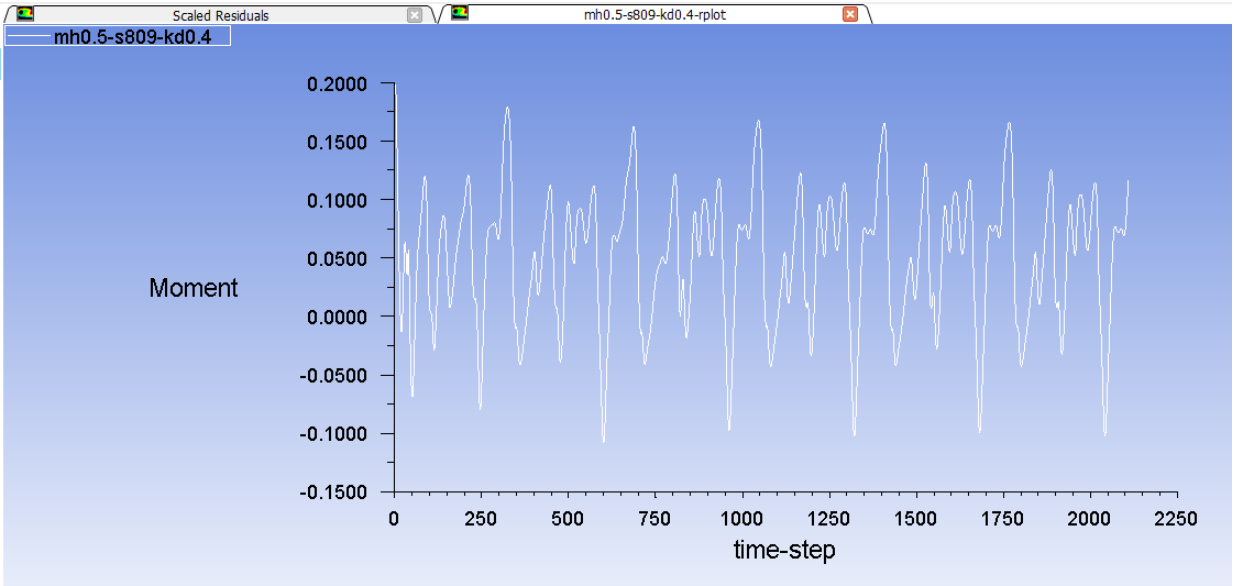

Fig. 2.24 Moment Value

The monitor was set around the central axis of rotation (Z-axis), with selected surfaces corresponding to the rotating blade profiles. The recorded torque values (T in N·m) included both pressure and viscous force contributions acting on the rotating blades.

To ensure stability and accuracy, simulations are conducted over multiple rotor revolutions. Data from the 1st – 5th revolutions are discarded to eliminate transient start-up effects. The average torque over subsequent revolutions was computed and used for further analysis. This averaging process helped reduce numerical oscillations and provided a more representative value of turbine performance under steady-state rotational conditions.

The moment coefficient (C_M) is calculated from the average torque using the following Eq. (2.67).

$$C_M = \frac{\tau}{\frac{1}{4}\rho A D {U_\infty}^2} \tag{2.67}$$

The swept area A is calculated based on rotor height and diameter, which varied depending on the model being tested.

Then, the power coefficient (C_P) represents the efficiency of the rotor in converting wind energy into mechanical energy is calculated indirectly using the moment coefficient and the tip speed ratio as shown in Eq. (2.68).

$$C_P = \lambda \cdot C_M \quad (2.68)$$

Since angular velocity ω and inlet velocity U are input parameters in the simulation, C_P could be derived easily for each TSR. Final values of C_P and C_M are tabulated for each rotor configuration across multiple TSRs. Results are plotted in graphs of C_P vs. TSR and C_M vs. TSR to identify optimal operating points and compare the influence of different design parameters.

2.5 RESULT AND DISCUSSION

2.5.1 Gird Independence Test

When performing CFD, the density of mesh elements greatly affects the accuracy of CFD results. The denser the mesh elements, the higher the C_P value. However, the high value of C_P does not mean that the CFD process is accurate. To determine the accuracy of the CFD results, it is necessary to validate them based on experimental data. A grid independence test is carried out to determine the configuration of mesh elements needed to provide accurate results and an efficient CFD process. The grid independence test uses the two-bladed Savonius model. After obtaining the correct ratio configuration of the number of mesh elements, the configuration is carried out for the hybrid Savonius-Darrieus model.

The mesh elements used for the grid independence test in this study are 33,097; 44,949; 67,759; and 113,556, respectively. These variations in element count were obtained by systematically adjusting the size of the outermost mesh elements to 3.0 cm, 2.8 cm, 2.6 cm, and 2.4 cm, while maintaining a refinement ratio of 0.5 for the inner mesh relative to the outermost cell size. This approach ensures a gradual increase in mesh density, particularly in critical regions near the rotor blades and wake zones, where accurate resolution of flow separation and vortex formation is essential.

The grid independence test was conducted at a tip speed ratio (TSR) of 0.6 with a uniform incoming wind velocity of 5.3 m/s. This condition was selected to represent a typical operating scenario of the rotor while providing a consistent basis for comparing the influence of mesh resolution on the simulation results. The purpose of this test is to determine whether further refinement of the mesh leads to significant changes in the computed performance parameters, such as torque, power coefficient, and pressure distribution.

By evaluating the results across the different mesh densities, the grid independence test ensures that the final chosen mesh provides a balance between computational efficiency and

accuracy. In other words, it identifies the point at which increasing the number of elements no longer yields meaningful improvements in solution accuracy, thereby optimizing both reliability and computational cost.

The grid independence test is evaluated through C_M and C_P graphs. Each graph shows the effect of increasing the number of mesh elements on the C_M and C_P values from the CFD results. The C_M graph at each azimuth angle from the results of the gird independence test is shown in Fig. 2.25. Based on the graph in Fig. 2.22, it can be observed that the more the mesh elements used, the higher the positive moment value in the turbine model, and vice versa. However, the higher resulting C_M value does not indicate accurate results.

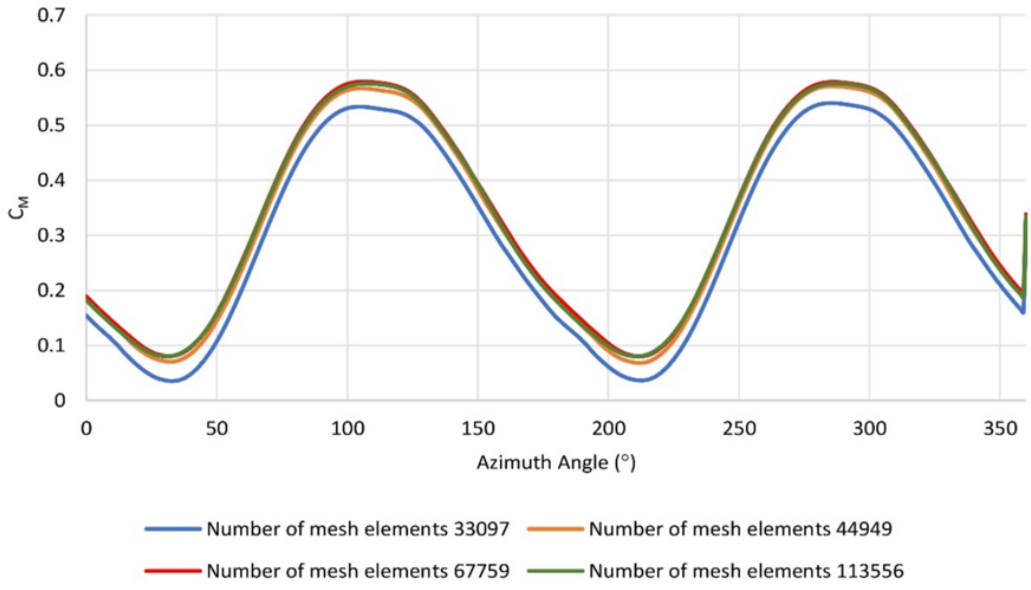

Fig. 2.25 Graph of Moment Coefficient (C_M) at Each Azimuth Angle

Then, C_P data can be used to analyze the sensitivity level of the mesh to changes in the number of mesh elements given. The C_P data from the grid independence test is shown in Fig. 2.26. Based on the graph in Fig. 2.23, the addition of the amount of mesh from 33097 to 44949 gives a large difference in the C_P value, which is 10.73%. It means that in this range, adding of the number of mesh still causes a significant change in the C_P value. The addition of the amount of mesh from 44949 to 67759 gives a C_P difference of 3.05%, while the addition of the mesh from 67759 to 113556 gives a minimal difference, which is 0.99%.

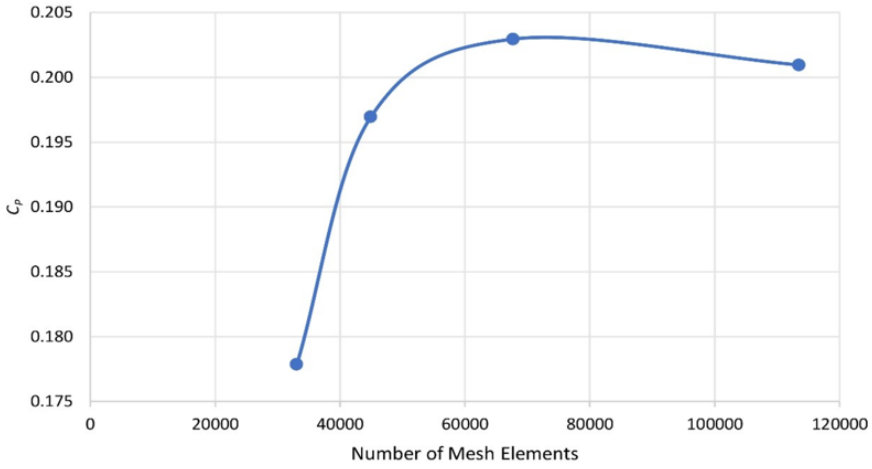

Fig. 2.26 Power Coefficient (C_P) of Grid Independence Test Graph

The slope of the graph of the change in C_P from the number of mesh elements 67759 to 113556 indicates that above the number of meshes 67759, the addition of the number of meshes no longer gives a significant difference to the C_P value. The more the number of mesh elements used, the longer the CFD process takes and the heavier the computer work becomes. The use of the number of mesh elements 67759 is effective in providing CFD results. The ${y^+}_{max}$ value for the internal rotor is 1.723, and the external rotor is 2.421. In addition, among all variations in the number of mesh elements used, the number of mesh elements 67759 has the smallest difference to the experimental data referring to [51], which is 5.82%. Therefore, the 67759-mesh density configuration is applied to the hybrid turbine CFD in this study.

2.5.2 Validation

The mesh density configuration obtained from the results of the grid independence test is used to validate the setup configuration. Validation is carried out to know the accuracy of the selected setup calculation. If the accuracy level is high enough, the selected setup calculation is appropriate and can be employed for the hybrid turbine model. The validation uses secondary data, namely the experimental data of the two-bladed Savonius turbine conducted by [50]. For the validation process, the dimensions of the two-bladed Savonius in this study are the same as the ones of research [52]. Validation is done at TSR 0.1 – 0.9 and wind velocity 5.3 m/s.

The C_P graph of the validation results is shown in Fig. 2.24. Fig. 2.24 shows that the CFD data in this study is similar to the experiment's secondary data [51], except at high TSR, there is a slight difference in value. This slight difference occurs because although the dimensions of the

turbine and several simulation conditions have been made the same as the reference, the temperature and pressure conditions used in the CFD are not the same as the reference since the factors such as the temperature and pressure of the test environment are not described in the reference.

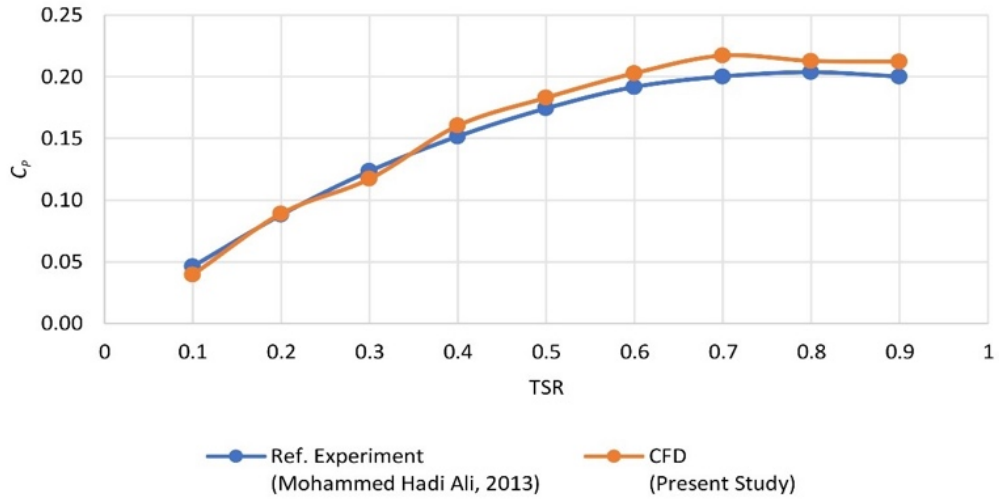

Fig. 2.27 Validation Graph

However, the Realizable k-e, Enhanced Wall Treatment viscous model in the CFD process provides an average difference of 6.26% against the secondary data of the experiment [52]. Based on research [53], the Realizable k-e, Enhanced Wall Treatment viscous model is recommended for hybrid VAWT CFD. Thus, it is believed that the setup calculations to validate the Savonius turbine also provide accurate results when implemented in a hybrid Savonius-Darrieus.

2.5.3 Comparative Analysis of Overlap and Non-Overlap Savonius

There are some results of the simulation, such as velocity, pressure, and turbulent kinetic energy contours. Tip speed ratio (TSR) 0.1, 0.3, and 0.5 at a 135° azimuth angle are selected as an analysis point as the differences are clear at this condition.

A. Velocity Contour

Fig. 2.25 described the velocity contours of the Savonius models. In the contour plots, the turning blade is located on the left, while the advancing blade is located on the right. Based on Fig. 2.25, the differences in terms of the TSR are displayed by the velocity flow pattern as a contour. For both overlap and non-overlap models, the relative velocity magnitude contours

demonstrate that the relative velocity magnitude decreases from the upstream of the rotor to the downstream side. The wind velocity is high on the turning blade of the moving blade because of the inlet velocity's free flow acceleration.

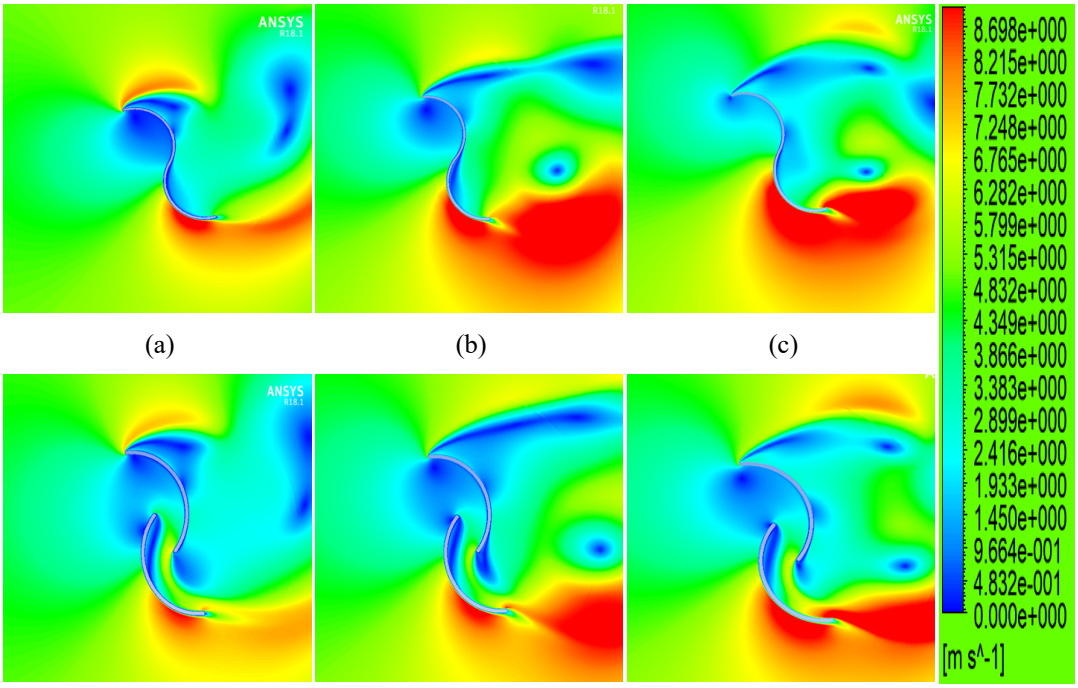

Fig. 2.28 Velocity Contours of Non-overlap Model at TSR 0.1 (a), 0.3 (b), 0.5 (c) and Overlap Model at TSR 0.1 (d), 0.3 (e), 0.5 (f)

Based on the contour, the difference between the overlap and non-overlap models is clearly observed. Advancing blade velocity appears to have decreased as a result of the overlap blade concept. The velocity contours at the overlap model and close to the positive overlap section reveal an expansion of the vortex region independent of the TSR. This suggests that at high tip speed ratios, aerodynamic efficiency declines. This is because, higher TSR increases air speed hitting the blade and generate more, then due to the space (overlap), there will be more vortexes or vortices on the side of the blade.

However, a model with overlap would permit flow to leak from the advancing side to the turning blade, forcing the latter to revolve in the same direction as the rotor. Greater intensity can be found in the wake flow region between the non-overlap turbine buckets and downstream of the rotor area at TSR 0.5. Additionally, the performance of a turbine with overlap is impacted

by the emphasis on deflected airflow from the upstream bucket to the downstream bucket. The overlap model includes greater-speed suction vortices, which reduce the overall pressure around the outer edge of the returning blade. Additionally, in the inner domain, the pressure of the blade on the advancing side is reduced at a greater TSR in the overlap model due to its higher reverse flow.

B. Pressure Contour

Fig. 2.26 described the pressure contours of all models.

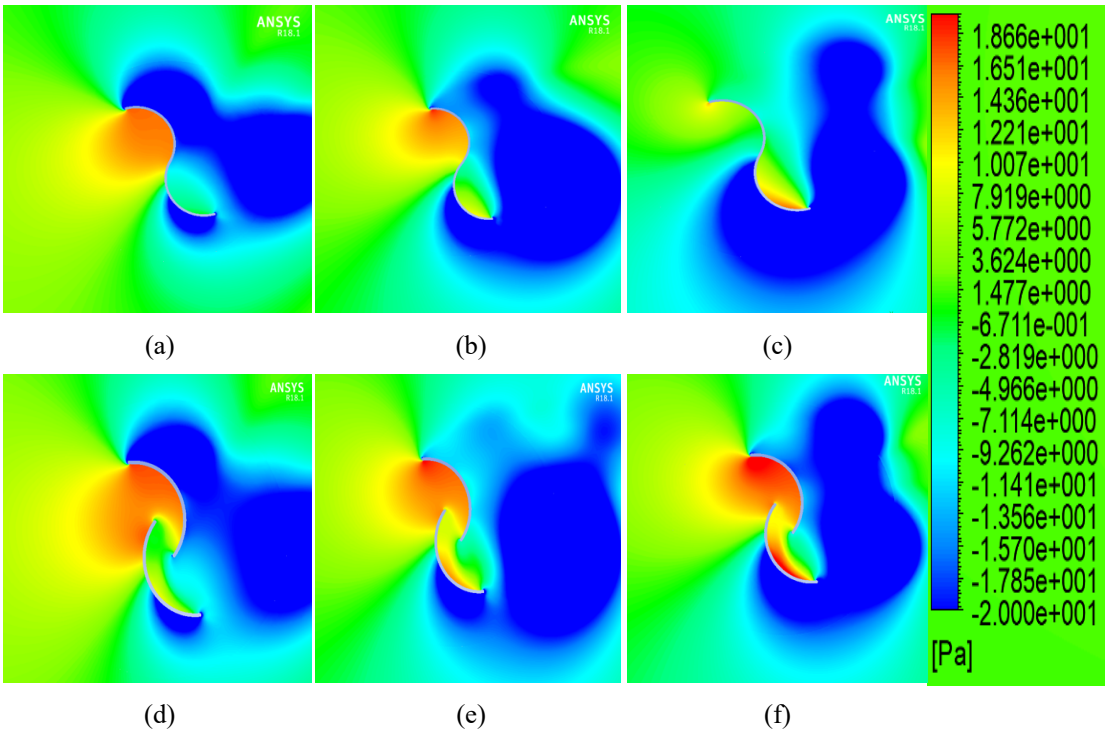

Fig. 2.29 Pressure Contours of Non-overlap Model at TSR 0.1 (a), 0.3 (b), 0.5 (c) and Overlap Model at TSR 0.1 (d), 0.3 (e), 0.5 (f)

Based on Fig. 2.26, all blades seem to have strong pressure on the concave blade. While the convex side of the blade may see a reduction in rotor torque due to pressure. The concave side may experience an increase in positive torque. The increased pressure across the blade's advancing side contributes to improve the value of the turbine torque. The higher pressure on the advancing side is the primary cause of the improved static torque achieved by increasing the ratio of overlap.

The pressure contour graphs indicate a pressure decrease across the rotor from the upstream to the downstream side. This pressure drop signifies that the rotor has been given electricity to turn. In fact, a zone of negative pressure occurs on the convex side of the blades. The static pressure on both blades' turning sides can be seen to be smaller than that on their advancing faces. This occurs due to high flow velocity across the blades' turning side. As a result, a pressure difference acts across the blades' advancing and turning sides, creating the necessary torque to rotate the blades. The turbine rotates clockwise about the shaft due to the torque produced by the drag force created resulting from the continuous pressure at the upper blade. However, only a small portion of the lower blade (the turning blade) contributes favourably to the net torque. These results indicate compatibility with research [43], and the effect of giving overlap can reduce the pressure on the return of blade returns so that it can reduce the negative torque of turbines.

Fig. 2.26 illustrates that the overlap model is facing greater pressure than the non-overlap model. The production performance is influenced by a strong red spot along the advancing blade side. Due to the greater drag force, maximum pressure is seen at the position of the advancing blade, close to the surface of the blade profile. A greater moment and power coefficient resulted from a greater drag force. The moment coefficient value of the turbine rises and keeps rising until it reaches an ideal value before falling once more. So, effects of the overlap blade perform the best and have the highest average moment coefficient when compared with a non-overlap. However, based on the research [53], a better moment and power coefficient can be gained if the overlap is increased to 0.3.

C. Turbulent Kinetic Energy Contours

Fig. 2.27 describes the turbulent kinetic energy contours. Focusing around the Savonius blade for the models, Fig. 2.27 shows the turbulent kinetic energy distribution around the computational domain. These findings show that the kinetic energy of turbulence at the computational domain's entrance is quite low. The turbulent kinetic energy at the rotor rises, notably around the edges of the two blades. In fact, a sizable wake resembling the peak values of turbulent kinetic energy can be seen around the upper attack zone of the advancing. Another wake, like the highest values, may be seen at the lower blade of the Savonius rotor.

The turbulent kinetic energy values drop dramatically behind the rotor. Based on Fig. 2.27, at TSR 0.5, the turbulent kinetic energy of the overlap model is lower than the non-overlap

model. For the overlap model, the turbulence decreases when the TSR increases. These findings can be compared to show that turbulent kinetic energy decreases with overlap. Then, for the non-overlap model, the amount of turbulence is greater downstream, which causes vortices to form and lowers turbine performance.

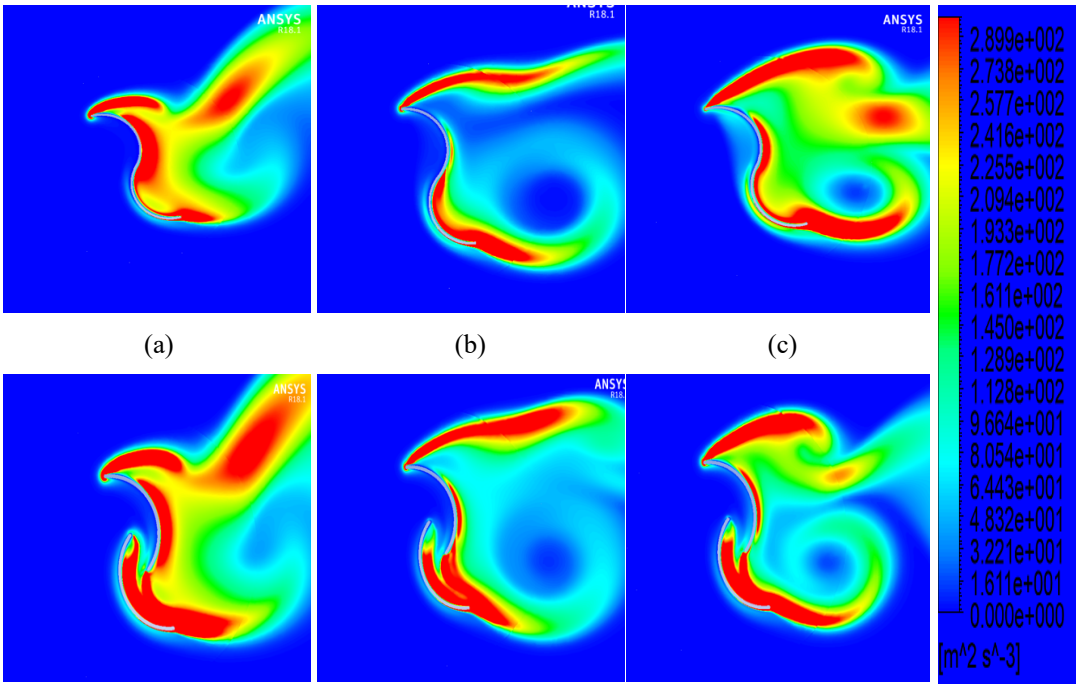

Fig. 2.30 Turbulent Kinetic Contours of Non-overlap Model at TSR 0.1 (a), 0.3 (b), 0.5 (c) and Overlap Model *at TSR 0.1 (d), 0.3 (e), 0.5 (f)*

2.5.4 Comparative Analysis of the Hybrid Rotor Radius Ratios

A. Velocity Contours

Free stream air flows into the turbine blade resulting in a collision between the air mass flow and the turbine blade. The collision causes a force on each turbine blade so that it can rotate it. Simultaneously, the airflow hits the returning blade and advancing blade of Savonius. The advancing blade is the Savonius concave side facing the inlet while the returning blade is the Savonius convex side facing the inlet. In principle, the advancing blade generates positive torque while returning blade generates negative torque. The torque generated by the advancing blade is more dominant to enable the turbine to rotate.

Based on this CFD, the velocity contours across the variations of rotor radius ratios ($\frac{R_S}{R_D}$) can be seen in Fig. 2.28. The velocity contour is taken at TSR 2.5 as it is the optimum TSR of the turbine. The velocity contours are shown at an azimuth angle of 115° because the different contours of each model are most clearly observed at that azimuth angle. Of the five models, the contour near the Darrieus airfoils is mostly the same, but there are differences on the Savonius side. The fluid velocity on the upstream side of Darrieus is lower than that on the downstream, and the greatest fluid velocity occurs at the leading edge.

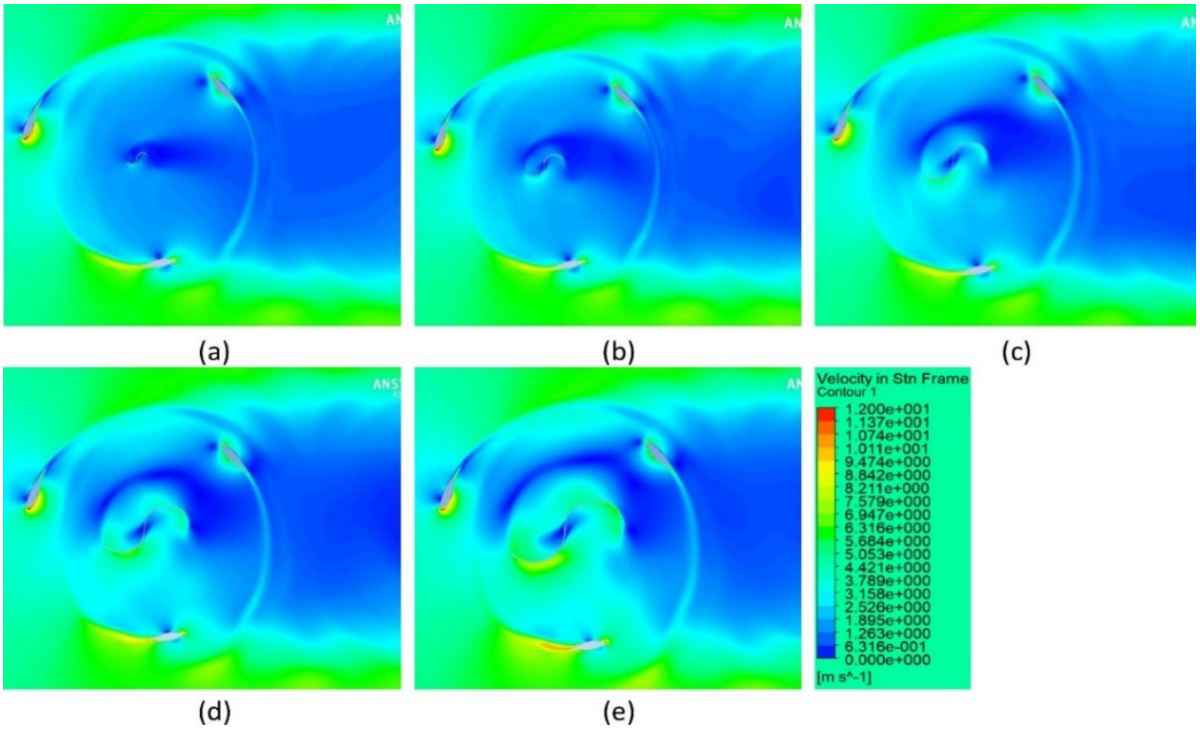

Fig. 2.31 Velocity Contour of $\frac{R_S}{R_D}$ 0.1 (a), $\frac{R_S}{R_D}$ 0.2 (b), $\frac{R_S}{R_D}$ 0.3 (c), $\frac{R_S}{R_D}$ 0.4 (d), and $\frac{R_S}{R_D}$ 0.5 (e)

The flow velocity on the advancing side of the $\frac{R_S}{R_D}$ 0.1 model is the lowest compared to the others. This is indicated by the blue contour color the advancing blade model $\frac{R_S}{R_D}$ 0.1, which is wider than the others. The highest fluid flow velocity on the Savonius advancing blade side occurs in the $\frac{R_S}{R_D}$ 0.5 model. In addition, the flow rate behind the Savonius for the $\frac{R_S}{R_D}$ 0.5 model is also the highest among the others. The flow velocity value is inversely proportional to the

pressure so that if the flow velocity is low, the pressure at that point is high, and vice versa. This can be proven in the pressure contour analysis.

B. Pressure Contours

Then, the characteristics of the pressure generated by the turbine can explain the cause of the rotating turbine and produce a force value. The pressure contour that needs attention is the pressure difference around the turbine blade. The pressure contour of each turbine model are shown in Fig. 2.32.

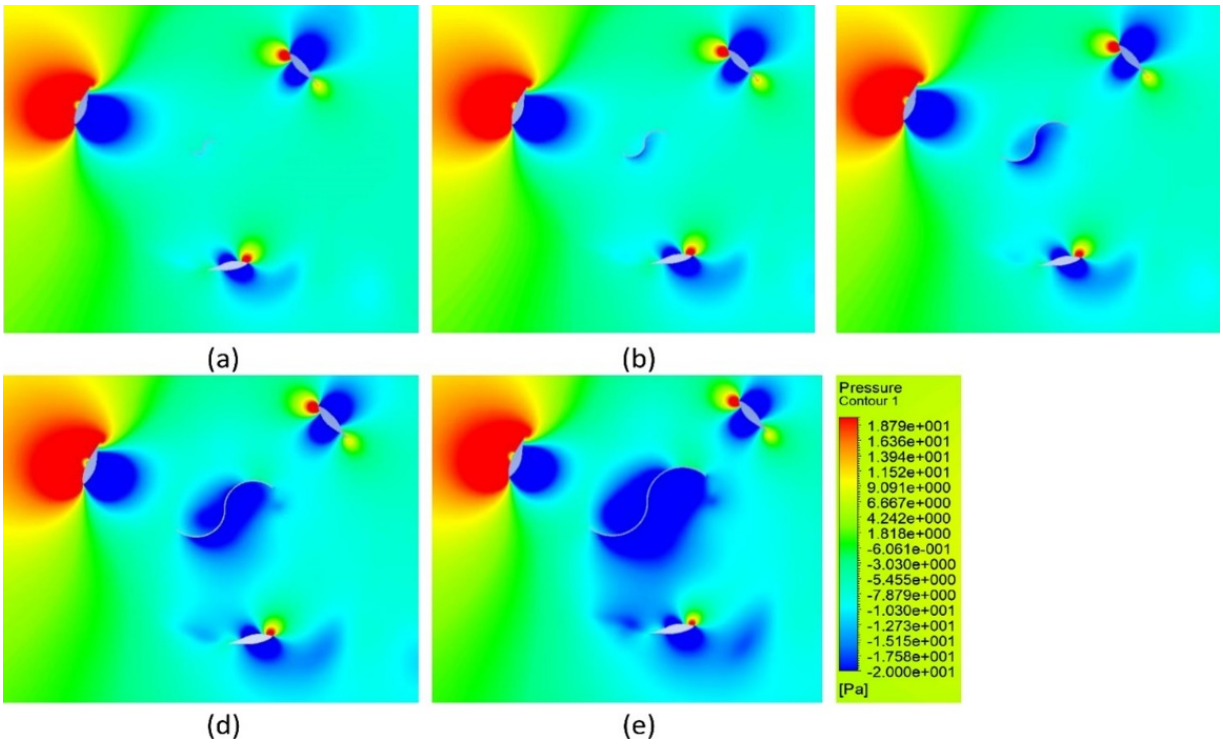

Fig. 2.32 Pressure Contour of $\frac{R_S}{R_D}$ 0.1 (a), $\frac{R_S}{R_D}$ 0.2 (b), $\frac{R_S}{R_D}$ 0.3 (c), $\frac{R_S}{R_D}$ 0.4 (d), and $\frac{R_S}{R_D}$ 0.5 (e)

The pressure contour is also presented at a TSR of 2.5 and an azimuth angle of 115°. Based on the picture in Fig. 2.29, the pressure difference that occurs on Darrieus is greater than on Savonius. Darrieus's upstream side is under greater pressure than the downstream side. It is marked in red on the upstream side while marked in blue on the downstream side. The pressure difference that occurs is very high, reaching 20 Pa upstream and -20 Pa downstream. A direct collision with the fluid mass flow from the inlet causes high pressure on the upstream side of

Darrieus. However, Darrieus's airfoil behind Savonius has a smaller difference than the other airfoils because the flow of fluid hitting it is blocked by Savonius.

Among all the models, the returning blade Savonius from the $\frac{R_S}{R_D}$ 0.5 model receives the greatest pressure. This means that the negative torque generated by the $\frac{R_S}{R_D}$ 0.5 model is the largest compared to the others. The turbine extracts the greater the negative torque that occurs, the less power. Meanwhile, the pressure difference in the Darrieus airfoils of the five models tends to be the same. Thus, the $\frac{R_S}{R_D}$ 0.5 model on the TSR 2.5 has the greatest negative torque, which can cause the power extracted by the turbine to be small. This is proven through the C_M and C_P graphs, which are discussed in the next section.

C. Moment Coefficient

The essence of this study is to determine the effect of $\frac{R_S}{R_D}$ on the performance of the hybrid Savonius-Darrieus NREL S809. This can be analyzed through C_M and C_P graphs from the CFD process. The C_M graph in each TSR is shown in Fig. 2.33.

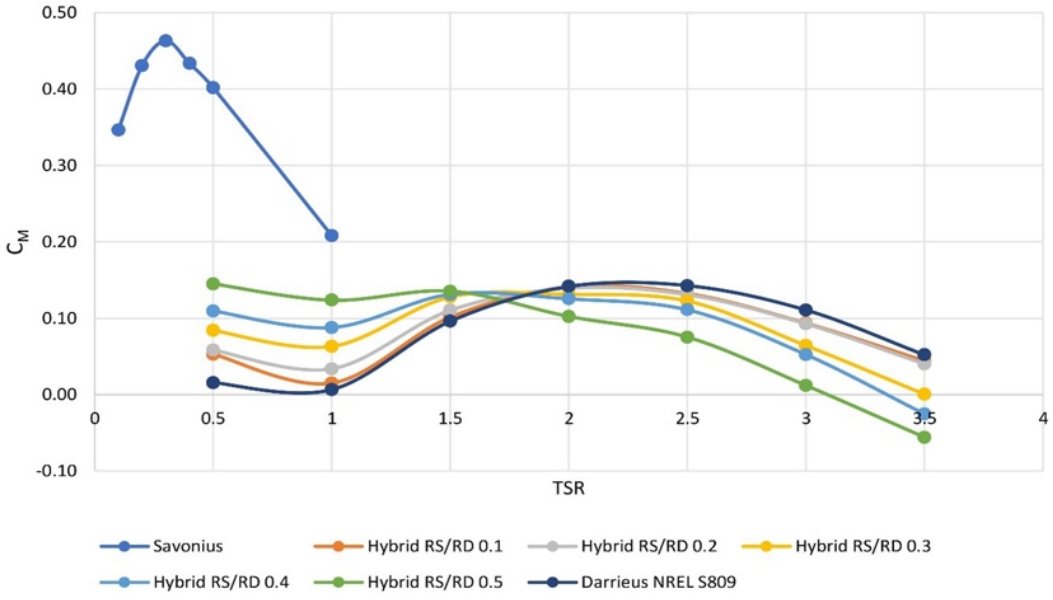

Fig. 2.33 C_M Graph in Several $\frac{R_S}{R_D}$ Variations

CFD is carried out in the TSR range of 0.5 -3.5 because in that range it can be observed the difference in each variation of $\frac{R_S}{R_D}$. The graph in Fig. 2.30 shows that the greater the $\frac{R_S}{R_D}$ value, the

greater the C_M value at low TSR. The high value of C_M at low TSR indicates that the turbine has the sufficient self-starting capability. Of all hybrid models, the C_M value at TSR 0.5 is greater than TSR 1. This is because Savonius works more dominantly at TSR less than 1. Darrieus works more dominantly in the next TSR, but Savonius inhibits Darrieus since it can't rotate at TSR above 1. As a result, after showing an increase in torque at a TSR above 1 and at a certain TSR, all models show a decrease in C_M value again. A turbine owns the largest C_M value at low TSR with an $\frac{R_S}{R_D}$ of 0.5. This shows that the RS/RD 0.5 model has the best self-start.

Furthermore, the wind speed required to rotate is also the lowest compared to the others. In the range of TSR 0.5 – 1.5, the C_M value of the $\frac{R_S}{R_D}$ 0.5 model tends to be stable at C_M 0.15, though it is still unable to exceed the Savonius one. However, the C_M of the $\frac{R_S}{R_D}$ 0.5 model is 8-times higher than single Darrieus at TSR 0.5 and the highest among all hybrid models; this value has exceeded the target to increase the initial C_M of the turbine, which is 5-times higher than a single Darrieus. At low TSR, the $\frac{R_S}{R_D}$ 0.1 model has the smallest C_M value among the others. So, based on the graph of Fig. 2.30, the increase in the $\frac{R_S}{R_D}$ value leads to an increase in the initial C_M value of the turbine, however at a TSR above 1.5, the turbine shows a rapid decrease in C_M value.

D. Power Coefficient

Furthermore, when the C_M value is multiplied by the TSR as Eq. (2.55), the C_P value is obtained, as shown in Fig. 2.34. The graph in Fig. 2.31 shows that the higher the $\frac{R_S}{R_D}$ value, the higher the C_P value at the initial TSR. On the other hand, the higher the $\frac{R_S}{R_D}$ value, the faster the C_P value drops at the TSR above 1.5, and the maximum C_P value decreases as well. Among all hybrid models, the highest maximum C_P value is owned by the 0.1 and 0.2 $\frac{R_S}{R_D}$ models, which are 0.33 at TSR 2.5, respectively. The lowest maximum C_P value is owned by the $\frac{R_S}{R_D}$ 0.5 model, which is 0.20 at TSR 1.5. The smaller the $\frac{R_S}{R_D}$ value, the more dominant Darrieus's work is, which shows that the hybrid turbines with small $\frac{R_S}{R_D}$ tend to have high C_P values at high TSR.

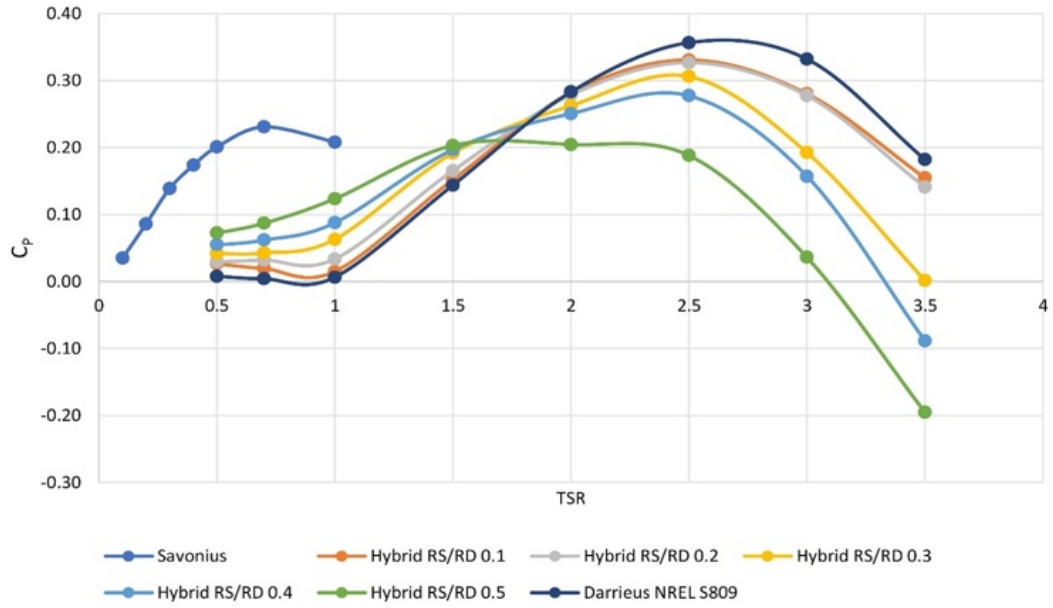

Fig. 2.34 Power Coefficient (C_P) Graph in Several $\frac{R_S}{R_D}$ Variations

At initial TSR, the $\frac{R_S}{R_D}$ 0.5 model has the largest C_P value of 0.07, while the $\frac{R_S}{R_D}$ 0.1 model has the smallest C_P value of 0.03. However, at TSR above 1.5, the $\frac{R_S}{R_D}$ 0.5 model experiences a rapid decrease in C_P value compared to other models. At TSR above 2, the hybrid model's C_P can still not exceed a single Darrieus. Therefore, the $\frac{R_S}{R_D}$ 0.5 model has the smallest maximum C_P value at high TSR compared to other models. However, the $\frac{R_S}{R_D}$ 0.5 model has a C_P value 8-times higher than the single Darrieus in the initial TSR.

The hybrid Savonius-Darrieus turbine's performance is a combination of each turbine's characteristics. Savonius has the characteristic of not being able to rotate above the wind that hits it. Based on these properties, since Savonius prevents Darrieus from rotating at a higher TSR, there is a decrease in the C_M and C_M value. However, as shown by figures, based on the characteristics of each model, the maximum advantage can be achieved if a turbine has C_M and C_M values as high as the $\frac{R_S}{R_D}$ 0.5 model at the low TSR and as high as a single Darius at the high TSR. This condition can be obtained in several ways, one of which is by utilizing the switching rotor mechanism so that at the low TSR, the turbine can rotate in hybrid mode, while at high TSR, the turbine is changed to a single Darrieus mode.

2.5.5 Analysis Switching Rotor Concept Across Various Wind Speeds

Based on the CFD analysis in the previous subchapter, the turbine's performance is fully optimized when rotor switching occurs at a TSR of approximately 2. This section further discusses its performance under various wind speed conditions through CFD analysis.

A. Velocity Contours

Velocity contours are analyzed at TSR 2 because in previous study [54], the switching point is estimated to occur around this TSR. This image is taken for all variations of wind velocities and at an azimuth angle of 135°, as the difference in fluid flows is clear at that angle. The contours are shown in Fig. 2.35.

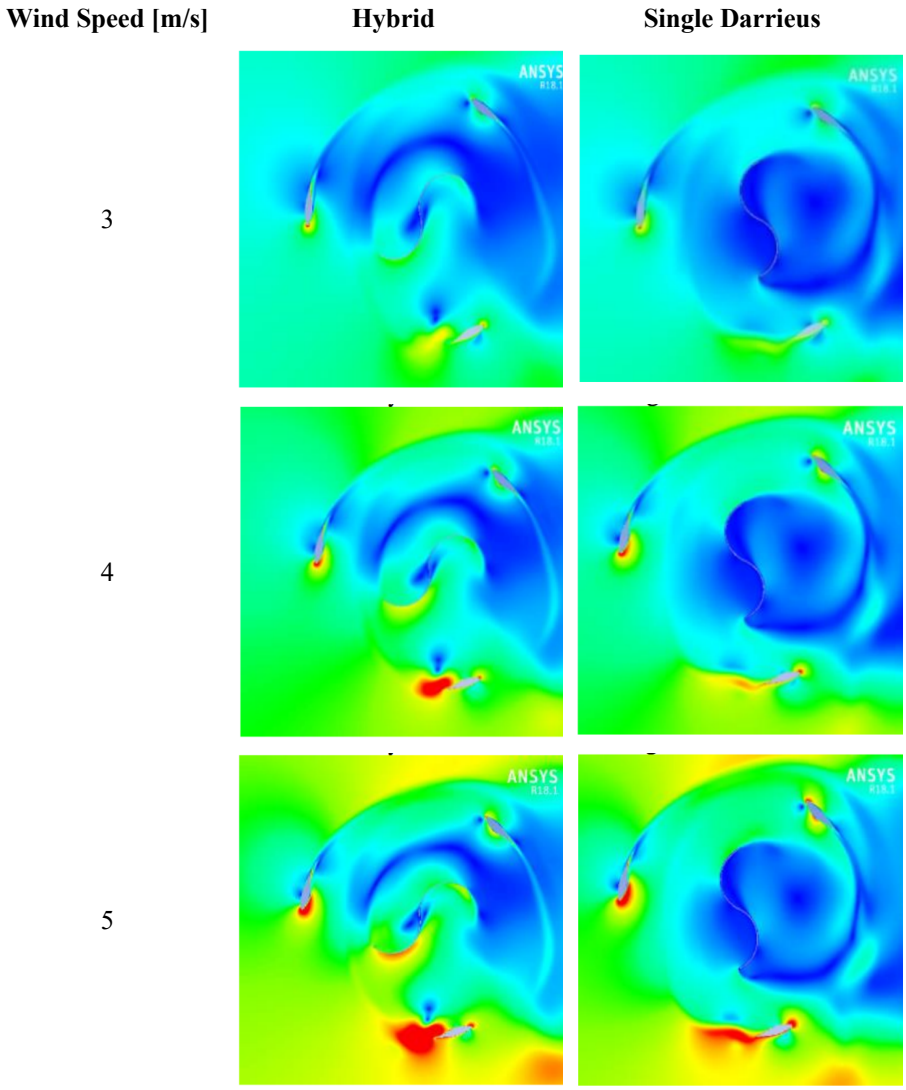

6

7

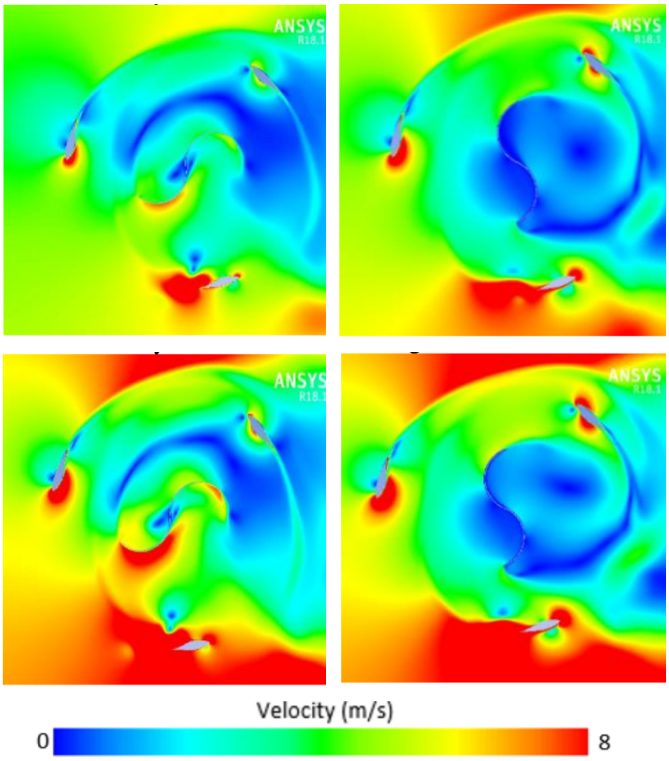

Fig. 2.35 Velocity Contours Across Various Wind Speeds

In Fig. 2.35, the greater the inlet velocity, the higher the flow velocity around the airfoil. In all ranges of wind velocity variations, the flow velocity around the airfoil is higher the turbine is in hybrid rotation mode compared to single Darrieus rotation mode. This is indicated by more red contours around the airfoil when in hybrid rotation mode. After the iteration process is stable for the various input velocities indicated in Table 2.7, Fig. 2.35 is generated. The Realizable $k - \varepsilon$ turbulence model creates contours.

Fig. 2.35 shows that the blade area of wind turbines can produce a small patch of velocity wake. A few areas have velocities that are higher than the speed of unrestricted flow. The back side of the wind turbine blade has a substantially higher velocity than the front blade, creating a significant velocity gradient around the blade. The size of the velocity spread around the blade varies depending on the input velocity. Fig 2.35 also illustrates the relationship between the wake regions of the Darrieus and Savonius rotors. The Darrieus airfoil is impacted by the Savonius rotor's biggest wake zone, which is located behind the rotor and marked with a deep blue color. At those contours, Darrieus airfoil in hybrid rotation mode is stuck in the wake zone, while in single Darrieus rotation mode, Darrieus airfoil can escape. As a result of being stuck in

the wake region, the Darrieus airfoil behind Savonius failed to generate torque. A variation in inlet velocity of 7 m/s gives the smallest wake zone effect on the Darrieus airfoil behind Savonius.

B. Pressure Contours

Then, the pressure contours are shown in Fig. 2.36. These contours provide a clear visualization of the pressure distribution around the rotor blades and within the flow domain. By observing the variation in pressure gradients, it is possible to identify key aerodynamic phenomena such as high-pressure regions on the windward side of the blades, low-pressure zones on the leeward side, and the pressure recovery in the wake region.

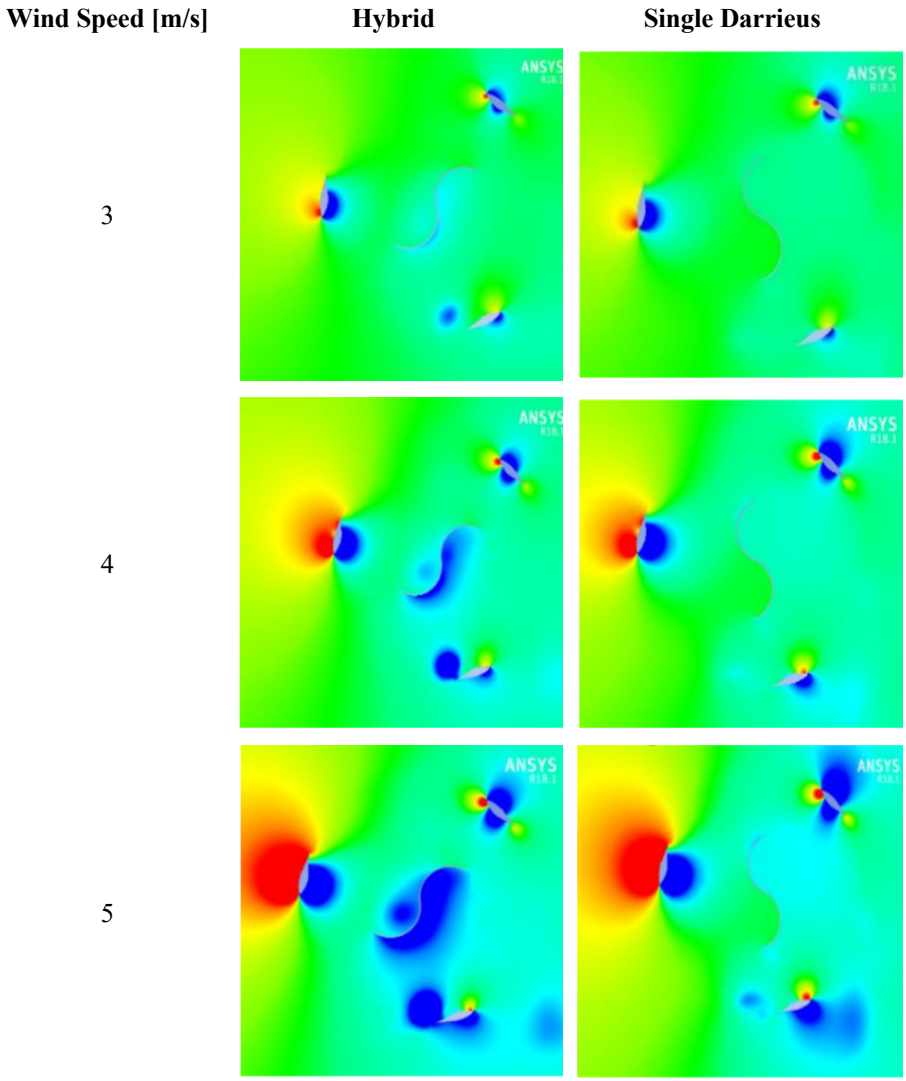

6

7

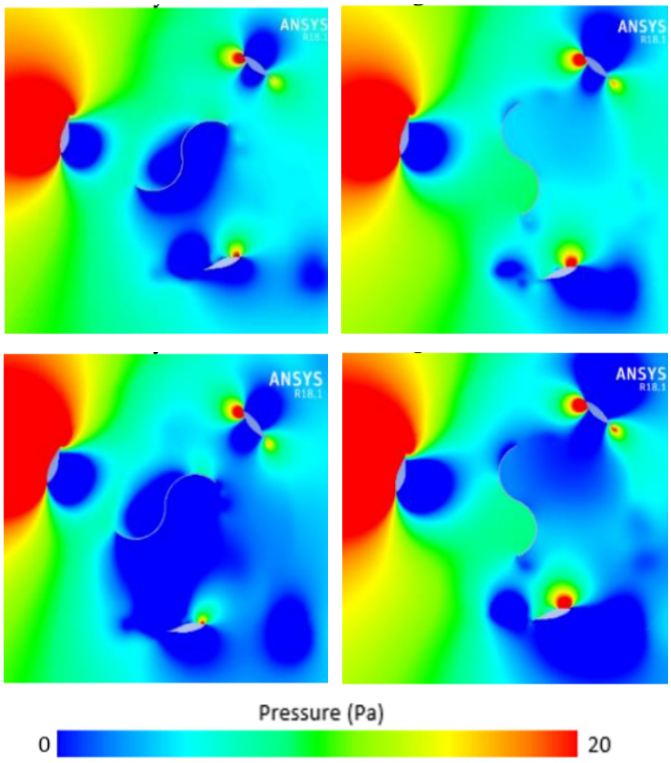

Fig. 2.36 Pressure Contours Across Various Wind Speeds

Pressure has an inverse relationship with the velocity contour. If the velocity is large, the pressure is small, and vice versa. The pressure difference around the Darrieus airfoil is greater than that of the Savonius. Therefore, the Darrieus airfoil is the main point that generates torque on that TSR.

In Fig 2.36, the pressure that occurs around the turbine blades during the single Darrieus rotation mode is greater than the hybrid rotation mode for all variations of wind velocities. The Darrieus airfoil, which is in front of Savonius, is the blade that is the first to be hit by the wind so that it exerts the greatest pressure, and it is the most dominant in generating torque. In single Darrieus rotation mode, the Darrieus airfoil has the greatest pressure at the inlet velocity of 7 m/s. At that time, the moment generated by the Darrieus airfoil is also large. While in hybrid rotation mode, the Savonius blade has a very small pressure zone, marked in deep blue, which influences the Darrieus airfoil behind it, thereby reducing Darrieus ability to generate torque. Based on those contour studies, it can be concluded that the wake zone effect can be avoided by changing the turbine rotation mode from hybrid to single Darrieus at TSR around 2.

C. Moment Coefficient

The improvement for the hybrid Savonius-Darrieus given in this study is changing the turbine rotation from hybrid rotation mode at a TSR below 1.7, to single Darrieus rotation mode at a TSR above it. When the TSR exceeds than 1.7, Darrieus rotates independently, while Savonius in the middle is set so that it does not rotate on the same axis as Darrieus. This ensures that the moment coefficient and power coefficient are only measured from the Darrieus. The moment coefficient of this model is analyzed in the TSR range of 0.5–4 for all wind velocity variations. The results are shown in Fig. 2.37.

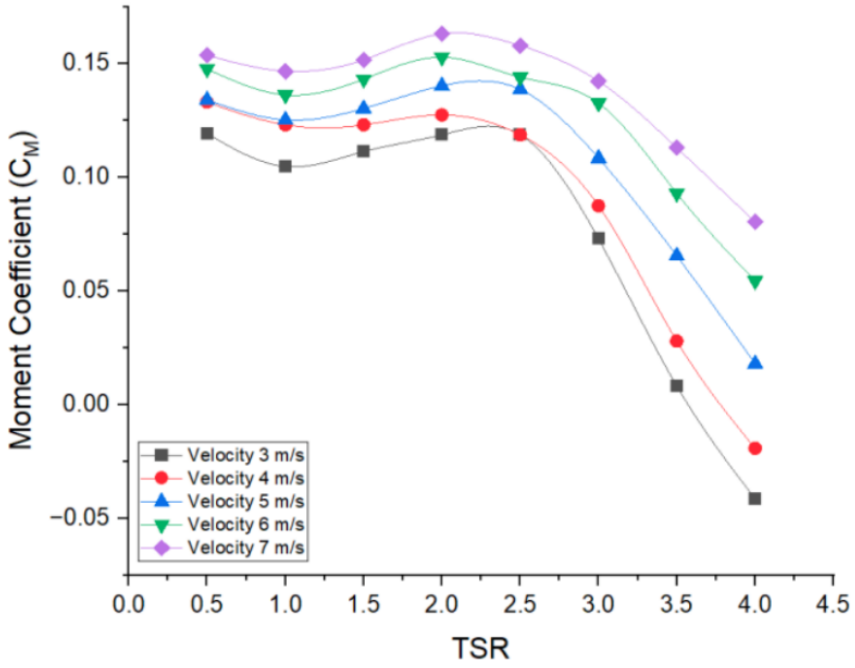

Fig. 2.37 Moment Coefficient Graph Across Various Wind Speeds

The largest initial C_M value can be achieved at the inlet velocity of 7 m/s, which is 0.15. However, there is a decrease in C_M at TSR 1 for all variations of inlet velocity. This is caused by the characteristic of Savonius, which cannot produce a moment when the TSR is over 1, so that it causes a decrease in turbine performance. Whereas in the next TSR, Darrieus works more dominantly which allows it to increase the moment. Therefore, the improvement made by changing the turbine rotation mode from hybrid to single Darrieus is more capable of maintaining the stability of the turbine moment.

D. Power Coefficient

The power coefficient of the turbine across the wind speed variations is shown in Fig. 2.38. In Fig. 2.37 and 2.38, all variations have the same pattern. However, the magnitude of the inlet velocity has an influence on the initial C_M and $C_{P_{Max}}$. The greater the given inlet velocity, the higher the initial C_M and $C_{P_{Max}}$ of the turbine. In addition, the greater the inlet velocity that is given, also causes $C_{P_{Max}}$ to occur at a higher TSR.

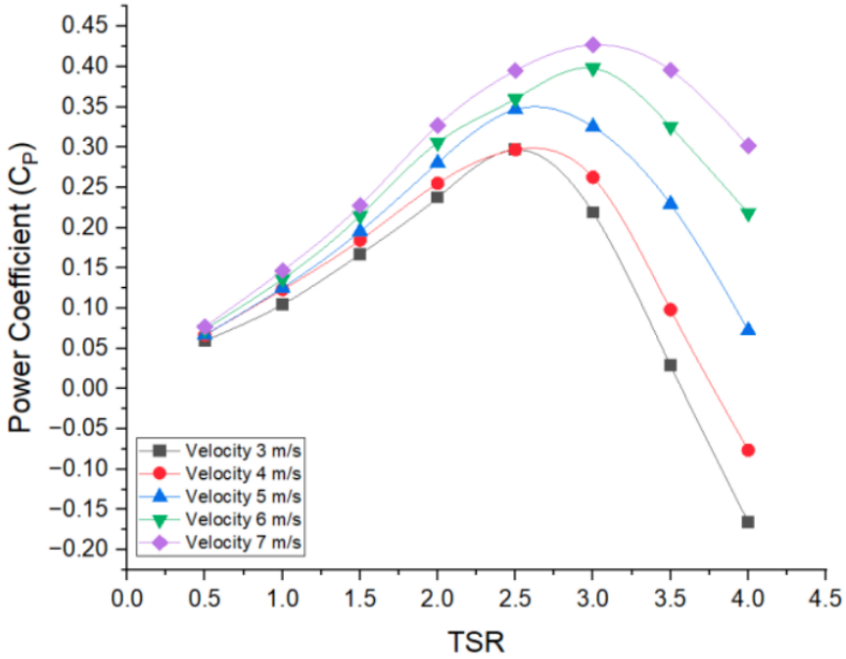

Fig. 2.38 Power Coefficient Graph Across Various Wind Speeds

Fig 2.38 provides information that the best turbine performance occurs at an inlet velocity of 7 m/s. Although at TSR 1–2 the difference in the C_P value of all variations is quite small, at the next TSR, the difference in the $C_{P_{Max}}$ value produced by each variation is quite large. The highest $C_{P_{Max}}$ value occurs at the inlet velocity of 7 m/s, which is 0.47 at TSR 3.5. At a TSR over 2 and high wind speeds, Darrieus's work is very dominant. This is related to the basic characteristic of Darrieus, which delivers strong performance at wind speeds above 4 m/s.

Then, Fig. 2.39 shows a comparison of the C_P of a conventional hybrid turbine, the current study, and a single Darrieus NREL S809. The improvement given in this study is 110% more

effective than Darrieus NREL S809 at a TSR of 0.5. In addition, the current study model can produce a C_P at a TSR of 1–1.5, while the Darrieus NREL S809 shows poor performance. At high TSR, the current study model has a maximum C_P of 50% better than the conventional hybrid.

However, the parallel turbine configuration between Savonius and Darrieus indicates that Savonius is located inside the Darrieus in the same shaft, which can cause the $C_{P_{Max}}$ value of our model to not be as high as the single Darrieus NREL S809 at high TSR. In the future, the positions of the Savonius and Darrieus arrangements will be further studied, which could provide even more optimal results. Then, the comparison of the C_P of a conventional hybrid turbine, the current study, and a single Darrieus NREL S809 is shown in Fig. 2.39.

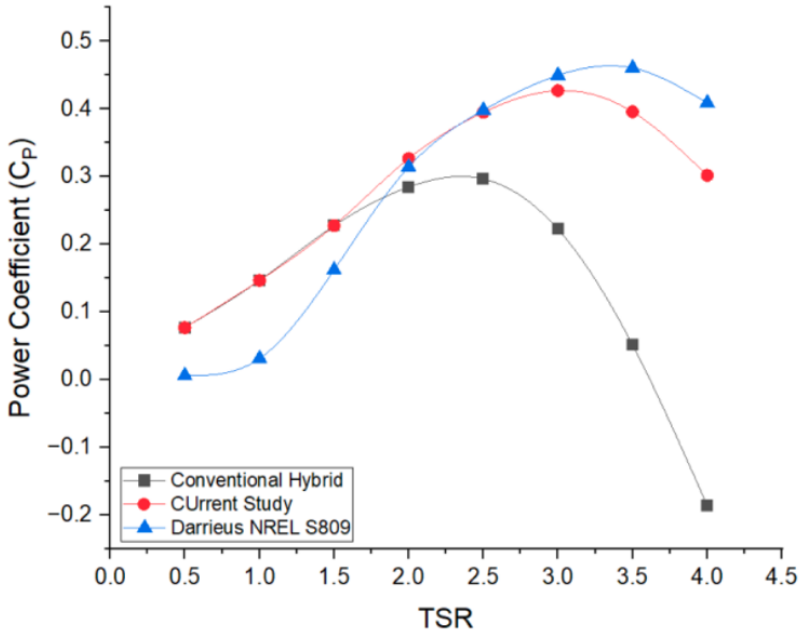

Fig. 2.39 Comparison of Power Coefficient (C_P) of Conventional Hybrid, Current Study, and Single Darrieus NRELS809

2.6 CONCLUSSION

This study analyzed the performance of a hybrid Savonius-Darrieus VAWT using CFD. The results show that the hybrid design improves self-starting but reduces aerodynamic efficiency due to added drag from the Savonius rotor. Increasing the rotor radius ratio ($\frac{R_S}{R_D}$) enhances self-starting but lowers the maximum power coefficient (C_P), while smaller ratios (0.1

– 0.2) yield better efficiency at higher TSRs. A switching rotor mechanism, transitioning from hybrid to single Darrieus mode at TSR ≈ 2, was proposed to optimize performance, reducing wake effects, and improving power extraction. CFD validation showed a 6.26% deviation from experimental data, and a grid independence test confirmed optimal accuracy with 67,759 elements. This study highlights the potential of hybrid VAWTs with optimized design parameters for improved efficiency and real-world applications.

REFERENCES

[1] Y. Chang and H. Phoumin, "Harnessing Wind Energy Potential in ASEAN: Modelling and Policy Implications," *Sustainability*, vol. 13, no. 8, Art. no. 8, Jan. 2021, doi: 10.3390/su13084279.

[2] H. Eftekhari, A. S. M. Al-Obaidi, and S. Eftekhari, "Aerodynamic Performance of Vertical and Horizontal Axis Wind Turbines: A Comparison Review," *Indonesian Journal of Science and Technology*, vol. 7, no. 1, Art. no. 1, 2022, doi: 10.17509/ijost.v7i1.43161.

[3] C. Zhu, Y. Qiu, Y. Feng, W. Zhong, and T. Wang, "Rotational effects on the blade flow of a horizontal axis wind turbine under axial and yawed inflow conditions," *Ocean Engineering*, vol. 271, p. 113764, Mar. 2023, doi: 10.1016/j.oceaneng.2023.113764.

[4] M. Ahmad and M. H. Zafar, "Enhancing vertical axis wind turbine efficiency through leading edge tubercles: A multifaceted analysis," *Ocean Engineering*, vol. 288, p. 116026, Nov. 2023, doi: 10.1016/j.oceaneng.2023.116026.

[5] A. Tummala, R. K. Velamati, D. K. Sinha, V. Indraja, and V. H. Krishna, "A review on small scale wind turbines," *Renewable and Sustainable Energy Reviews*, vol. 56, pp. 1351–1371, Apr. 2016, doi: 10.1016/j.rser.2015.12.027.

[6] A. M. A. El-Zafry, O. E. A. El-Hameed, D. M. S. Hassan, and D. M. M. Shaheen, "A Review On The Types Of Vertical Axis Wind Turbines And The Methods Of Their Performance Study," vol. 6, no. 9, 2019.

[7] S. Roy and U. K. Saha, "Review of experimental investigations into the design, performance and optimization of the Savonius rotor," *Proceedings of the Institution of Mechanical Engineers, Part A: Journal of Power and Energy*, vol. 227, no. 4, pp. 528–542, Jun. 2013, doi: 10.1177/0957650913480992.

[8] M. Yousefi Roshan, J. Khaleghinia, M. Eshagh Nimvari, and H. Salarian, "Performance improvement of Darrieus wind turbine using different cavity layouts," *Energy Conversion and Management*, vol. 246, p. 114693, Oct. 2021, doi: 10.1016/j.enconman.2021.114693.

[9] S. Chegini, M. Asadbeigi, F. Ghafoorian, and M. Mehrpooya, "An investigation into the self-starting of darrieus-savonius hybrid wind turbine and performance enhancement through innovative deflectors: A CFD approach," *Ocean Engineering*, vol. 287, p. 115910, Nov. 2023, doi: 10.1016/j.oceaneng.2023.115910.

[10] T. Wakui, Y. Tanzawa, T. Hashizume, and T. Nagao, "Hybrid configuration of Darrieus and Savonius rotors for stand-alone wind turbine-generator systems," *Electrical Engineering in Japan*, vol. 150, no. 4, pp. 13–22, 2005, doi: 10.1002/eej.20071.

[11] H. Ibadi, A. Sangidzun, D. S. Wijayanto, H. Saputro, Soenarto, and M. B. Triyono, "Effect of Adding of Pitch on the Darrieus Blade Against the Cut In Speed of the Savonius Type S - Darrieus Type H Hybrid Turbine," *J. Phys.: Conf. Ser.*, vol. 1808, no. 1, p. 012003, Mar. 2021, doi: 10.1088/1742-6596/1808/1/012003.

[12] D. Puspitasari and K. Sahim, "Effect of Savonius blade height on the performance of a hybrid Darrieus-Savonius wind turbine," *Journal of Mechanical Engineering and Sciences*, vol. 13, no. 4, Art. no. 4, Dec. 2019, doi: 10.15282/jmes.13.4.2019.09.0465.

[13] M. Ahmad, A. Shahzad, and S. I. A. Shah, "Experimental investigation and analysis of proposed hybrid vertical axis wind turbine design," *Energy & Environment*, p. 0958305X231181675, Jun. 2023, doi: 10.1177/0958305X231181675.

[14] H. Huang, J. Luo, and G. Li, "Study on the optimal design of vertical axis wind turbine with novel variable solidity type for self-starting capability and aerodynamic performance," *Energy*, vol. 271, no. C, 2023, Accessed: Jan. 04, 2025. [Online]. Available: https://ideas.repec.org//a/eee/energy/v271y2023ics0360544223004255.html

[15] S. C. Pryor, R. J. Barthelmie, and T. J. Shepherd, "Wind power production from very large offshore wind farms," *Joule*, vol. 5, no. 10, pp. 2663–2686, Oct. 2021, doi: 10.1016/j.joule.2021.09.002.

[16] S. M. Islam, C. V. Nayar, A. Abu-Siada, and M. M. Hasan, "25 - Power Electronics for Renewable Energy Sources," in *Power Electronics Handbook (Fourth Edition)*, M. H. Rashid, Ed., Butterworth-Heinemann, 2018, pp. 783–827. doi: 10.1016/B978-0-12-811407-0.00027-1.

[17] M. M. Salah, A. G. Abo-khalil, and R. P. Praveen, "Wind speed characteristics and energy potential for selected sites in Saudi Arabia," *Journal of King Saud University - Engineering Sciences*, vol. 33, no. 2, pp. 119–128, Feb. 2021, doi: 10.1016/j.jksues.2019.12.006.

[18] J. G. González-Hernández and R. Salas-Cabrera, "Representation and estimation of the power coefficient in wind energy conversion systems," *Revista Facultad de Ingeniería*, vol. 28, no. 50, pp. 77–90, 2019.

[19] H. Huang, J. Li, and G. Li, "Improving the self-starting and operating characteristics of vertical axis wind turbine by changing center distance in part of blades," *Journal of Building Engineering*, vol. 68, p. 105974, Jun. 2023, doi: 10.1016/j.jobe.2023.105974.

[20] P. Coelho, "The Betz limit and the corresponding thermodynamic limit," *Wind Engineering*, vol. 47, no. 2, pp. 491–496, Apr. 2023, doi: 10.1177/0309524X221130109.

[21] M. H. Ranjbar, S. A. Nasrazadani, H. Zanganeh Kia, and K. Gharali, "Reaching the betz limit experimentally and numerically," *Energy Equipment and Systems*, vol. 7, no. 3, pp. 271–278, Sep. 2019, doi: 10.22059/ees.2019.36563.

[22] Z. Yang, "Wind Turbine Controls for Farm and Offshore Operation," *Theses and Dissertations*, Dec. 2013, [Online]. Available: https://dc.uwm.edu/etd/382

[23] I. Bayati, M. Belloli, L. Bernini, and A. Zasso, "Aerodynamic design methodology for wind tunnel tests of wind turbine rotors," *Journal of Wind Engineering and Industrial Aerodynamics*, vol. 167, pp. 217–227, Aug. 2017, doi: 10.1016/j.jweia.2017.05.004.

[24] P. Giguère and M. S. Selig, "Low Reynolds Number Airfoils for Small Horizontal Axis Wind Turbines," *Wind Engineering*, vol. 21, no. 6, pp. 367–380, 1997.

[25] C. MacEachern and İ. Yıldız, “1.16 Wind Energy,” in *Comprehensive Energy Systems*, I. Dincer, Ed., Oxford: Elsevier, 2018, pp. 665–701. doi: 10.1016/B978-0-12-809597-3.00118-8.

[26] P. O. Ochieng, A. W. Manyonge, and A. O. Oduor, “Mathematical Analysis of Tip Speed Ratio of a Wind Turbine and its Effects on Power Coefficient,” in *International Journal of Mathematics and Soft Computing*, Jan. 2014, p. 61. doi: 10.26708/IJMSC.2014.1.4.07.

[27] J. G. Leishman, “Aerodynamics of Horizontal Axis Wind Turbines,” in *Advances in Wind Energy Conversion Technology*, M. Sathyajith and G. S. Philip, Eds., Berlin, Heidelberg: Springer, 2011, pp. 1–69. doi: 10.1007/978-3-540-88258-9_1.

[28] P. D. Fleming and S. D. Probert, “The evolution of wind-turbines: An historical review,” *Applied Energy*, vol. 18, no. 3, pp. 163–177, Jan. 1984, doi: 10.1016/0306-2619(84)90007-2.

[29] E. A. D. Kumara and N. K. Hettiarachchi, “Review Paper: Overview of the Vertical Axis Wind Turbines,” vol. 4, no. 8, 2017.

[30] K. H. Wong, W. T. Chong, N. L. Sukiman, S. C. Poh, Y.-C. Shiah, and C.-T. Wang, “Performance enhancements on vertical axis wind turbines using flow augmentation systems: A review,” *Renewable and Sustainable Energy Reviews*, vol. 73, pp. 904–921, Jun. 2017, doi: 10.1016/j.rser.2017.01.160.

[31] L. N. Azadani and M. Saleh, “Effect of blade aspect ratio on the performance of a pair of vertical axis wind turbines,” *Ocean Engineering*, vol. 265, p. 112627, Dec. 2022, doi: 10.1016/j.oceaneng.2022.112627.

[32] S. Brusca, R. Lanzafame, and M. Messina, “Design of a vertical-axis wind turbine: how the aspect ratio affects the turbine’s performance,” *Int J Energy Environ Eng*, vol. 5, no. 4, pp. 333–340, Dec. 2014, doi: 10.1007/s40095-014-0129-x.

[33] A. A. Mohammed, H. M. Ouakad, A. Z. Sahin, and H. M. S. Bahaidarah, “Vertical axis wind turbine aerodynamics: Summary and review of momentum models,” *Journal of Energy Resources Technology, Transactions of the ASME*, vol. 141, no. 5, May 2019, doi: 10.1115/1.4042643.

[34] C. S. Bang, Z. A. Rana, and S. A. Prince, “CFD Analysis on Novel Vertical Axis Wind Turbine (VAWT),” *Machines*, vol. 12, no. 11, Art. no. 11, Nov. 2024, doi: 10.3390/machines12110800.

[35] M. Moghimi and H. Motawej, “Developed DMST model for performance analysis and parametric evaluation of Gorlov vertical axis wind turbines,” *Sustainable Energy Technologies and Assessments*, vol. 37, p. 100616, Feb. 2020, doi: 10.1016/j.seta.2019.100616.

[36] A. A. Mohammed and V. Mustafa, “An Easily Programmable Analysis Approach for Vertical Axis Wind Turbines,” in *Proceedings of the Eighth Asia-Pacific Conference on Wind Engineering*, Research Publishing Services, 2013, pp. 1276–1285. doi: 10.3850/978-981-07-8012-8_293.

[37] N. Fan, X. Yuan, W. Duan, and L. Bi, “A novel improved actuator line method for tandem-arranged wind turbines wake analysis and its application,” *Ocean Engineering*, vol. 313, p. 119301, Dec. 2024, doi: 10.1016/j.oceaneng.2024.119301.

[38] F. Ghafoorian, S. R. Mirmotahari, M. Eydizadeh, and M. Mehrpooya, “A systematic investigation on the hybrid Darrieus-Savonius vertical axis wind turbine aerodynamic performance and self-starting capability improvement by installing a curtain,” *Next Energy*, vol. 6, p. 100203, Jan. 2025, doi: 10.1016/j.nxener.2024.100203.

[39] D. A. Tillman, D. N. B. Duong, and N. S. Harding, “Chapter 7 - Modeling and Fuel Blending,” in *Solid Fuel Blending*, D. A. Tillman, D. N. B. Duong, and N. S. Harding, Eds., Boston: Butterworth-Heinemann, 2012, pp. 271–293. doi: 10.1016/B978-0-12-380932-2.00007-6.

[40] J. F. Helgaker and T. Ytrehus, “Coupling between Continuity/Momentum and Energy Equation in 1D Gas Flow,” *Energy Procedia*, vol. 26, pp. 82–89, Jan. 2012, doi: 10.1016/j.egypro.2012.06.013.

[41] Faro A Ayodeji, “Navier-Stokes Equation (An overview and the simplification),” 2020, doi: 10.13140/RG.2.2.17406.00323.

[42] T. Ahmad, S. L. Plee, and J. P. Myers, “FLUENT User’s Guide”.

[43] M. Ebrahimpour, R. Shafaghat, R. Alamian, and M. Safdari Shadloo, “Numerical Investigation of the Savonius Vertical Axis Wind Turbine and Evaluation of the Effect of the Overlap Parameter in Both Horizontal and Vertical Directions on Its Performance,” *Symmetry*, vol. 11, no. 6, Art. no. 6, Jun. 2019, doi: 10.3390/sym11060821.

[44] S. Chhin and V. S. Djanali, “Numerical Simulation on Hybrid Savonius Turbine with NACA-Airfoils as H-rotor Blades,” in *2020 International Seminar on Intelligent Technology and Its Applications (ISITIA)*, Jul. 2020, pp. 123–128. doi: 10.1109/ISITIA49792.2020.9163710.

[45] A. Taflove, S. C. Hagness, and M. Piket-May, “9 - Computational Electromagnetics: The Finite-Difference Time-Domain Method,” in *The Electrical Engineering Handbook*, W.-K. Chen, Ed., Burlington: Academic Press, 2005, pp. 629–670. doi: 10.1016/B978-012170960-0/50046-3.

[46] H. Chanson, “2 - Fundamentals of open channel flows,” in *Environmental Hydraulics of Open Channel Flows*, H. Chanson, Ed., Oxford: Butterworth-Heinemann, 2004, pp. 11–34. doi: 10.1016/B978-075066165-2.50034-5.

[47] B. Godderidge, M. Tan, S. Turnock, and C. Earl, “A verification and validation study of the application of computational fluid dynamics to the modelling of lateral sloshing,” 2006. Accessed: Jan. 04, 2025. [Online]. Available: https://www.semanticscholar.org/paper/A-verification-and-validation-study-of-the-of-fluid-Godderidge-Tan/49bcd39a43fb688dc1280e703143dff9f32db025?utm_source=direct_link

[48] H. K. Versteeg and W. Malalasekera, *An introduction to computational fluid dynamics: the finite volume method*, 2. ed., [Nachdr.]. Harlow: Pearson/Prentice Hall, 2007.

[49] F. Wenehenubun, A. Saputra, and H. Sutanto, “An Experimental Study on the Performance of Savonius Wind Turbines Related With The Number Of Blades,” *Energy Procedia*, vol. 68, pp. 297–304, Apr. 2015, doi: 10.1016/j.egypro.2015.03.259.

[50] 1Ocean Energy Engineering and Management, Institut Teknologi Sepuluh Nopember, 60111 Surabaya, Indonesia, D. Satrio, I. K. A. Pria Utama, Faculty of Marine Technology, Institut Teknologi Sepuluh Nopember, 60111 Surabaya, Indonesia, M. M, and Faculty of Marine Technology, Institut Teknologi Sepuluh Nopember, 60111 Surabaya, Indonesia, “The influence of time step setting on the CFD simulation result of vertical axis tidal current turbine,” *J. MECH. ENG. SCI.*, vol. 12, no. 1, pp. 3399–3409, Mar. 2018, doi: 10.15282/jmes.12.1.2018.9.0303.

[51] M. H. Ali, “Experimental Comparison Study for Savonius Wind Turbine of Two & Three Blades At Low Wind Speed,” 2013. Accessed: Jan. 04, 2025. [Online]. Available:

https://www.semanticscholar.org/paper/Experimental-Comparison-Study-for-Savonius-Wind-of-Ali/3714f618f873b6dace1f547dec907f9773d884f1

[52] T. P. Syawitri, Y. Yao, J. Yao, and B. Chandra, “Assessment of stress-blended eddy simulation model for accurate performance prediction of vertical axis wind turbine,” *International Journal of Numerical Methods for Heat & Fluid Flow*, vol. 31, no. 2, pp. 655–673, Jun. 2020, doi: 10.1108/HFF-09-2019-0689.

[53] T. Rus, L. F. Rus, D. A. Ilutiu-Varvara, R. Mare, A. Abrudan, and F. Domnita, “Experimental Investigation on the Influence of Overlap Ratio on Savonius Turbines Performance,” *International Journal of Renewable Energy Research (IJRER)*, vol. 8, no. 3, Art. no. 3, Sep. 2018.

[54] E. N. Irawan, S. Sitompul, K.-I. Yamashita, and G. Fujita, “The Effect of Rotor Radius Ratio on The Performance of Hybrid Vertical Axis Wind Turbine Savonius-Darrieus NREL S809,” *Journal of Energy and Power Technology*, vol. 5, no. 1, Art. no. 1, Jan. 2023, doi: 10.21926/jept.2301001.

CHAPTER 3
HYBRID WIND TURBINE TESTING IN HIGH TIP SPEED RATIO EXPERIMENTAL STUDY

3.1 CHAPTER INTRODUCTION

Horizontal axis wind turbines (HAWT) represent the largest part of wind power output, which is around 85% [1]. HAWT offers excellent power coefficients (C_P), although it also necessitates the use of costly electromechanical energy conversion equipment and is complicated to manufacture [2]. However, vertical axis wind turbine (VAWT) is more advantageous in urban locations where wind is erratic and unstable because of its low start-up torque characteristics and other benefits like affordable building costs and easy construction [3]. VAWT can be further classified into a couple of primary groups: force-based drag (Savonius type) and lift (Darrieus type) [4]. The Darrieus' extremely poor initial torque prevents it from self-starting at low wind velocity [5]. On the other hand, the Savonius VAWT exhibits a much smaller power coefficient, but it starts with excellent torque [6]. Furthermore, at present, hybrid models that combine the Savonius and Darrieus rotors have been fitted.

Common wind turbine performance evaluation is done on the mechanical aspect, like research performed by [5]. The subsonic wind tunnel was utilized for the research, which had an open test area with a cross-section of 1x1.25 m and a wind velocity range of 0–9 m/s. Then, the model's rotational speed was measured by a digital tachometer, while a digital force meter was utilized to calculate the force generated by the rotating shaft. The wind tunnel's airflow velocity was measured using a static pitot tube that was linked to a macroscopic manometer. Therefore, the goal of their research is to obtain the magnitude of the turbine torque, which is then used to find the power coefficient value. However, the tip speed ratio (TSR) range of the measurement was relatively low, around 2, which indicates the method needs to be improved.

Then, to perform comparative analysis, a hybrid VAWT evaluation system comprising a triple-bladed Darrieus turbine and a double-staged Savonius turbine was constructed by [7]. Steps were included in the turbine base structure to provide an improved foundation and to accommodate the machinery needed for power extraction and transfer. In the experiment's setup, a direct current (DC) motor serving as the generator and a pulley-based transfer unit were employed. This is a performance evaluation through an electrical approach. Results show that

at every condition, an average of 150% more electricity was produced by the hybrid than by the Savonius, and an average of 22% more than by the Darrieus.

The results of wind tunnel testing on a VAWT prototype were also presented by [8]. The model was an innovative combination of the Savonius-Darrieus rotor. The 4.6 cm radius and 16 cm height Savonius was constructed of aluminum and was based on a batch blade. The NACA 4418 airfoil PVC blades, with a chord of 1.8 cm, were positioned on three axes spaced 120 degrees apart and have a helicoidal design, making up the Darrieus. During the measurement, particle image velocimetry (PIV) was used to test a dynamically scaled turbine model. PIV enables the derivation of wakes and particular fluid flow phenomena in every arrangement as well as correlations in the combined structure. To find the optimal working circumstances, general performance, and efficiency, these findings were combined with electrical testing. Measurements were made of the motor's voltage and current. Finally, the electrical results of measurement as defined by the TSR were provided, including power and torque coefficients.

On the other hand, [9] performed an experiment in hybrid Savonius-Darrieus. A hybrid turbine with an aspect ratio of 1, an overlap ratio of 0.15, and a double-stage Savonius rotor was used. The installation was made up of four distinct arrangements of VAWT connected to 300-watt generators. At Wind Turbine Research Station (WTRS), Kayathar, Tamil Nadu, India, all VAWTs were located on the ground in positions of 8.947°N latitude and 77.774°E longitude, with the aim of guaranteeing favorable wind speed during the experiment. However, analysis of the energy loss resulting from friction in the ball bearing configuration was challenging.

In most articles measuring turbine performance in the low wind speed range, the TSR range obtained was not that wide. Apart from that, the power loss aspect that arises from DC motors was not considered in the detailed measurements. Therefore, this research provides an objective for a new approach to increasing the turbine TSR range in a low-wind speed experiment by considering the effect of power loss from the DC generator used.

3.2 REGENERATIVE TEST

The regenerative test, often called the back-to-back test, is a practical method to evaluate the performance and losses in DC motors and generators. The test bench is designed to perform a variety of experimental tasks, including load testing, no-load testing, locked rotor testing, temperature rise evaluation, loss measurement, DC resistance assessment of windings, and

analysis of torque-speed and current-speed characteristics [10]. The regenerative testing method, also known as the Hopkinson's test, is an efficient technique for analyzing these losses [11]. This method involves coupling two identical machines as shown in Fig. 3.1, one operating as a motor and the other as a generator, to create a closed-loop system.

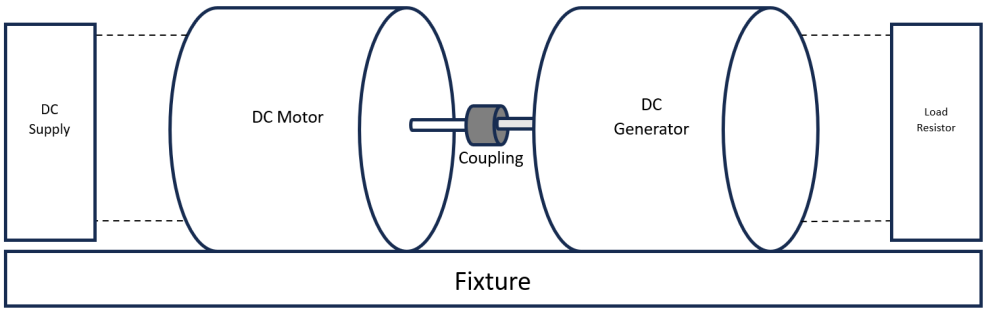

Fig. 3.1 Regenerative Testing Scheme

By recirculating power within the system, it reduces the need for external energy input, making it an energy-efficient approach for determining losses [11].

This method allows the determination of loss coefficients, including iron loss, copper loss, and mechanical/friction loss, while efficiently circulating power between the motor and generator.

3.2.1 Iron Loss (Core Loss)

Iron loss occurs due to hysteresis and eddy currents in the motor core when exposed to alternating magnetic fields [12]. It is frequency-dependent and varies with magnetic flux density. The total iron loss can be expressed as [13]:

$$P_{iron} = k_h f B^2 + k_e f^2 B^2 \quad (3.1)$$

Where P_{iron} is iron loss [W], k_h is hysteresis loss coefficient, k_e is eddy current loss coefficient, f is frequency of magnetic reversals [Hz], B is magnetic flux density [T]. In the regenerative test, iron loss is typically determined by measuring total losses at no load and subtracting mechanical losses.

3.2.2 Copper Loss

Copper loss is caused by resistive heating in the windings [14]. It is proportional to the square of the current and the winding resistance [15]:

$$P_{copper} = I^2 R \quad (3.2)$$

Where P_{copper} stands for copper loss [W], I is current through the winding [A], and R is resistance of the winding [Ω].

3.2.3 Mechanical Loss (Friction and Windage Loss)

Mechanical losses arise from friction in the bearings and windage effects due to air resistance on the rotating parts [16]. These losses are speed-dependent but can generally be approximated as constant for a given speed [17].

$$P_{mechanical} = P_{no-load} - P_{iron} \tag{3.3}$$

Where $P_{no-load}$ is the total power input at no load [W] while P_{iron} is an iron loss at no load [W].

3.3 METHODOLOGY

Basically, this experiment consists of two main stages. The first stage involves testing the method used for measuring the performance of VAWTs at high tip speed ratios, and the second stage applies this testing method to various hybrid Savonius-Darrieus models with different solidity variations.

3.3.1 Models Geometry

As an initial test of the performance measurement method for VAWTs at high tip speed ratios, the primary model used is shown in Fig. 3.2.

(a) (b)

Fig. 3.2 Hybrid Savonius-Darrieus (a) and Single Darrieus (b) Models

Two stages of Savonius with 0.2 overlap and a 135° bucket angle are used as internal rotor. On the other hand, the external rotor is a NREL S809 Darrieus airfoil with a cord length of 7 cm.

Savonius has a radius of 5 cm, while Darrieus has a 10 cm radius, so that it has 0.5 rotor radius ratio. Darrieus is placed with a 45° increment angle and a 0° angle of attack. Their height is 14 cm. The models are created using a 3D printer machine (Fig. 3.3 (a)) with PLA material (Fig. 3.3 (b)). In addition, as a result of the 3D printing, a hollow is applied to each Darrieus blade to minimize the weight (Fig. 3.3 (c)).

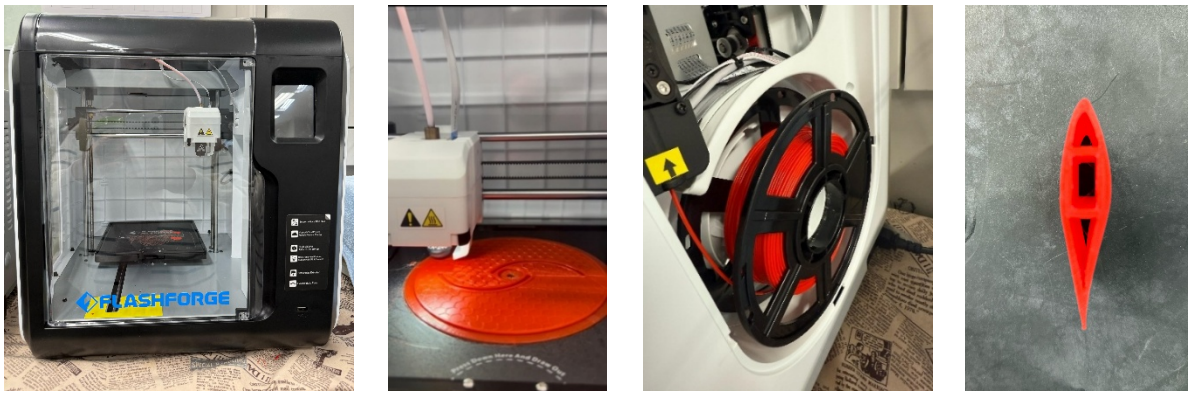

(a) (b) (c)

Fig. 3.3 3D Printer Machine (a), PLA Material (b), and 3D Printing Result of the Darrieus with a Hollow

Subsequently, other models examined to determine the effect of solidity on performance are shown in Fig. 3.4.

(a) (b) (c)

Fig. 3.4 Hybrid Savonius-Darrieus with the Solidity of 0.5 (a), 0.75 (b), and 1 (c)

The term "solidity (σ)" is the ratio of the total blade area to the area of the rotor swept by the blades as described in Eq. (3.4).

$$\sigma = \frac{Nc}{2r} \tag{3.4}$$

N, c, and r represent the number of blades, cord length [m], and radius of the Darrieus turbine [m], respectively.

3.3.2 Direct Current (DC) Generator Loss Assessment

In general, wind turbine performance is analyzed from a mechanical perspective. However, this research provides another approach to measure wind turbine performance, which is the electrical point of view. A DC generator with a maximum voltage of 12 V is used for the generator. It is important to conduct a generator loss test, which is regenerative test, as it affects the turbine's output power. Driving the DC motor under load demonstrates how to test its properties as shown in Fig 3.1.

The test includes the following steps:

A. Total Power Loss Test

This is an initial test. A 5 Ω resistor is attached to the circuit on the generator side. The motor's voltage and current are applied via a DC-stabilized power supply as shown in Fig. 3.5.

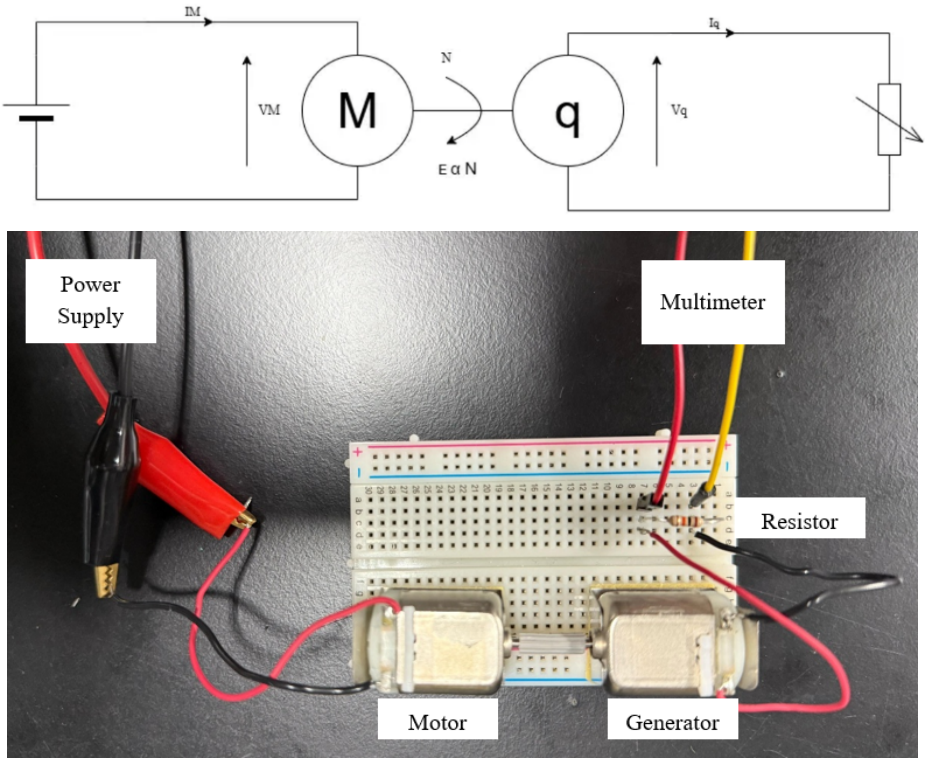

Fig. 3.5 Closed Loop Test

The total amount of all losses is calculated using Eq. (3.5) by considering both generator and motor side.

$$Total\ Power\ Loss = (V_G I_G) - (V_M I_M) \quad (3.5)$$

V_G is the generator voltage [V], I_G is the generator current [A], V_M is the motor voltage [V], and I_M is the motor current [A].

B. Friction Loss Test

The voltage and current are then applied to the motor using a DC-stabilized power supply, and the circuit on the generator is released as shown in Fig. 3.6.

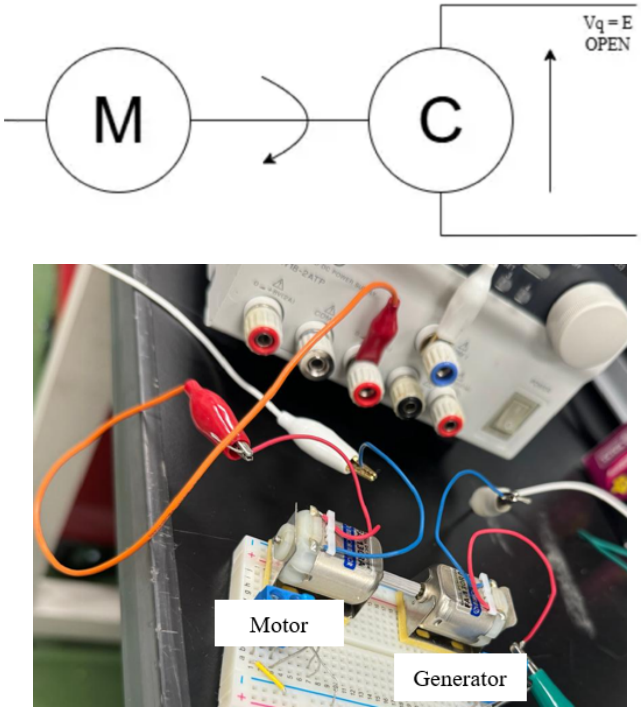

Fig. 3.6 Open Circuit Test

A graph showing the correlation between input voltage and generator speed is used to determine friction loss.

C. Copper Loss Test

A DC-stabilized power supply is connected to the motor, and then voltage and current are applied. By stopping motor rotation and performing a restraint test, only the copper loss, excluding friction loss and iron loss, can be determined. The scheme is shown in Fig. 3.7.

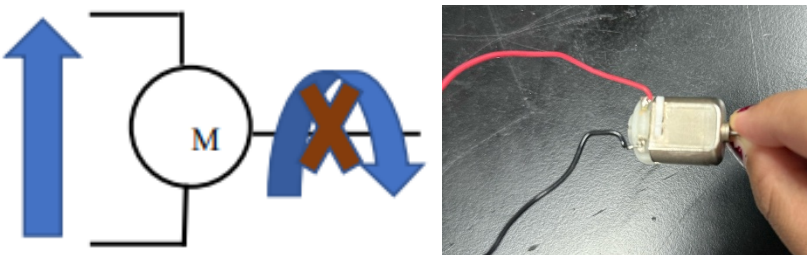

Fig. 3.7 Lock Test

The copper loss coefficient is obtained by dividing the voltage of the motor during the restraint by the current.

D. Iron Loss Test

Copper loss, friction loss, and iron loss occur on the motor and generator sides, respectively. The copper loss is an expression of the current squared, while the iron loss is proportional to the square of the voltage. Since the total loss has already been determined, the friction loss and copper loss can also be determined; the remainder minus them represents the iron loss. Friction loss is tested using a double loaded scheme as shown in Fig. 3.8.

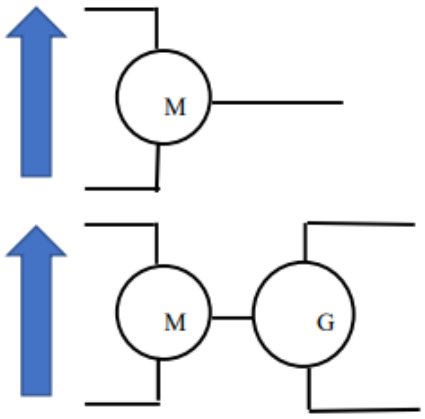

Fig. 3.8 Double Loaded Test

3.3.3 Model Characteristic Investigations

Model characteristic investigations are conducted in the Power System Laboratory's small wind tunnel at Shibaura Institute of Technology as shown in Fig. 3.9.

(a)

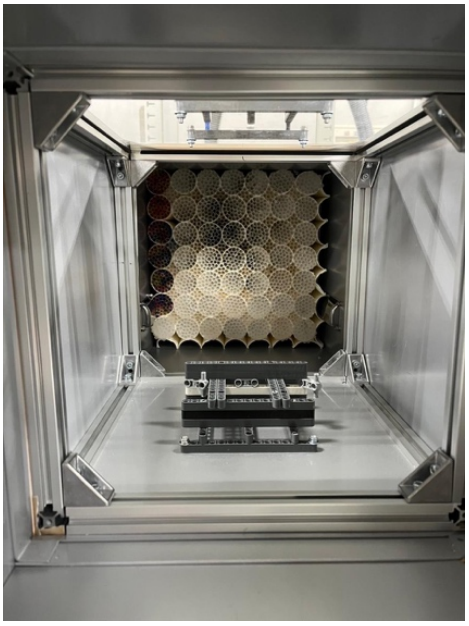

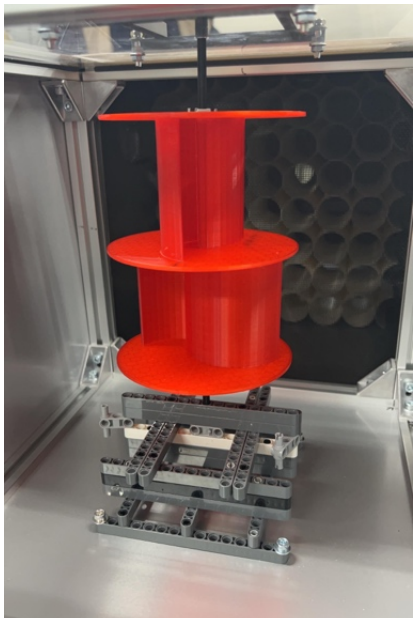

(b) (c)

Fig. 3.9 Overall Wind Tunnel (a), Detailed Honeycomb (b), and test Section Part (c)

The investigations are carried out in a low-speed, open-loop wind tunnel. The dimension of the test section is 30x30x30 cm, with a maximum wind speed of 12 m/s. An anemometer (Fig. 3.10 (a)) is used to assess the flow uniformly in the tested area, and the data shows that the wind distribution is the same at every point, while a tachometer (Fig. 3.10 (b)) is used to measure the rotational speed of the model. The output parameters, such as current and voltage are measured using a multimeter (Fig. 3.10 (c)). At room temperature an air density (ρ) of roughly 1.225 kg/m^3 is maintained using an air conditioner.

(a) (b) (c)

Fig. 3.10 Anemometer (a), Tachometer (b), and Multimeter (c)

Then, a model performance test is carried out using a closed circuit like the scheme in Fig. 3.11 (a). However, using this scheme, the turbine can't reach a higher TSR, so the improvement test is conducted as shown in Fig 3.11 (b).

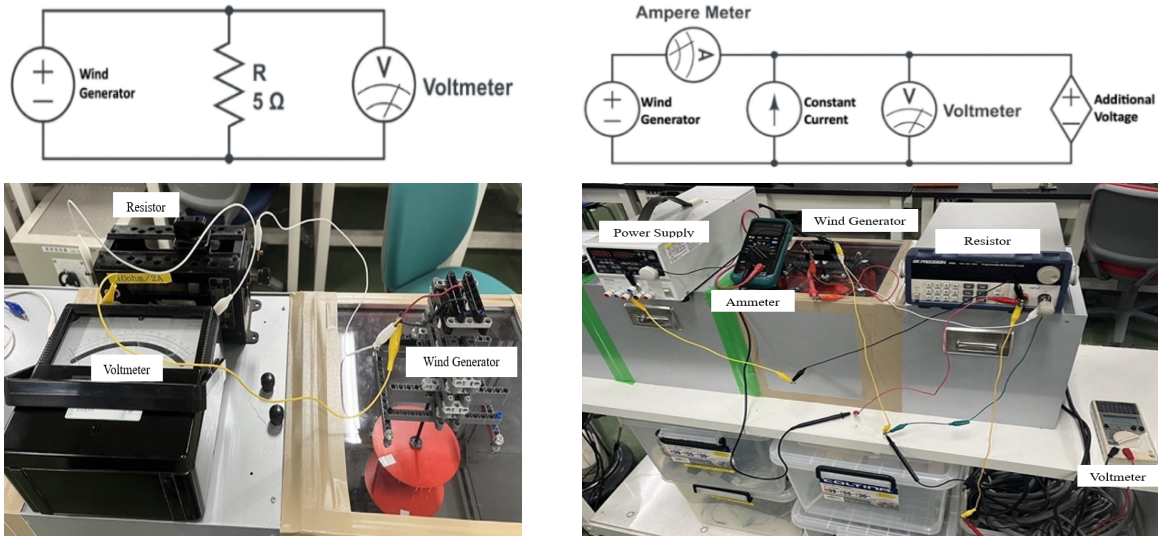

(a) (b)

Fig. 3.11 Basic Circuit (a) and Improved Circuit (b)

In the improvement scheme shown in Fig. 3.11 (b), the constant current source is given as equal to the current produced by the turbine from the first output. Then an initial additional voltage is

also applied, equal to the output voltage in the first circuit, which is then increased gradually so that the rotational turbine also increases.

3.3.4 Parameters

Finally, several parameters are specified to assess the wind turbine's characteristics during the test. Tip speed ratio (TSR) of the turbine is calculated using Eq. (3.6).

$$TSR = \frac{\omega r}{v} \tag{3.6}$$

ω is turbine's rotational speed [rad/s], r is turbine's outer radius [m], and v is wind speed [m/s]. Then, the turbine's output power is calculated, including the motor loss factors as shown in Eq. (3.7).

$$P_T = P_o + K_f\omega + K_c{I_o}^2 + K_i{V_o}^2 \tag{3.7}$$

P_T is turbine extracted power [Watt], P_o is output power [Watt], K_f is friction loss coefficient, K_c is copper loss coefficient, I_O is output current by measurement [A], K_i is the iron loss coefficient, and V_O is output voltage by measurement [V]. After getting turbine's output power, the power coefficient (C_P) is calculated using Eq. (3.8).

$$C_P = \frac{2P_T}{\rho A v^3} \tag{3.8}$$

A is the turbine swept area [m^2], which is the rotor diameter times the height.

3.4 RESULT AND DISCUSSION

3.4.1 DC Generator Loss Assessment Result

Multiple properties are displayed by the DC generator assessment results, including total power loss, friction loss, copper loss, and iron loss. Each loss will be analyzed, but the first thing that needs to be done is to get the total loss. To find out how much total power is lost in the DC generator used, the results of a comparison of the input and output power of two identical DC motors and generator that are coupled are shown in Table 3.1.

Table 3.1 Power Losses Assessment

Total Power Loss Test						
Motor			Generator			Total Power Loss [W]
V_m [V]	I_m [A]	P_m [W]	V_g [V]	V_g [A]	P_g [W]	
1	0.09	0.09	0.19	0.01	0.00	0.09

2	0.12	0.24	0.47	0.02	0.01	0.24
3	0.14	0.41	0.57	0.02	0.01	0.39
4	0.17	0.67	0.77	0.03	0.02	0.65
5	0.22	1.08	0.99	0.03	0.03	1.04

Copper Loss Test

Before Locked		After Locked		Copper Loss Coefficient (K_c)
V [V]	I [A]	V [V]	I [A]	
1	0.02	0.96	0.20	4.80
2	0.02	1.88	0.35	5.37
3	0.03	2.83	0.57	4.96
4	0.03	3.79	0.72	5.26
5	0.04	4.87	0.89	5.47
Average				**5.17**

Friction Loss Test

Non load		Double load		Friction	Rotational Speed	Friction Loss
V [V]	I [A]	V [V]	I [A]	Loss [W]	[rad/s]	Coefficient (K_f)
1	0.02	1	0.04	0.02	120	1.4E-04
2	0.02	2	0.04	0.04	222	1.6E-04
3	0.02	3	0.05	0.07	370	1.9E-04
4	0.02	4	0.06	0.12	629	2.0E-04
5	0.03	5	0.06	0.19	920	2.1E-04
Average						**1.8E-04**

Iron Loss Test

Total Power Loss [W]	Friction Loss (P_f) [W]		Copper Loss (P_{Cu}) [W]		Iron Loss (P_i) [W]	Iron Loss Coefficient (K_i)
	Motor	Generator	Motor	Generator	Motor+Generator	
0.09	0.02	0.02	0.04	0.00	0.02	0.02
0.24	0.04	0.04	0.08	0.00	0.08	0.02
0.39	0.07	0.07	0.09	0.00	0.16	0.02
0.65	0.12	0.12	0.15	0.00	0.25	0.02
1.04	0.19	0.19	0.25	0.01	0.40	0.02
Average						**0.02**

As mentioned before, the total power loss is the accumulation of power friction loss, power copper loss, and power iron loss. Next, each part of the three factors is analyzed. Friction loss graph characteristic is shown in Fig. 3.12.

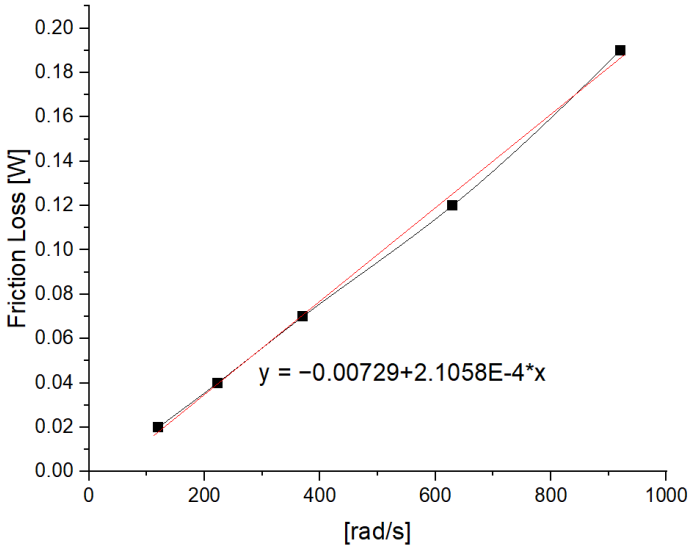

Fig. 3.12 Friction Loss Test Result

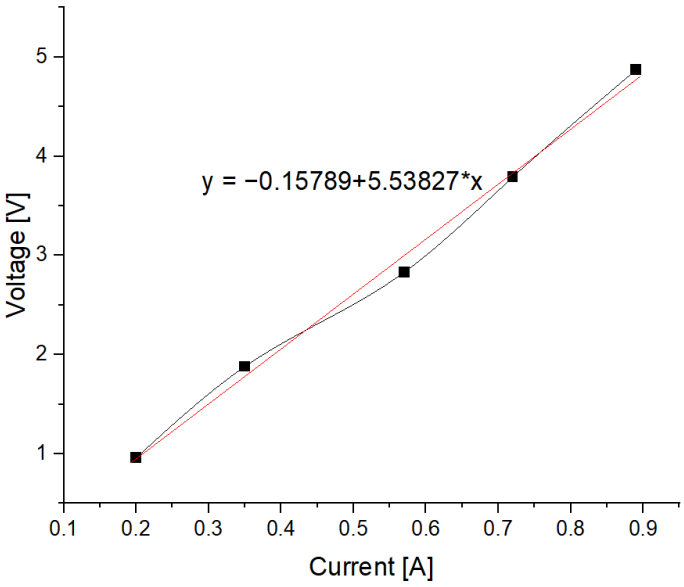

Fig. 3.13 Copper Loss Test Result

Then, the graph in Fig 3.13 is the result of copper loss testing. Since this test is carried out in a locked state, which means the rotation of the motor is restrained, the only loss that arises is

copper loss. In this case, the measured resistance is the copper loss coefficient itself. Thus, the copper loss coefficient value obtained is 5.17.

Finally, because the power friction power copper loss value has been obtained, it is not difficult to determine iron loss. Since the total loss has been obtained, the reduction in total loss due to friction and copper loss of both the motor and generator is iron loss. Next, the iron loss coefficient is obtained by applying Eq. (3.7), and the value obtained is 0.02.

3.4.2 Model Characteristics

When using a testing scheme such as Fig. 3.11 (a), wind speed is varied from 0 to 12 m/s. The hybrid Savonius-Darrieus model can start rotating at a wind speed of around 3 m/s, while the Darrieus starts rotating at a wind speed of around 4.5 m/s. Test results using the scheme in Fig. 3.11 (b) shows that rotational speed increases with increasing wind speed, as does the power extracted by the turbine. However, using this scheme can provide a maximum TSR of only 1. This value is not enough to know the characteristics of both hybrid Savoinus-Darrieus and Darrieus, because both are types of turbines that have good performance at high TSR.

By applying an improvement method in measurement shown in Fig. 3.11 (b), the turbine receives power from outside which boosts rotational speed and a higher TSR can be achieved. In this case, wind speed 4.4 m/s is used for the measurement. When additional current and voltage are equal to the turbine output shown in the scheme in Fig. 3.11 (b), a positive current and voltage arise. However, if the additional current is maintained constant while the voltage is gradually increased, the measured output current will decrease whereas the output voltage will increase. This happens because the additional power given to increase the turbine rotation is getting bigger, and the value is greater than the power produced by the turbine; this condition is called assisting the turbine with external power to get a higher TSR. Next, the original power generated by the turbine itself is calculated using Eq. (3.8) by considering the DC generator loss factors as mentioned in the methodology.

Then, the performance of the models is presented in the TSR vs. C_P graphs. Basically, hybrid Savonius Darrieus and single Darrieus wind turbines have the characteristics of being able to achieve a TSR of 3 to 4. In the low wind speeds experiment, which is 0–12 m/s, the measured TSR range cannot cover the entire working area of the model, as shown in Fig. 3.14 (a). Furthermore, by applying improvement method in measurement through the application of the

circuit scheme shown in Fig. 3.11 (b), the TSR range can increase and cover the entire working area of the models, as indicated in Fig. 3.14 (b).

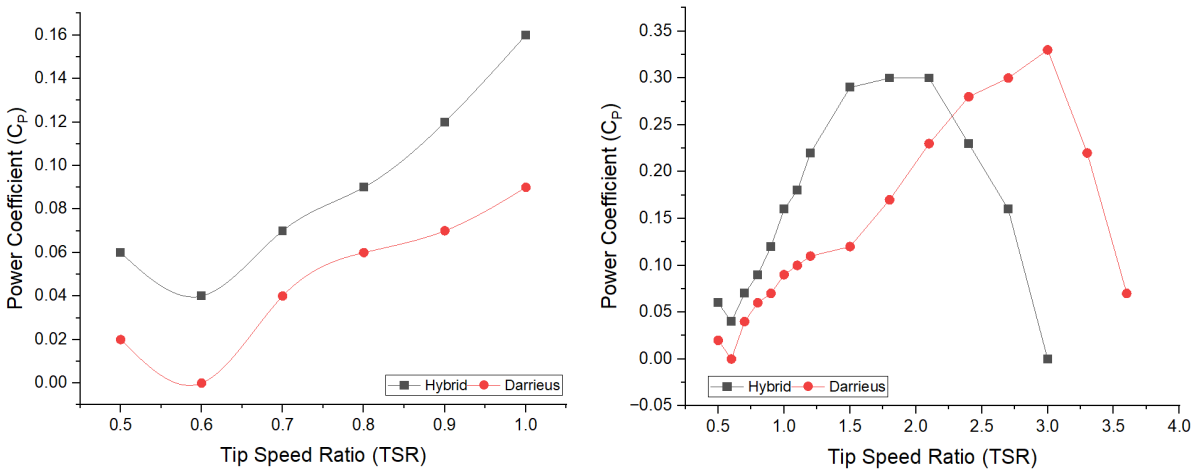

Fig. 3.14 Models Performance Test Results Before (a) and After (b) Improvement Method

The results of this test are validated with previous research [18], where a numerical study of the hybrid Savonius-Darrieus was carried out at several rotor radius ratio conditions. This method is satisfying because the graphical results shown in Fig. 3.14 (b) have the same characteristics as the previous study, which is that Hybrid Savonius-Darrieus with rotor radius ratio of 0.5 has a maximum C_P on TSR around 1.5 and becomes 0 TSR about 3. Thus, the results show that the maximum C_P of the hybrid Savonius-Darrieus and single Darrieus is 0.30 at TSR 0.15 and 0.33 at TSR 3.3, respectively.

By applying this method, the total power that can be generated by the hybrid Savonius-Darrieus and single Darrieus models for all TSR at 4.40 m/s wind velocity is 26.17 Watts and 26.11 Watts, respectively. Without improvement, the model can only work at a maximum TSR of 1, so that the power produced by the hybrid Savonius-Darrieus and single Darrieus models is 6.35 Watts and 3.33 Watts, respectively. Thus, this improvement method can increase the working range of the model by four times. This means that the application of this method also plays a role in saving fossil energy along with increasing the power produced in the amount of 19.82 Watts and 22.78 Watts for the hybrid Savonius-Darrieus and single Darrieus models, respectively.

However, the efficiency of the turbine also depends on several factors, such as its model, dimensions, and configuration, as explained in research [6], [19], [20], [21]. This method has no limitations regarding this matter for investigation at low wind speeds. This method can be applied to various VAWT turbine models. But the most important point is that it is necessary to adjust the generator capacity to the turbine output power. In addition, generator characterization and test methods can be carried out as described.

3.4.3 Analyzing the Effect of Solidity on the Performance of Hybrid Savonius-Darrieus

After successfully applying the proposed measurement method to the main model, the effect of solidity on the performance of the hybrid Savonius-Darrieus turbine was tested, yielding the following results.

A. Moment Coefficient

A wind turbine's moment coefficient is largely dependent on its solidity. It is important to note that there is an upper limit to the increase in moment coefficient with increasing solidity. In Fig. 3.15, the correlation between solidity and moment coefficient is clearly depicted.

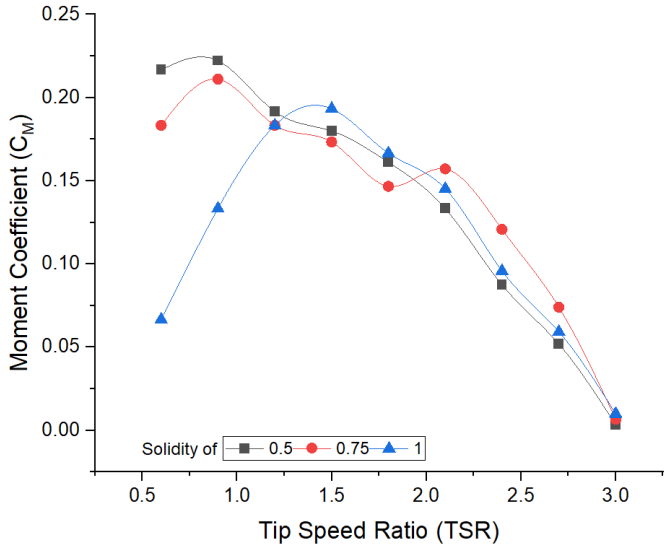

Fig. 3.15 Moment Coefficient Graph of All Models

Based on this experiment, the initial moment coefficient of the models exhibits a notable inverse relationship with solidity, suggesting a decline as solidity values increase. This trend is indicative of the intricate aerodynamic interactions within the turbine system. Notably, the model characterized by a solidity of 0.5 displays the highest initial moment coefficient, reaching

0.22, whereas the model featuring a solidity of 1 manifests the lowest initial moment coefficient, recorded at 0.07.

Specifically, augmenting solidity in the hybrid model entails augmenting the number of Darrieus blades, thus altering the balance between lift and drag forces inherent in the Savonius rotor. As solidity increases, the prominence of Darrieus blades becomes more pronounced, potentially compromising the optimal performance of the Savonius blades due to disrupted airflow patterns and increased aerodynamic drag. Consequently, this may contribute to a diminished initial moment coefficient in the hybrid configuration.

B. Power Coefficient

Generally, as solidity increases, the maximum power coefficient tends to increase as well as depicted in Fig 3.16.

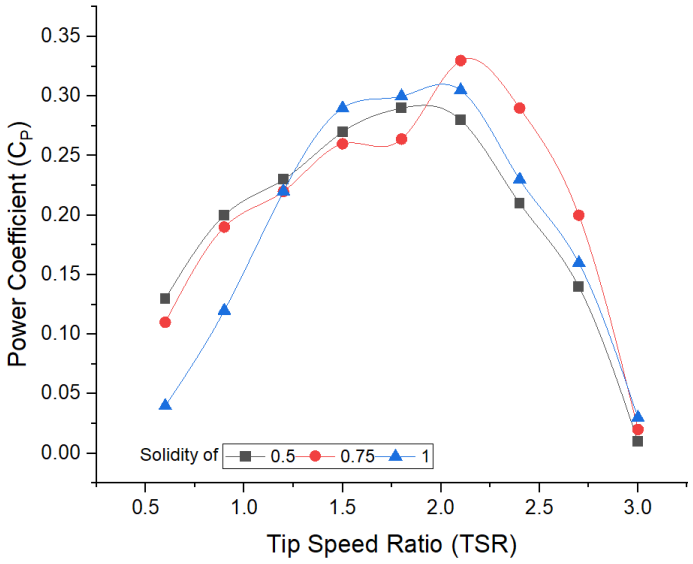

Fig. 3.16 Power Coefficient Graph of all Models

This is due to the increased number of blades generating lift forces on the turbine. As solidity increases, more blade surface area is packed into the same rotor area, leading to higher aerodynamic forces being exerted on the turbine. This often results in improved power extraction capabilities, especially at optimal operational conditions. However, there is a point of diminishing returns where excessively high solidity can lead to increased aerodynamic losses, thus diminishing overall efficiency. Fig 3.16 demonstrates that the maximum attainable power coefficient varies significantly with different solidity values. For instance, turbines with a

solidity of 0.75 achieve the highest maximum power coefficient of 0.33 at a tip speed ratio of 2.1. Conversely, turbines with a lower solidity of 0.5 exhibit a lower maximum power coefficient of 0.29, occurring at a lower tip speed ratio of 1.8.

C. Output Power

The influence of solidity on the power output generated by the turbine is illustrated in Fig. 3.17. Through Fig 3.17, it is evident that the model capable of extracting the highest power output is at solidity 0.75. The solidity 0.5 model can rotate at a lower wind velocity of 3.3 m/s, whereas the solidity 0.75 and 1 models can rotate at a wind velocity of 4.4 m/s.

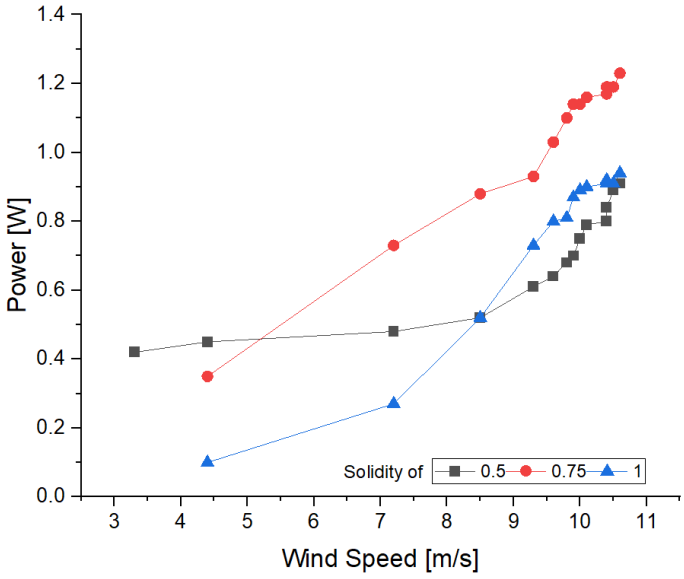

Fig. 3.17 Output Power of All Models

Additionally, it can be observed that at low wind speeds, the model with solidity 0.5 can generate the highest power output. This phenomenon is attributed to the dominant performance of the Savonius component compared to the Darrieus component in hybrid models with lower solidity, providing a favorable initial starting point. However, with increasing wind speed, the power generated becomes less significant. Conversely, the model with solidity 0.1 experiences a significant increase in output power with increasing wind speed. This occurs because the lift force generated by the Darrieus component is more dominant than the Savonius component in hybrid models with larger solidity. However, it should be highlighted that increasing the solidity

of the hybrid turbine can also increase its weight, thus creating internal resistance to rotation. Therefore, the performance of the model with solidity 0.75 is considered the most ideal.

3.5 CONCLUSION

This study evaluated the performance of a hybrid Savonius-Darrieus VAWT at high tip speed ratios (TSR) using experimental testing. Results show improved self-starting but reduced aerodynamic efficiency due to Savonius drag. A regenerative testing method accurately measured power loss, enhancing evaluation precision. The study also found that increasing solidity improved the maximum power coefficient (C_P), with an optimal value of 0.75 achieving $C_P = 0.33$ at TSR 2.1. However, excessive solidity reduced initial torque and increased rotational resistance. An improved measurement circuit expanded the TSR range for better turbine assessment. These findings enhance hybrid VAWT optimization, contributing to efficient wind energy solutions for low-wind environments.

REFERENCES

[1] D. H. Didane, S. Mohd, Z. Subari, N. Rosly, M. F. A. Ghafir, and M. F. M. Masrom, "An aerodynamic performance analysis of a perforated wind turbine blade," *IOP Conf. Ser.: Mater. Sci. Eng.*, vol. 160, no. 1, p. 012039, Nov. 2016, doi: 10.1088/1757-899X/160/1/012039.

[2] M. Barzegar-Kalashani, M. Seyedmahmoudian, S. Mekhilef, A. Stojcevski, and B. Horan, "Small-scale wind turbine control in high-speed wind conditions: A review," *Sustainable Energy Technologies and Assessments*, vol. 60, p. 103577, Dec. 2023, doi: 10.1016/j.seta.2023.103577.

[3] S. F. Bello *et al.*, "Optimizing vertical axis wind turbines for urban environments: Overcoming design challenges and maximizing efficiency in low-wind conditions," *GSC Advanced Research and Reviews*, vol. 21, no. 1, Art. no. 1, 2024, doi: 10.30574/gscarr.2024.21.1.0384.

[4] Z. Zhao, D. Wang, T. Wang, W. Shen, H. Liu, and M. Chen, "A review: Approaches for aerodynamic performance improvement of lift-type vertical axis wind turbine," *Sustainable Energy Technologies and Assessments*, vol. 49, p. 101789, Feb. 2022, doi: 10.1016/j.seta.2021.101789.

[5] M. Ahmad, A. Shahzad, F. Akram, F. Ahmad, and S. I. A. Shah, "Design optimization of Double-Darrieus hybrid vertical axis wind turbine," *Ocean Engineering*, vol. 254, p. 111171, Jun. 2022, doi: 10.1016/j.oceaneng.2022.111171.

[6] F. Wenehenubun, A. Saputra, and H. Sutanto, "An Experimental Study on the Performance of Savonius Wind Turbines Related With The Number Of Blades," *Energy Procedia*, vol. 68, pp. 297–304, Apr. 2015, doi: 10.1016/j.egypro.2015.03.259.

[7] A. Tripathi, P. Das, T. Aggarwal, and Sahil, “Efficiency enhancement of a hybrid Vertical axis wind turbine by utilizing Optimum parameters,” *Materials Today: Proceedings*, vol. 62, pp. 3582–3588, Jan. 2022, doi: 10.1016/j.matpr.2022.04.406.

[8] A. Pallotta, D. Pietrogiacomi, and G. P. Romano, “HYBRI – A combined Savonius-Darrieus wind turbine: Performances and flow fields,” *Energy*, vol. 191, p. 116433, Jan. 2020, doi: 10.1016/j.energy.2019.116433.

[9] M. P. Thomai, S. Sivamani, and H. Venkatesan, “Dataset on the measurement of power in the hybrid vertical axis wind turbine in natural wind,” *Data in Brief*, vol. 31, p. 105922, Aug. 2020, doi: 10.1016/j.dib.2020.105922.

[10] T. Izhar, M. Ali, M. Sohaib, and A. Nazir, “Development of a motor test bench to measure electrical/mechanical parameters,” in *2017 International Conference on Energy Conservation and Efficiency (ICECE)*, Nov. 2017, pp. 64–67. doi: 10.1109/ECE.2017.8248830.

[11] E. V. Beyerleyn, P. V. Tyuteva, and B. S. Dorzieva, “Feasibility demonstration of back-to-back method for induction traction motors testing,” *IOP Conf. Ser.: Mater. Sci. Eng.*, vol. 1019, no. 1, p. 012051, Jan. 2021, doi: 10.1088/1757-899X/1019/1/012051.

[12] G. J. Wakileh, “Harmonics in rotating machines,” *Electric Power Systems Research*, vol. 66, no. 1, pp. 31–37, Jul. 2003, doi: 10.1016/S0378-7796(03)00069-5.

[13] G. J. Wakileh, *Power Systems Harmonics: Fundamentals, Analysis and Filter Design*. Springer Nature, 2019.

[14] G. P. Shultz, “CHAPTER 1 - Fundamental Concepts: Transformers,” in *Transformers and Motors*, G. P. Shultz, Ed., Boston: Newnes, 1989, pp. 3–22. doi: 10.1016/B978-0-08-051958-6.50004-4.

[15] Q. Gao, X. Wang, C. Gu, and Y. Zhang, “Copper loss analysis and loss separation method in a dynamic process of ultra-high speed motor with slotless stator,” *IET Electric Power Applications*, vol. 17, no. 4, pp. 464–473, 2023, doi: 10.1049/elp2.12278.

[16] J.-B. Boni, A. Neurouth, C. Changenet, and F. Ville, “Experimental investigations on churning power losses generated in a planetary gear set,” *JAMDSM*, vol. 11, no. 6, pp. JAMDSM0079–JAMDSM0079, 2017, doi: 10.1299/jamdsm.2017jamdsm0079.

[17] Q. Xin and C. F. Pinzon, “10 - Improving the environmental performance of heavy-duty vehicles and engines: particular technologies,” in *Alternative Fuels and Advanced Vehicle Technologies for Improved Environmental Performance*, R. Folkson, Ed., Woodhead Publishing, 2014, pp. 279–369. doi: 10.1533/9780857097422.2.279.

[18] E. N. Irawan, S. Sitompul, K.-I. Yamashita, and G. Fujita, “The Effect of Rotor Radius Ratio on The Performance of Hybrid Vertical Axis Wind Turbine Savonius-Darrieus NREL S809,” *Journal of Energy and Power Technology*, vol. 5, no. 1, Art. no. 1, Jan. 2023, doi: 10.21926/jept.2301001.

[19] I. Bayati, M. Belloli, L. Bernini, and A. Zasso, “Aerodynamic design methodology for wind tunnel tests of wind turbine rotors,” *Journal of Wind Engineering and Industrial Aerodynamics*, vol. 167, pp. 217–227, Aug. 2017, doi: 10.1016/j.jweia.2017.05.004.

[20] S. Brusca, R. Lanzafame, and M. Messina, “Design of a vertical-axis wind turbine: how the aspect ratio affects the turbine’s performance,” *Int J Energy Environ Eng*, vol. 5, no. 4, pp. 333–340, Dec. 2014, doi: 10.1007/s40095-014-0129-x.

[21] D. Puspitasari and K. Sahim, “Effect of Savonius blade height on the performance of a hybrid Darrieus-Savonius wind turbine,” *Journal of Mechanical Engineering and Sciences*, vol. 13, no. 4, Art. no. 4, Dec. 2019, doi: 10.15282/jmes.13.4.2019.09.0465.

CHAPTER 4
UNLOCKING THE POWER OF THE WIND: INNOVATIONS IN SMART HYBRID VERTICAL AXIS WIND TURBINES

4.1 CHAPTER INTRODUCTION

In general, there are two primary kinds of wind turbines: vertical-axis wind turbines (VAWT) and horizontal-axis wind turbines (HAWT) [1]. The optimal HAWT has an efficiency of approximately 0.6 according to the Betz Limit calculation [2]; however, the VAWT has an efficiency of 25% less than the HAWT [3]. The HAWT design's ability to transform wind energy into electrical energy over a complete rotation of the blade's accounts for its higher efficiency when compared to VAWT [4]. It is undeniable, nonetheless, that VAWT has more benefits than HAWT [5]. These benefits include the fact that VAWT is simpler to maintain, doesn't require adjusting for the wind's direction, produces less noise, and can work at low wind speeds [6].

Among all types of VAWT, there are two types that have been the most studied, namely Savonius and Darrieus [7]. Savonius has semicircle-shaped blades, so it is very easy to make [8]. Savonius works based on the drag force so that it has a very large torque and requires a low wind speed to start the rotation [9]. Unfortunately, the efficiency of Savonius is still low, which is around 0.1 – 0.2 [10]. Meanwhile, Darrieus works based on the lift force and is not capable of self-starting if the wind speed is below 4 m/s [11]. However, Darrieus efficiency is the best among all types of VAWT turbines, which is around 0.4 – 0.45 [12]. Lift-type VAWTs are known for their ability to operate at higher rotational speeds compared to drag-type VAWTs [13].

By combining the positive side of Savonius and Darrieus, many researchers are developing hybrid SavoniusDarrieus [14]. The purpose of developing the hybrid Savonius Darrieus is to obtain a VAWT turbine that can self-start at low wind speeds like the Savonius and has high efficiency like the Darrieus. Many methods have been used to optimize the performance of the hybrid Savonius-Darrieus, such as adjusting the position of the turbine arrangement [15], adding the Darrieus pitch angle [16], and adjusting the height of the Savonius blade [17].

Unfortunately, the conventional hybrid Savonius Darrieus cannot provide as good efficiency as single Darrieus [2] because at high TSR, Savonius inhibits Darrieus rotation. This case is caused by the Savonius character which cannot rotate a TSR exceeding 1 nor beyond the

speed of the wind that hits it [18]. M. Ahmad et. all [2] conducted both experimental and computational investigation into a unique combined configuration of Savonius-Darrieus. The proposed hybrid model included DU 06-W-200 airfoil blades internally, while externally, it featured three NACA0018 airfoil blades. Compared to the conventional Darrieus H-rotor and hybrid VAWT model, this innovative combined model showcased enhanced performance criteria, such as the power coefficient (C_P), dynamic torque coefficient (C_T), and static torque coefficient (C_{TS}), with improvements ranging from approximately 11 – 13% across a wide range of wind speeds. Moreover, the presence of positive values across all azimuths indicated that the proposed hybrid model possessed self-starting capabilities.

Subsequently, Ahmad M and Zafar MH [4] conducted improvement through a computational study of the hybrid VAWT model, utilizing a three-bladed Darrieus configuration as both external and internal rotors. With a tip speed ratio of 3, an efficiency peak of 0.475 was achieved, outperforming the Savonius-Darrieus hybrid model. However, the power coefficient generated at an initial Tip Speed Ratio is roughly 0.1, which is not much different from the conventional Savonius-Darrieus hybrid.

The authors then used the CFD method to compare the performance of a single Darrieus design with a hybrid Savonius-Darrieus configuration at high TSR [19]. The model utilized in study [20] was employed with a 0.5 rotor radius ratio. Based on the results, the hybrid model displayed higher flow velocity around the blade at higher TSR compared to the single Darrieus model. Conversely, during high TSR, there was a rise in the pressure surrounding the single Darrieus, leading to an increase in torque. A detailed analysis of the study suggests that the best-performing hybrid VAWT model is distinguished by attaining the greatest maximum power coefficient when operating at high tip speed ratios, and by having substantial starting torque at lower tip speed ratios. Hence, this research addresses these challenges by introducing the Smart Hybrid VAWT. This innovative design enhances the field of VAWTs by aiming to improve the efficiency of conventional hybrid VAWTs through the implementation of a rotor switching mechanism.

4.2 THE CONCEPT OF SMART HYBRID VAWT

Vertical-axis wind turbines are particularly suitable for urban environments and regions with low wind speeds [21], as they do not require yaw mechanisms to orient themselves with

wind direction [22]. The two most studied VAWT types are the Savonius and Darrieus turbines [29].

- **Savonius Turbine:** Operates based on drag force, generating high starting torque at low wind speeds. However, its power efficiency is relatively low, ranging from approximately 10% to 20%.
- **Darrieus Turbine:** Utilizes lift force to achieve greater efficiency, typically between 40% and 45%, but suffers from self-starting issues at low wind speeds.

A hybrid Savonius-Darrieus turbine integrates the strengths of both turbine types, aiming to enhance performance under fluctuating wind conditions [15]. This combination facilitates self-starting through the Savonius component while benefiting from the higher efficiency of the Darrieus rotor. However, at higher tip speed ratios (TSR), the drag-inducing nature of the Savonius rotor can hinder the rotation of the Darrieus component, thereby reducing overall efficiency [23].

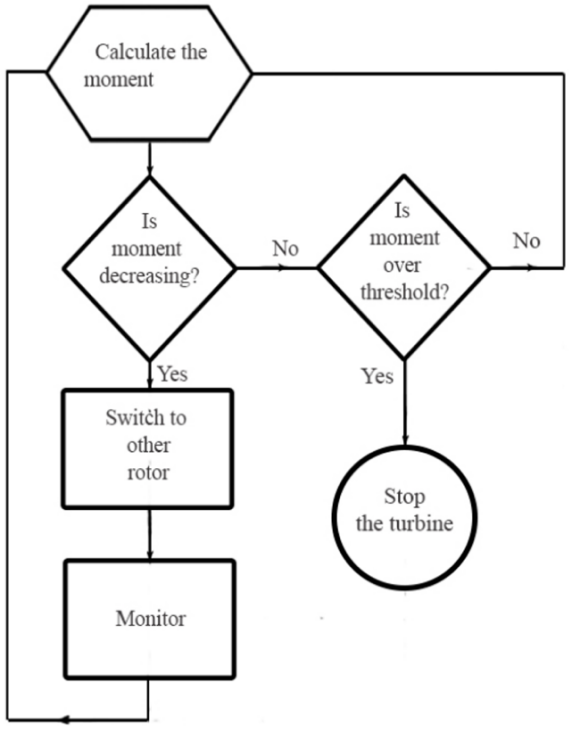

Fig. 4.1 Control Algorithm for the Smart Hybrid Turbine [24]

To address the efficiency limitations of hybrid configurations at high TSRs, the Smart Hybrid VAWT concept was developed by A. Hosseini and N. Goudarzi [24], incorporating an

electromagnetic rotor switching mechanism. This system ensures that the Savonius rotor operates exclusively at low wind speeds, where its high starting torque is advantageous, and automatically disengages at higher TSRs to allow the Darrieus rotor to function with minimal aerodynamic resistance with the control algorithm as shown in Fig. 4.1.

Computational fluid dynamics (CFD) simulations and experimental analyses have demonstrated that integrating this rotor switching mechanism enhances power efficiency by up to 40% and extends the operational range of the turbine to TSR 6. This represents a significant improvement over conventional hybrid turbines, which typically experience efficiency losses at higher TSRs. The switching process is governed by a sensor-based control system that determines the optimal transition between operational modes, ensuring aerodynamic efficiency across a broad spectrum of wind conditions. This adaptive approach enhances the overall energy capture capability and reliability of hybrid wind turbines, making them more suitable for real-world applications.

4.3 METHODOLOGY

4.3.1 Model Specifications

The detailed specifications of this innovative hybrid model are comprehensively outlined in Table 4.1.

Table 4.1 Model Specifications

Configuration	Feature
Savonius	
Number of Blades	2
Number of Stages	2
Radius (R_S)	5 cm
Height (h_S)	14 cm
Overlap (e)	0.2
Darrieus	
Number of Blades	3
Radius (R_D)	10 cm
Cord Length (c)	5 cm
Height (h_D)	15.4 cm

The research employs a sophisticated compact hybrid wind turbine model that integrates both Savonius and Darrieus designs. As seen in Fig. 4.2, the hybrid configuration uses the Savonius for the inner rotor and the Darrieus for the outer rotor. This design approach aims to combine the advantageous features of both Savonius and Darrieus turbines to enhance overall efficiency and performance.

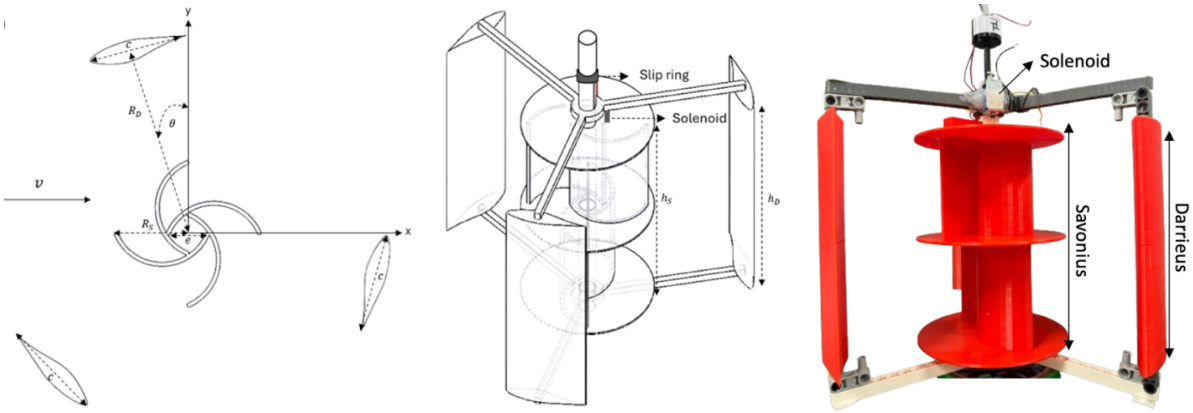

(a) (b) (c)

Fig. 4.2 2D (a) and 3D (b) Design, 3D Printing of Smart Hybrid Model (c)

The overlap, defined as the relative distance between two adjacent Savonius blades [25] at 0.2 times their total diameter, is implemented to achieve this distance of 2cm. The Darrieus blades are positioned with an angle of attack ($\boldsymbol{\alpha}$) of 0° respect to the airflow, while they are incrementally angled (°) at 15° with respect to the Savonius component. The NREL S809 airfoil type Darrieus is employed due to its favorable performance characteristics at high wind speeds [26].

Based on the literature review conducted, separating the rotation of the Savonius from the Darrieus when reaching high rotational speeds can enhance the efficiency of the hybrid turbine. A solenoid coil is employed for this purpose. The solenoid coil is utilized to combine and separate the rotation of the Savonius rotor from that of the Darrieus rotor. Consequently, to prevent any influence on the rotational dynamics of the main rotor, the solenoid is integrated with a slip ring mechanism. This arrangement ensures that the solenoid's operation does not impede the overall performance of the rotor system.

4.3.2 Experimental Arrangement

A. Model Performance Investigations

These experimental investigations are conducted within a wind tunnel featuring a cross-sectional area measuring 30x30 cm. Wind velocities are systematically varied across a range of 3 – 12 m/s to capture a spectrum of operating conditions. Concurrently, meticulous attention is paid to maintaining ambient conditions at a controlled temperature, achieved through the regulation of room temperature utilizing an air conditioning system to ensure the accuracy of the air density value for extracted power calculations [27].

The power coefficient of the model can be analyzed using the circuit scheme depicted in Fig. 4.3.

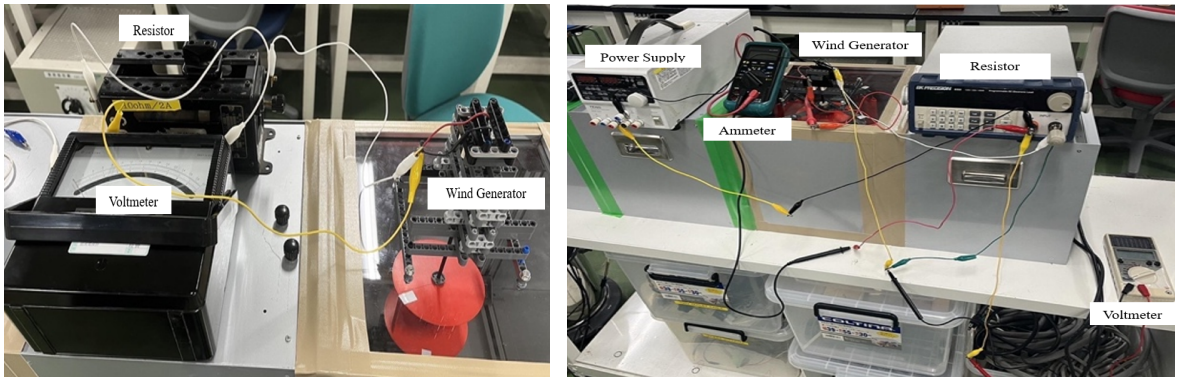

(a) (b)

Fig. 4.3 Circuit Diagram for Low TSR (a) and High TSR (b)

The circuit scheme in Fig 4.3 (a) is employed at low rotational speeds. Subsequently, at higher rotational speeds, circuit scheme in Fig. 4.3 (b) is applied. The utilization of circuit scheme ini Fig. 4.3 (b) serves the purpose of extending the measurement capabilities to encompass high tip speed ratios. This is achieved through the strategic injection of power into the model, thereby augmenting its rotational speed. The power injection is administered by providing a constant electric current (equivalent to the maximum current that the model can generate based on measurements using circuit scheme 4.3 (a)) while gradually increasing the voltage source until a gradual enhancement in the model's rotational speed is observed. Following this, the output current $(\boldsymbol{I_O})$ and voltage $(\boldsymbol{V_O})$ generated by the model or wind generator are measured by

ammeter and voltmeter to be considered for calculating the power extracted ($\boldsymbol{P_O}$), moment coefficient ($\boldsymbol{C_M}$), and power coefficient ($\boldsymbol{C_P}$) and by the model.

B. Rotor Switching Design

To achieve optimal turbine performance across a range of operational conditions, a sophisticated rotor switching mechanism is employed as a smart hybrid model. This mechanism facilitates a seamless transition from the hybrid mode, characterized by the joint operation of the Savonius and Darrieus rotors, to the single Darrieus mode. This transition is guided by the operational paradigm outlined in the block diagram depicted in Fig. 4.4.

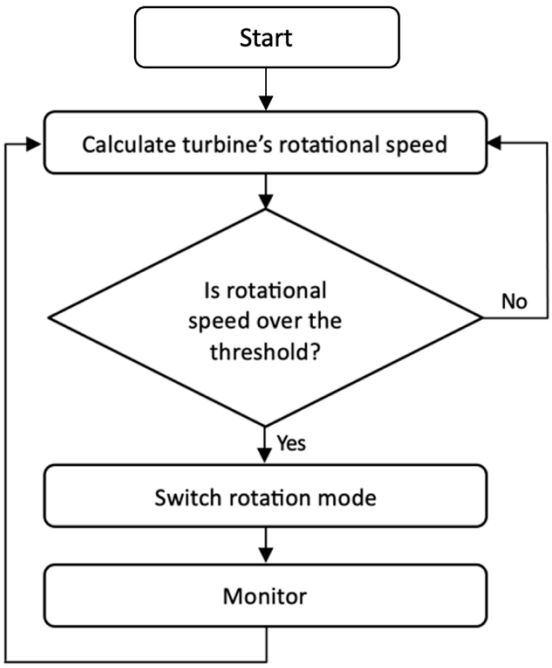

Fig. 4.4 Switching Rotor Scheme

The turbine operation has two distinct modes based on the rotational speed condition as follows:

- **Hybrid mode:** This mode is engaged when the rotational speed remains below the threshold. In this configuration, both the Savonius and Darrieus rotors collaborate to harness wind energy efficiently, leveraging the complementary characteristics of each rotor design.
- **Single Darrieus mode:** As the rotational speed surpasses the threshold, the turbine seamlessly transitions to the single Darrieus mode. Upon achieving high rotational speeds, the rotation of Savonius is made independent from that of Darrieus. In this mode, the

operation is solely reliant on the Darrieus rotor. This mode is specifically optimized for higher rotational speeds, where the Darrieus rotor's design excels in extracting wind energy effectively.

The switching of the rotor configuration is orchestrated by precisely controlling the rotation of the Savonius rotor relative to the Darrieus. This control is achieved through a meticulously designed circuit configuration, as illustrated in the schematic depicted in Fig. 4.5.

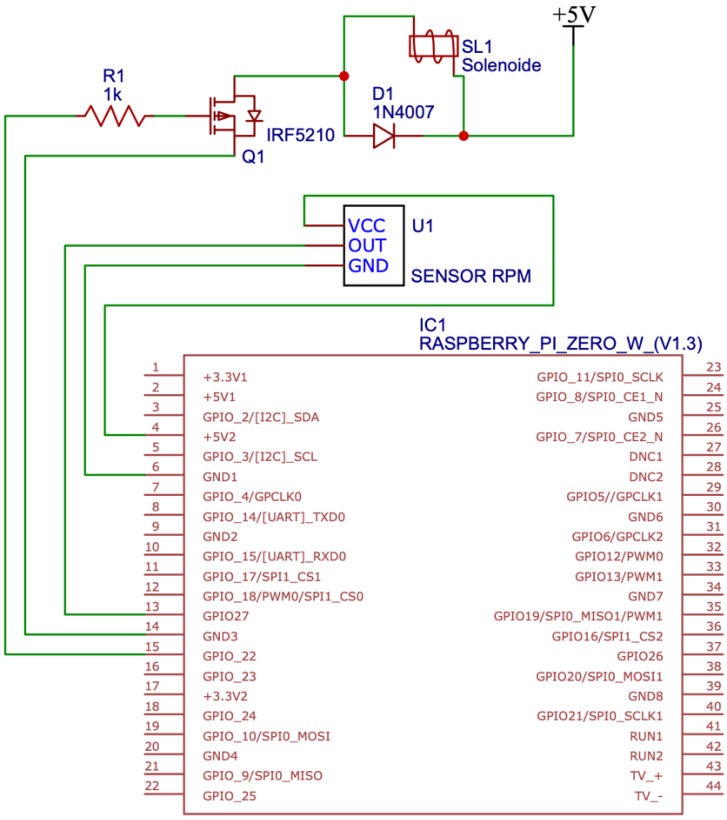

Fig. 4.5 Switching Rotor Circuit Scheme

The idea is to utilize a photoresistor to measure the turbine's rotational speed. The data collected is then processed by an Arduino, serving as the microcontroller. Unlike A. Hosseini and N. Goudarzi's research [24], which employs an electromagnetic switching mechanism, this study utilizes a solenoid to engage and disengage the turbine's rotational modes. Based on this processing, the Arduino generates a response in the form of an output that either activates or deactivates the solenoid. Therefore, this main mechanism is the utilization of a solenoid, a crucial element that makes it easier for the Savonius rotor to engage or disengage from the

Darrieus rotor in accordance with operational demands. This precise control over the rotor configuration ensures that the turbine operates optimally across a wide range of wind conditions, maximizing its overall efficiency and performance.

To protect vertical axis wind turbines from overspeed and structural damage during high wind conditions, one effective strategy is the implementation of electrical braking through generator load control. This method relies on increasing the electrical load on the generator to create a resistive torque that slows down rotor rotation. In general, the system consists of a generator connected to a power controller and a set of resistive braking loads as shown in Fig. 4.6.

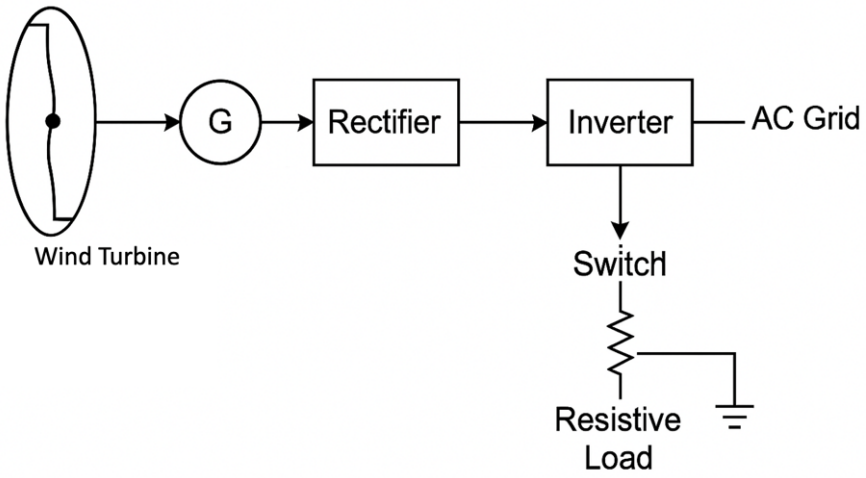

Fig. 4.6 Scheme of Electrical Braking Through Generator Load Control

When wind speed or rotor RPM exceeds a predefined safety threshold, a control unit, typically a microcontroller or programmable logic controller (PLC) detects the condition and activates the braking circuit. The electrical energy produced by the generator is then diverted from the standard output pathway into a dump load, which is often composed of high-power resistors. These resistors convert the excess kinetic energy into heat, effectively applying a braking force on the rotor through increased electromagnetic resistance in the generator.

This approach is advantageous because it does not require mechanical components such as friction brakes, reducing the complexity and maintenance burden of the system. Moreover, electrical braking can be precisely controlled and automated based on real-time data from wind speed sensors, RPM sensors, voltage, or current feedback. It is especially suitable for small to

medium-scale wind turbines, where weight, cost, and simplicity are critical considerations. By limiting the rotor speed through load regulation, this method prevents mechanical overstress and ensures operational safety, particularly during sudden gusts or extreme weather events.

Together, these two mechanisms form a complementary protection strategy. The rotor switching system mitigates aerodynamic overload, while the electrical braking system offers dynamic speed control through generator feedback. When integrated into a single intelligent control architecture, they can ensure that hybrid VAWTs remain structurally safe, efficient, and adaptable across a wide range of wind conditions.

C. Parameters

The primary metric utilized for assessing the efficiency of the model lies in the power coefficient ($\boldsymbol{C_P}$) [9], derived through the application of Eq. (4.1).

$$C_P = \frac{2P_T}{\rho A v^3} \tag{4.1}$$

$\boldsymbol{\rho}$ is a density of air [1.225 kg/m^3], $\boldsymbol{v}$ stands for the wind velocity [m/s], and $\boldsymbol{A}$ represents the swept area of the turbine [m^2], which is the result of multiplying the diameter of the rotor by its height. On the other hand, $\boldsymbol{P_T}$, representing turbine's output power [W], is ascertained via empirical measurements conducted employing the methodology outlined in Fig. 4.3 (b). However, it's imperative to acknowledge that $\boldsymbol{P_T}$ is subject to modulation by inherent loss factors intrinsic to the DC generator [28] under consideration. Consequently, its determination necessitates recourse to Eq. (4.2).

$$P_T = P_O + K_f \omega + K_c {I_O}^2 + K_i {V_O}^2 \tag{4.2}$$

$\boldsymbol{P_O}$, $\boldsymbol{I_O}$, and $\boldsymbol{V_O}$ denote the recorded power output, current, and voltage of the turbine, respectively. The DC generator employed exhibits specific loss factors [29], including a friction loss coefficient ($\boldsymbol{K_f}$) of 1.8E-04, a copper loss coefficient ($\boldsymbol{K_c}$) of 5.17, and an iron loss coefficient ($\boldsymbol{K_i}$) of 0.02.

Furthermore, the model's performance evaluation extends to the analysis of the tip speed ratio (TSR), computed utilizing Eq. (4.3).

$$TSR = \frac{\omega r}{v} \tag{4.3}$$

In this context, $\boldsymbol{\omega}$ symbolizes the turbine rotation in radians per second while $\boldsymbol{r}$ represents the outer radius of the turbine in meters. Finally, the model's effectiveness is further elucidated by the derivation of the moment coefficient ($\boldsymbol{C_M}$) [30], achievable through Eq. (4.4).

$$C_M = R \cdot \tau \tag{4.4}$$

τ indicates the turbine's torque [N.m]. These four parameters serve as benchmarks for evaluating the performance of the model.

4.4 RESULT AND DISCUSSION

4.4.1 Model's Original Performance

The original performance characteristics of the hybrid wind turbine model are effectively illustrated through detailed graphical representations. These graphs, as delineated in Fig. 4.7, showcase the variation of both the moment coefficient and the power coefficient under different operational conditions. By analyzing these graphical depictions, one can gain a comprehensive understanding of the model's efficiency and performance dynamics across a range of scenarios.

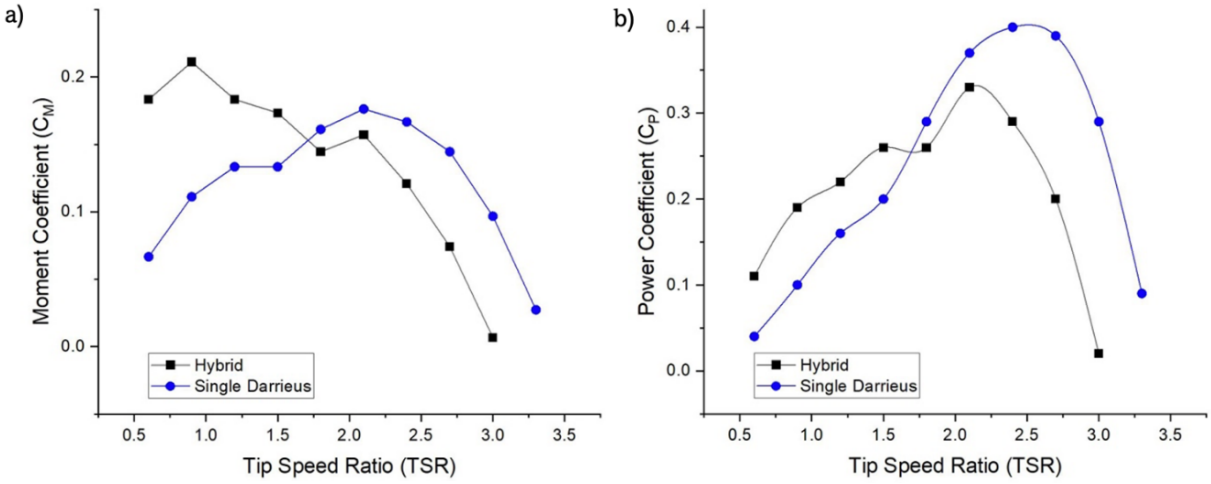

Fig. 4.7 Original Moment (a) and Power Coefficients (b) of the Model

The graphs are constructed based on calculations using Eqs. (4.1) and (4.4). In Fig. 4.7 (a), a detailed characteristic of the moment coefficient profiles for both hybrid and single Darrieus models is presented. Notably, the hybrid configuration demonstrates a substantial initial moment coefficient advantage over its single Darrieus counterpart, registering a remarkable 150% increase. This disparity in performance indicates the distinct aerodynamic characteristics inherent in hybrid turbine design.

Specifically, the hybrid model having a rotor radius ratio of 0.5 exhibits a notable augmentation in the initial moment coefficient. Its enhancement could be ascribed to the Savonius component's dominating effect in the hybrid arrangement. Conversely, a reduction in

the rotor radius ratio leads to a commensurate decrease in the initial moment's coefficient. This observation is in line with prior simulation findings [20], which indicates a rapid decline in moment coefficient for hybrid models with varying rotor radius ratios post-TSR surpassing 1. Notably, the single Darrieus model continues to display a rise in moment coefficient even beyond a TSR of 2, highlighting the robustness and versatility of the single Darrieus setup under varied operational conditions.

Eq. (4.4) shows how the moment coefficient and power coefficient of a turbine are closely connected. Through empirical observation in Fig. 4.7 (b), a discernible distinction emerges between the performance of single Darrieus and hybrid models. Notably, the single Darrieus model reaches a significantly higher maximum power coefficient, exceeding that of the hybrid model by 21%. This difference can be seen in the highest power coefficients that the single Darrieus configuration and the hybrid model attain, with the former reaching a maximum of 0.4 at TSR 2.4 and the latter peaking at 0.33 at TSR 2.1. The lift-based operation of the Darrieus configuration makes it particularly effective at harnessing wind energy at higher velocities. This allows the single Darrieus model to reach its maximum power coefficient at a relatively higher TSR, as observed in Fig. 4.7 (b). In contrast, the hybrid model, which combines elements of both Savonius and Darrieus designs, may exhibit a different performance profile due to the interaction between these distinct aerodynamic principles. However, compared to the computational fluid dynamics (CFD) research conducted by [26], the NREL S809 should still be able to achieve a higher power coefficient, reaching 0.5 at a wind speed of 10 m/s.

The operational dynamics of the Darrieus turbine, predicated on lift force principles, render it particularly effective at higher wind speeds. In ideal circumstances, a single Darrieus turbine would typically reach its maximum power coefficient within the TSR range of 3 – 4 [22]. However, the specific single Darrieus model utilized in this study, characterized by a solidity of 0.75, deviates from this ideal scenario [1]. The relatively high solidity introduces weight considerations that impact the turbine's performance, precluding it from attaining its maximum power coefficient within the typical TSR range of 3 – 4.

4.4.2 Rotor Switching

By combining the best features of hybrid and single Darrieus turbine designs, the rotor switching mechanism is a novel way to produce a hybridized model that optimizes the power generation and aerodynamic efficiency of vertical axis wind turbine. This method involves

seamlessly blending the robust initial torque provided by the hybrid model with the high-speed operational efficiency of the single Darrieus configuration. The resultant model is distinguished by its high initial moment coefficient, which enhances startup capabilities, and its superior maximum power coefficient, which optimizes overall energy production at higher wind speeds.

A crucial component of this design approach is figuring out the exact time to switch the rotor. It is based on a meticulous analysis of the power coefficient curves from extensive empirical data. Fig. 4.7 represents the energy efficiency of the hybrid and single Darrieus models across a range of operating conditions. The intersection of those curves indicates the most effective transition point where the combined benefits of both models are optimized, allowing for enhanced performance and efficiency.

The experimental results, illustrated in Fig. 4.7 (b), are essential to our analysis. They provide a visual representation of the performance thresholds where the benefits of switching from the hybrid to the single Darrieus model are maximized. A technique for determining the rotor switching mechanism has been researched by [24]. A. Hosseini and N. Goudarzi proposed the idea of switching rotors based on the moment value of the turbine. However, this approach is considered less straightforward in practice. Therefore, using the tip speed ratio as the parameter for rotor switching offers a simpler and more innovative solution.

The data in Fig. 4.7 indicates that the optimal rotor switching occurs at a TSR of 1.7. This TSR is identified as the point where the turbine achieves a balance between low-speed torque and high-speed power output, enabling it to operate efficiently across a broader spectrum of wind conditions. However, to simplify the process of determining the switching conditions, using rotational speed is considered easier compared to tip speed ratio. Once it is understood that rotor switching needs to be performed at a TSR of 1.7 for this Smart Hybrid model, it can be converted into rotational speed based on wind speed conditions as illustrated by the graph in Fig. 4.8. The graph in Fig. 4.8 typically illustrates how the rotational speed varies with wind speed to maintain the switching process, providing a visual representation of the turbine's operational strategy to maximize energy extraction under different environmental conditions.

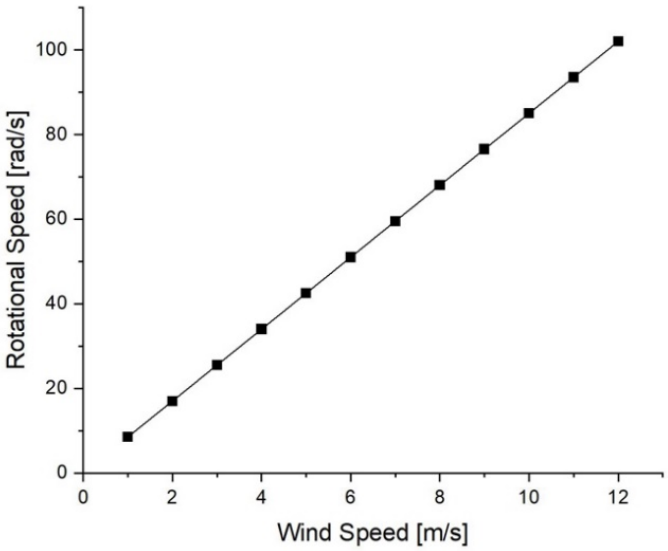

Fig. 4.8 Correlation between Wind Speed and Rotational Speed of the Smart Hybrid at a TSR of 1.7

4.4.3 Expected Performance

Based on the previously described switching rotor theory, it is anticipated that the rotor switching theory will yield superior results, as illustrated in Fig. 4.9.

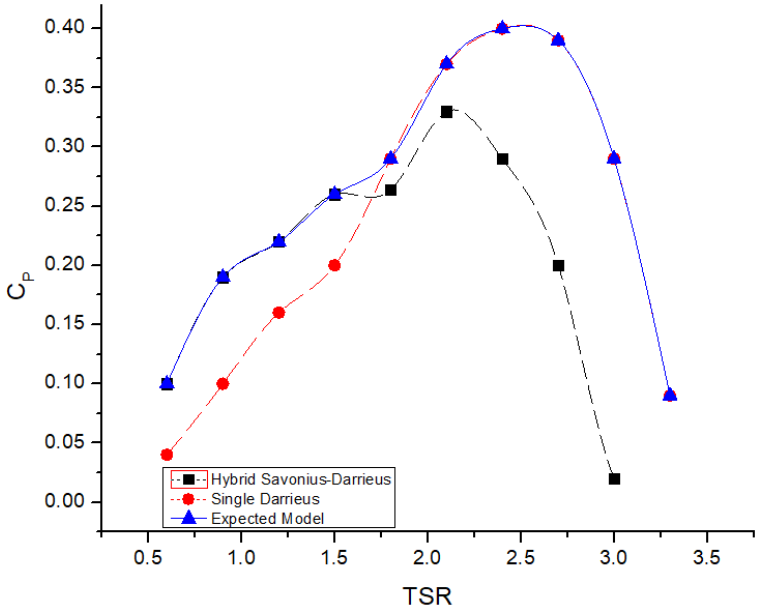

Fig. 4.9 Expected Power Coefficient as a Result of Switching Rotor Mechanism

Transitioning the turbine rotation mode from hybrid to single Darrieus at TSR 1.7 prevents the typical decrease in power coefficient that occurs with the hybrid model. By switching to the single Darrieus mode at this specific TSR, the turbine can maintain or even improve its power coefficient, ensuring more efficient power generation. At the initial TSR, the hybrid mode offers a substantial advantage of 150% over the single Darrieus, providing superior performance and efficiency in capturing wind energy. This initial advantage ensures a strong start in power generation, particularly in lower wind speed conditions. Furthermore, by transitioning to the single Darrieus mode, the turbine can achieve a 21% improvement in maximum power coefficient compared to the hybrid configuration.

This switching mechanism capitalizes on the strengths of the single Darrieus configuration, which may be better suited for higher TSR values. As a result, the turbine can mitigate the decline in power coefficient associated with the hybrid mode and sustain optimal performance across a wider range of wind speeds. Implementing this operational strategy allows for dynamic adaptation to varying wind conditions, ultimately enhancing the overall efficiency and effectiveness of the turbine system. Additionally, by avoiding the power coefficient decrease typically observed in the hybrid mode, this transition ensures consistent and reliable power generation, contributing to the long-term viability and performance of the turbine.

4.4.4 Performance of Smart Hybrid

After implementing the rotor switching, the performance of the Smart Hybrid model can be demonstrated by the following Fig. 4.10.

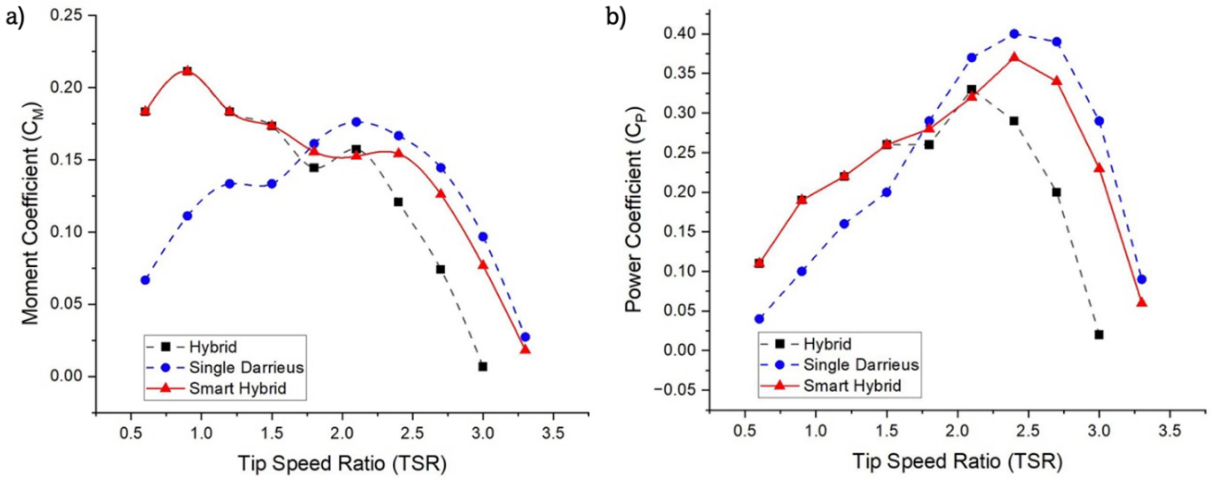

Fig. 4.10 Moment (a) and Power (b) Coefficients of the Smart Hybrid Compared to Two Other Models

Fig. 4.10 (a) displays a comparison of the moment coefficient among three models: hybrid, single Darrieus, and Smart Hybrid. Prior to reaching this pivotal TSR, the Smart Hybrid model mirrors precisely the moment coefficient values of the hybrid model. This implies that the Smart Hybrid model initially presents a compelling advantage, boosting a moment coefficient that surpasses that of the single Darrieus model by 175%. Similarly, compared to the CFD research on improving hybrid VAWTs using double Darrieus conducted by [2], the proposed improvement of the smart hybrid Savonius-Darrieus in this study has a superior initial moment up to a TSR of 2.

However, as the turbine transitions to TSRs immediately following the detachment of the Savonius component from the primary rotor, a discernible impact on the operational dynamics emerges. At this critical point, the power coefficient value of the Smart Hybrid model deviates slightly from the expected trajectory of the single Darrieus model. This shows similar characteristics to those observed in previous simulation studies [20]. This deviation results in a marginal reduction of 8.11% in the maximum power coefficient generated by the Smart Hybrid model compared to the single Darrieus configuration. This phenomenon finds its roots in the independent rotation of the Savonius component positioned amidst the Darrieus blades. This can be elucidated through CFD studies, as demonstrated by the airflow contours in Fig. 4.11. The Savonius component's independent rotational dynamics introduce subtle aerodynamic perturbations within the airflow region proximal to the Darrieus blades, causing minor airflow obstructions.

The presence of the Savonius rotor within the Darrieus turbine configuration induces a flow disturbance that affects the downstream Darrieus blades. This disturbance is visually depicted by the intense blue shading observed in the velocity contours of Fig. 4.11 (a), indicating the formation of a wake region behind the Savonius rotor. Within this wake region, the airflow velocity is significantly reduced, resulting in decreased dynamic pressure and weaker aerodynamic forces acting on the Darrieus blades positioned downstream. Consequently, the Darrieus blades situated directly behind the Savonius rotor experience a diminished pressure differential between their upper and lower surfaces, leading to a reduction in lift force generation. This reduced aerodynamic lift has a negative impact on the turbine's overall reliability since it lessens the torque applied to the rotor shaft, which in turn reduces the turbine

system's power generation. However, acording to research conducted by [5], this weakness can be avoided by positioning the Savonius and Darrieus turbines in a parallel, top-and-bottom arrangement, thereby mitigating the wake effect caused by the internal rotor.

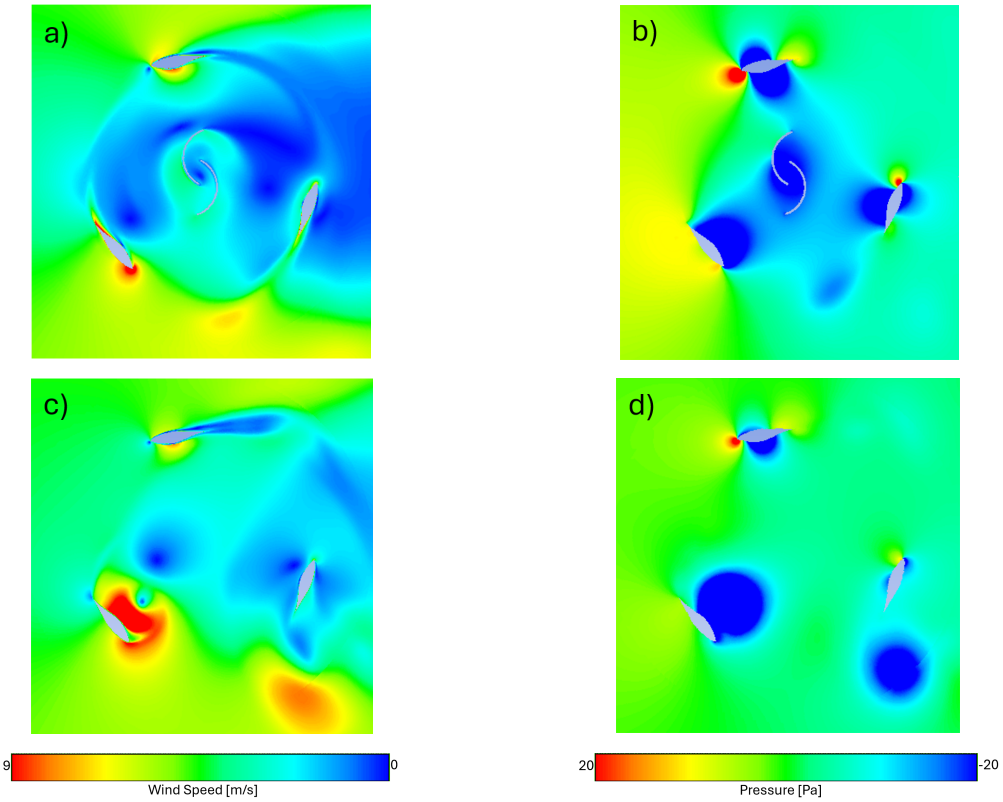

Fig. 4.11 Velocity (a) and Pressure (b) Contours of Hybrid Model vs. Velocity (c) and Pressure (d) Contours of Single Darrieus Model

Despite this deviation, the Smart Hybrid model still maintains a notable maximum power coefficient superiority of 12.12% when juxtaposed against the conventional hybrid model. This improvement reflects the enhanced aerodynamic efficiency achieved through its innovative design, which optimizes the interaction between the Savonius and Darrieus components. The Smart Hybrid model effectively harnesses both drag- and lift-based mechanisms, allowing for higher energy capture under similar wind conditions.

Furthermore, the operational versatility of the Smart Hybrid model is highlighted by its extended range of operation in terms of tip speed ratio (TSR), surpassing a threshold of 3.3. In comparison, the traditional hybrid model exhibits a more limited TSR range, capped at a maximum value of 3.0, which restricts its ability to efficiently operate under fluctuating wind

conditions. This expanded TSR capability of the Smart Hybrid enables the turbine to maintain optimal performance across a broader spectrum of wind speeds, improving both reliability and consistency in power generation.

4.5 CONCLUSION

This study introduced a Smart Hybrid vertical axis wind turbine (VAWT) with a rotor-switching mechanism to optimize performance at various tip speed ratios (TSR). Experimental results confirmed that the hybrid model improves self-starting but suffers efficiency losses at high TSR due to Savonius drag. The rotor-switching mechanism successfully transitions operation to a single Darrieus mode at TSR 1.7, enhancing efficiency by 21% compared to the hybrid model alone.

The Smart Hybrid model maintains a high initial moment coefficient, improving startup, and extends the TSR range beyond 3.3, outperforming conventional hybrid designs. Despite a minor efficiency drop due to aerodynamic disturbances, the model achieves a 12% higher maximum power coefficient than the hybrid model. This innovative switching approach improves adaptability and energy output, making Smart Hybrid VAWTs more viable for real-world applications.

REFERENCES

[1] N. Aboufazeli, P. H. Tari, R. Gavagsaz-ghoachani, and M. Zandi, “Effect of solidity on the performance of micro-scale darrieus wind turbines: An Experimental Study,” in *2019 Iranian Conference on Renewable Energy & Distributed Generation (ICREDG)*, Jun. 2019, pp. 1–5. doi: 10.1109/ICREDG47187.2019.190154.

[2] M. Ahmad, A. Shahzad, F. Akram, F. Ahmad, and S. I. A. Shah, “Design optimization of Double-Darrieus hybrid vertical axis wind turbine,” *Ocean Engineering*, vol. 254, p. 111171, Jun. 2022, doi: 10.1016/j.oceaneng.2022.111171.

[3] M. Ahmad, A. Shahzad, and M. N. M. Qadri, “An overview of aerodynamic performance analysis of vertical axis wind turbines,” *Energy & Environment*, vol. 34, no. 7, pp. 2815–2857, Nov. 2023, doi: 10.1177/0958305X221121281.

[4] M. Ahmad and M. H. Zafar, “Enhancing vertical axis wind turbine efficiency through leading edge tubercles: A multifaceted analysis,” *Ocean Engineering*, vol. 288, p. 116026, Nov. 2023, doi: 10.1016/j.oceaneng.2023.116026.

[5] N. M. Ali, A. H. A. K, and S. Aljabair, “THE EFFECT OF DARRIEUS AND SAVONIUS WIND TURBINES POSITION ON THE PERFORMANCE OF THE HYBRID WIND TURBINE AT LOW WIND SPEED,” May 26, 2020, *Engineering Archive*. doi: 10.31224/osf.io/grbmv.

[6] M. A. Al-Rawajfeh and M. R. Gomaa, “Comparison between horizontal and vertical axis wind turbine,” *International Journal of Applied Power Engineering (IJAPE)*, vol. 12, no. 1, Art. no. 1, Mar. 2023, doi: 10.11591/ijape.v12.i1.pp13-23.

[7] L. Amjith and B. Bavanish, “A review on biomass and wind as renewable energy for sustainable environment,” *Chemosphere*, vol. 293, p. 133579, Apr. 2022, doi: 10.1016/j.chemosphere.2022.133579.

[8] T.-Z. Ang, M. Salem, M. Kamarol, H. S. Das, M. A. Nazari, and N. Prabaharan, “A comprehensive study of renewable energy sources: Classifications, challenges and suggestions,” *Energy Strategy Reviews*, vol. 43, p. 100939, Sep. 2022, doi: 10.1016/j.esr.2022.100939.

[9] O. C. Castillo, V. R. Andrade, J. J. R. Rivas, and R. O. González, “Comparison of Power Coefficients in Wind Turbines Considering the Tip Speed Ratio and Blade Pitch Angle,” *Energies*, vol. 16, no. 6, Art. no. 6, Jan. 2023, doi: 10.3390/en16062774.

[10] D. Cazzaro, G. Bedon, and D. Pisinger, “Vertical Axis Wind Turbine Layout Optimization,” *Energies*, vol. 16, no. 6, Art. no. 6, Jan. 2023, doi: 10.3390/en16062697.

[11] J. Cullen, “Measuring the Environmental Benefits of Wind-Generated Electricity,” *American Economic Journal: Economic Policy*, vol. 5, no. 4, pp. 107–133, 2013.

[12] A. Dewan, A. Gautam, and R. Goyal, “Savonius wind turbines: A review of recent advances in design and performance enhancements,” *Materials Today: Proceedings*, vol. 47, pp. 2976–2983, Jan. 2021, doi: 10.1016/j.matpr.2021.05.205.

[13] A. M. EI Kenawy, T. Al-Awadhi, M. Abdullah, R. Jawarneh, and A. Abulibdeh, “A Preliminary Assessment of Global CO2: Spatial Patterns, Temporal Trends, and Policy Implications,” *Global Challenges*, vol. 7, no. 12, p. 2300184, 2023, doi: 10.1002/gch2.202300184.

[14] A. M. A. El-Zafry, O. E. A. El-Hameed, D. M. S. Hassan, and D. M. M. Shaheen, “A Review On The Types Of Vertical Axis Wind Turbines And The Methods Of Their Performance Study,” vol. 6, no. 9, 2019.

[15] A. Pallotta, D. Pietrogiacomi, and G. P. Romano, “HYBRI – A combined Savonius-Darrieus wind turbine: Performances and flow fields,” *Energy*, vol. 191, p. 116433, Jan. 2020, doi: 10.1016/j.energy.2019.116433.

[16] A. Fazylova, B. Tultayev, T. Iliev, I. Stoyanov, and I. Beloev, “Development of a Control Unit for the Angle of Attack of a Vertically Axial Wind Turbine,” *Energies*, vol. 16, no. 13, Art. no. 13, Jan. 2023, doi: 10.3390/en16135202.

[17] D. Puspitasari and K. Sahim, “Effect of Savonius blade height on the performance of a hybrid Darrieus-Savonius wind turbine,” *Journal of Mechanical Engineering and Sciences*, vol. 13, no. 4, Art. no. 4, Dec. 2019, doi: 10.15282/jmes.13.4.2019.09.0465.

[18] P. Ghiasi, G. Najafi, B. Ghobadian, and A. Jafari, “Analytical and Numerical Solution for H-type Darrieus Wind Turbine Performance at the Tip Speed Ratio of Below One,” *International Journal of Renewable Energy Development*, vol. 10, no. 2, pp. 269–281, May 2021, doi: 10.14710/ijred.2021.33169.

[19] E. N. Irawan, K. Shibuya, K.-I. Yamashita, and G. Fujita, “Enhancing Vertical Axis Wind Turbine Performance Investigation at Low Wind Speed Using Electrical Approach,” in *2024 8th International Conference on Green Energy and Applications (ICGEA)*, Mar. 2024, pp. 1–5. doi: 10.1109/ICGEA60749.2024.10561142.

[20] E. N. Irawan, S. Sitompul, K.-I. Yamashita, and G. Fujita, “The Effect of Rotor Radius Ratio on The Performance of Hybrid Vertical Axis Wind Turbine Savonius-Darrieus NREL S809,” *Journal of Energy and Power Technology*, vol. 5, no. 1, Art. no. 1, Jan. 2023, doi: 10.21926/jept.2301001.

[21] H. Eftekhari, A. S. M. Al-Obaidi, and S. Eftekhari, “Aerodynamic Performance of Vertical and Horizontal Axis Wind Turbines: A Comparison Review,” *Indonesian Journal of Science and Technology*, vol. 7, no. 1, Art. no. 1, 2022, doi: 10.17509/ijost.v7i1.43161.

[22] E. A. D. Kumara and N. K. Hettiarachchi, “Review Paper: Overview of the Vertical Axis Wind Turbines,” vol. 4, no. 8, 2017.

[23] M. Jamil and M. Layeghi, “Experimental Study of a Combined Three Bucket H-Rotor with Savonius Wind Turbine,” 2013. Accessed: Feb. 16, 2025. [Online]. Available: https://www.semanticscholar.org/paper/Experimental-Study-of-a-Combined-Three-Bucket-with-Jamil-Layeghi/c7a7ca23b53112f77b31c90d9443b757f140a9a2

[24] A. Hosseini and N. Goudarzi, “CFD and Control Analysis of a Smart Hybrid Vertical Axis Wind Turbine,” presented at the ASME 2018 Power Conference collocated with the ASME 2018 12th International Conference on Energy Sustainability and the ASME 2018 Nuclear Forum, American Society of Mechanical Engineers Digital Collection, Oct. 2018. doi: 10.1115/POWER2018-7488.

[25] T. Rus, L. F. Rus, D. A. Ilutiu-Varvara, R. Mare, A. Abrudan, and F. Domnita, “Experimental Investigation on the Influence of Overlap Ratio on Savonius Turbines Performance,” *International Journal of Renewable Energy Research (IJRER)*, vol. 8, no. 3, Art. no. 3, Sep. 2018.

[26] F. N. Modi and N. R. Gilke, “Computational Analysis of Various Airfoil Profile on the Performance of H-Darrieus Wind Turbine,” in *2018 ieee international conference on system, computation, automation and networking (icscan)*, Jul. 2018, pp. 1–5. doi: 10.1109/ICSCAN.2018.8541245.

[27] C. Jung and D. Schindler, “The role of air density in wind energy assessment – A case study from Germany,” *Energy*, vol. 171, pp. 385–392, Mar. 2019, doi: 10.1016/j.energy.2019.01.041.

[28] P. Preecha and J. Dejvises, “The power losses calculation technique of electrical machines using the heat transfer theory,” in *2007 International Power Engineering Conference (IPEC 2007)*, Dec. 2007, pp. 297–301. Accessed: Jan. 27, 2025. [Online]. Available: https://ieeexplore.ieee.org/document/4510045

[29] W. L. Lorimer and D. K. Lieu, “Method for measuring and characterizing core loss in a motor,” *IEEE Transactions on Magnetics*, vol. 35, no. 4, pp. 2146–2151, Jul. 1999, doi: 10.1109/20.774185.

[30] Y. Kamada, T. Maeda, K. Naito, Y. Ouchi, and M. Kozawa, “Measurement of Unsteady Aerodynamics Load on the Blade of Field Horizontal Axis Wind Turbine,” *Journal of Fluid Science and Technology*, vol. 3, no. 3, pp. 335–343, 2008, doi: 10.1299/jfst.3.335.

CHAPTER 5
ESTIMATING WIND ENERGY POTENTIAL: ADVANCED SMART HYBRID VAWT ANALYSIS IN BANJARMASIN, INDONESIA

5.1 CHAPTER INTRODUCTION

Renewable energy has become the primary choice for modernizing and enhancing power systems [1]. Among these sources, solar and wind energy account for 90% of the total renewable energy supply [2]. Notably, Indonesia holds substantial potential for renewable energy, particularly in wind power, which provides a vast energy resource [3]. As outlined in the strategic plan by the Directorate General of New, Renewable, and Conservation Energy, Ministry of Energy and Mineral Resources (2020 – 2024), Indonesia's average wind speed annually varies between 3 and 6 m/s [4].

Wind energy is generated using wind turbines, which convert the wind's kinetic energy into electrical power [5]. Horizontal axis wind turbines (HAWT) are typically more efficient than vertical axis wind turbines (VAWT) due to their ability to capture energy throughout the full rotation of their blades under consistent wind conditions [6]. Unlike HAWTs, which need to continuously align with the wind direction for maximum efficiency, VAWTs can operate omnidirectionally, capturing wind from any direction [7]. The Savonius turbine represents the initial design of VAWTs and functions by utilizing drag forces similar to a water wheel. Conversely, the Darrieus turbine, a different type of VAWT, employs aerodynamic blades to generate lift, enabling the turbine to rotate.

According to A. Pallotta et al. [8], combining the performance of Savonius and Darrieus turbines offers significant advantages. This innovative design, a hybrid Savonius-Darrieus rotor, is specifically developed to optimize performance in low to moderate wind conditions. The system exhibits strong operational efficiency, achieving a power coefficient of approximately 0.2 or slightly less, over a wide range of operating parameters. In contrast to the individual turbines, which have narrower operating ranges (0.5 – 1 for Savonius and 1.7 – 4 for Darrieus), the hybrid turbine operates effectively across a broader tip speed ratio range of 0.5 to 4.

S. Chegini et al. [9] observed that integrating Savonius and Darriues turbines significantly improves the hybrid turbine's self-starting capability, leading to a 26.91% increase in the power coefficient (C_P) at the lowest tip speed ratio (TSR) of 1.45. However, as TSR increases, the

hybrid turbine's performance declines due to the limited aerodynamic efficiency of the Savonius turbine at higher speeds. This issue is addressed using front and side deflectors, which enhance the turbine's efficiency at an optimal TSR of 2.6 by 30% and 26%, respectively. These deflectors improve wind energy density in both the upwind and leeward areas of the turbine.

In our earlier research [10], we explored the potential of combining the hybrid Savonius-Darrieus configuration with a Darrieus mode within a single turbine unit. The findings demonstrated that switching the turbine's rotational mode at a TSR of 1.7 yields optimal results. This configuration, termed the smart hybrid vertical axis wind turbine, facilitates efficient operation across a wide range of wind speeds, from low to high velocities. It is particularly suitable for regions with substantial wind speed fluctuations, such as Banjarmasin, Indonesia. Therefore, we propose conducting a study to assess the wind power potential of the smart hybrid turbine model in this region.

5.1 WIND SPEED CONDITION AT BANJARMASIN

Evaluating wind speed is essential for accurately estimating the potential for wind power generation at a specific location [11]. Wind speed at a specific height above ground level is determined using Eq. (5.1).

$$u = u_{ref}\left(\left(\frac{h}{h_{ref}}\right)^{\gamma}\right) \tag{5.1}$$

In this equation, u and u_{reff} represent the mean wind speeds at heights h and h_{reff}, respectively. The estimation of wind speed u at a higher elevation h is commonly performed in the wind energy industry using the assumption of a standard wind profile or the power law relationship. This approach utilizes surface or tower wind speed measurements u_{reff} at a reference height h_{reff}, typically 10 meters. The shear exponent γ is generally taken as 0.2 [12].

Fig. 5.1 illustrates the wind speeds recorded in Banjarmasin at one-minute intervals during January 2024 at 10 m height. Fig. 5.1 is the wind speed data which is taken at the latitude of 114.767 and the longitude of -3.439. The region exhibits substantial variability in wind speeds, which is a key factor in assessing the efficiency and performance of wind turbines. The maximum wind speed observed was 14.7 m/s, highlighting the occurrence of occasional strong wind events. Meanwhile, the average wind speed was 2.9 m/s, representing the typical wind

conditions in the area. These variations are crucial for evaluating the potential energy output and addressing operational challenges associated with wind turbines.

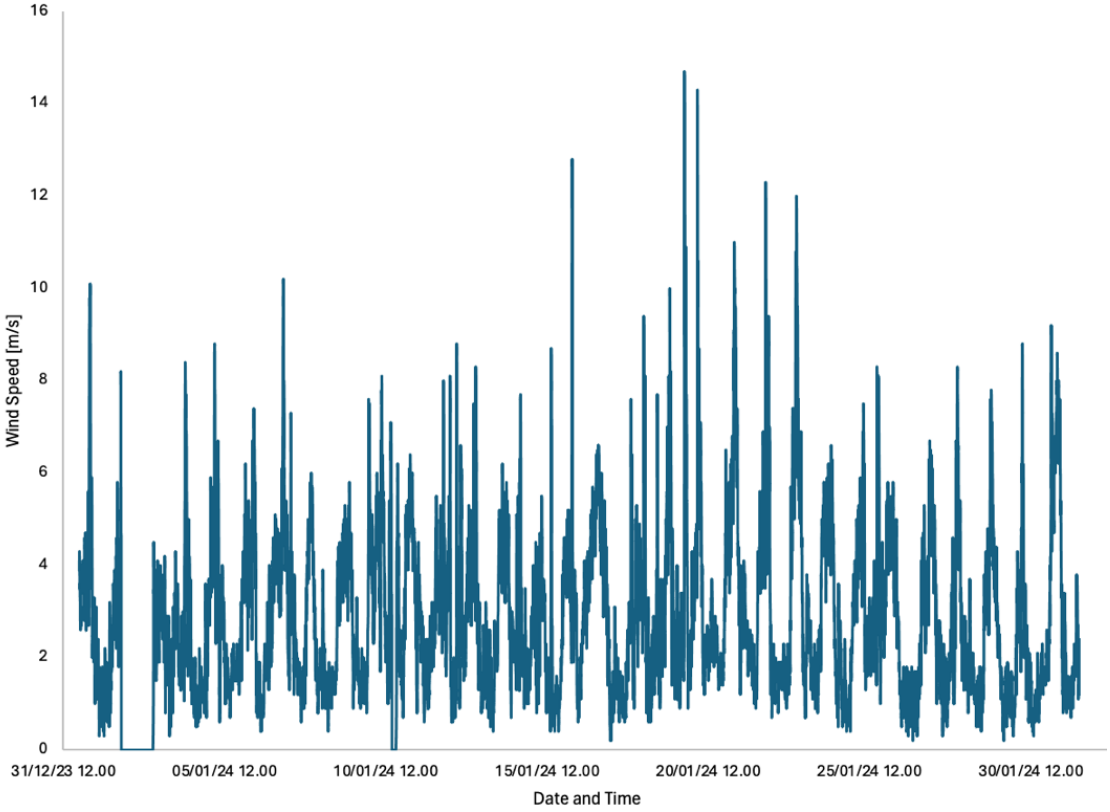

Fig. 5.1 Wind speed data at Banjarmasin, Indonesia (January 2024) [4]

5.2 INTERPOLATION

Interpolation is a crucial tool in environmental modeling, used for hindcasting, nowcasting, and forecasting [13]. This process utilizes datasets (such as remote sensing, sampling, or experimental data) to generate a function that can replicate or simulate data trends with minimal deviation [14]. While interpolation estimates values between known data points, extrapolation predicts values beyond the given range [15]. This approach enables users to make informed estimations of data within the existing dataset.

The development of an interpolation function from a dataset is primarily achieved using polynomials [13]. The polynomial approach is widely adopted in interpolation due to its ease of evaluation, differentiation, and integration [16]. Moreover, since interpolation focuses on fitting

a smooth curve through a given set of points, a mathematical representation of this smooth curve can only be effectively achieved using polynomials [17].

There are various types of interpolation, including piecewise constant interpolation, linear interpolation, polynomial interpolation, and spline interpolation [18]. The choice of a specific method largely depends on factors such as execution speed, accuracy, cost, the number of required data points, and user-friendliness. For instance, linear interpolation is efficient and easy to use with a small dataset; however, its main drawbacks include limited precision and the inability to differentiate data points [19]. In linear interpolation, the estimated value is assumed to lie on the straight line connecting the two closest known points. Suppose the x values are arranged in increasing order, meaning $x_i < x_{i+1}$, and there exists a point x such that $x_i < x < x_{i+1}$. The interpolation at x is then expressed as Eq. (5.2).

$$f(x) = f(x_i) + \frac{f(x_{i+1}) - f(x_i)}{x_{i+1} - x_i}(x - x_i) \tag{5.2}$$

This equation represents a linear function passing through the points $(x_i, f(x_i))$ and $(x_{i+1}, f(x_{i+1}))$, allowing for the estimation of $f(x)$ at any intermediate x within the given interval [20].

When dealing with gridded or scattered data, bicubic interpolation is commonly applied in two dimensions. Bicubic interpolation can be performed using Lagrange polynomials, cubic splines, or cubic convolution methods. The bicubic interpolation model can be illustrated using the functional value f along with its partial derivatives f_x, f_y, and f_{xy}, which are known at the four corners of the unit square: (0,0), (1,0), (0,1), and (1,1). Based on this, the interpolation formula can be expressed as Eq. (5.3).

$$p(x, y) = \sum_{i=0}^{3} \sum_{j=0}^{3} a_{ij} x^i y^j \tag{5.3}$$

$p(x, y)$ represents the interpolated function, which provides the estimated value at any point (x, y) within the unit square. a_{ij} are the coefficients that need to be determined based on the known function values and their derivatives at the four corners of the interpolation region [21]. Then trilinear interpolation is used in three dimensions. On the other hand, piecewise constant interpolation is often preferred for high-dimensional multivariate interpolation due to its simplicity and fast computation [22].

A major drawback of polynomial interpolation is that the error tends to increase proportionally to the distance between data points raised to the power of n [23]. In many cases,

this results in significant errors, making it essential to verify deviations when extensively applying interpolation in environmental research. Additionally, polynomial interpolation is computationally more demanding than linear interpolation, which is why spline interpolation is often preferred [24]. Spline interpolation utilizes low-degree polynomials within each interval, ensuring that the polynomial segments fit together smoothly [25]. When working with an infinite number of data points, the Whittaker–Shannon interpolation is recommended [26]. Since certain environmental datasets fall within this category, it is crucial for environmental experts to gain hands-on experience with various interpolation methods.

5.3 WIND POWER POTENTIAL

In all previous studies, average wind speeds have been employed to estimate wind power density. However, since wind power is directly related to the cube of wind speed, a more precise approach in calculations involves using the root mean cube of wind speed, which is defined as Eq. (5.4) [27].

$$v_{rmc} = \left(\frac{1}{n}\sum_{i=1}^{n} {v_i}^3\right)^{1/3} \tag{5.4}$$

The formula for wind power (P_w) can be expressed in terms of air density (ρ) [kg/m^3], the swept area of the turbine blades (A) [m^2], and a given set of wind speed data (v_i) [m/s] as Eq. (5.5) [27].

$$P_w = \frac{1}{2}\rho A\left(\frac{1}{n}\sum_{i=1}^{n} {v_i}^3\right)^{1/3} = \frac{1}{2}\rho A {v_{rmc}}^3 \tag{5.5}$$

The power extracted from the wind is influenced by both the available wind energy and the operational characteristics of the wind energy conversion system. The wind power potential of a location is influenced by site-specific characteristics, wind speed, and the specifications of the wind turbine. Betz established a theoretical limit, known as the Betz limit, which states that wind turbines cannot achieve 100% efficiency in converting wind energy into power. According to Eq. (5.6), actual power output (P) of a turbine is directly proportional to the cube of the wind speed [28].

$$P = \frac{1}{2} C_P \rho A v^3 \tag{5.6}$$

In this equation, C_P is a turbine power coefficient, ρ denotes air density, v represents wind speed, and A, the swept area of the turbine rotor, is determined by the diameter of the rotor blades. The

diameter of the rotor affects both the power generation capacity and the optimal spacing between wind turbines in a given area [29]. Then, the daily energy output E can be estimated using Eq. (5.7).

$$E = P_T t \tag{5.7}$$

Where t represents the total operational time of the turbine in a day [hour].

5.4 METHODOLOGY

5.4.1 Turbine model

The proposed turbine model adopts a hybrid Savonius-Darrieus configuration, as depicted in Fig. 5.2.

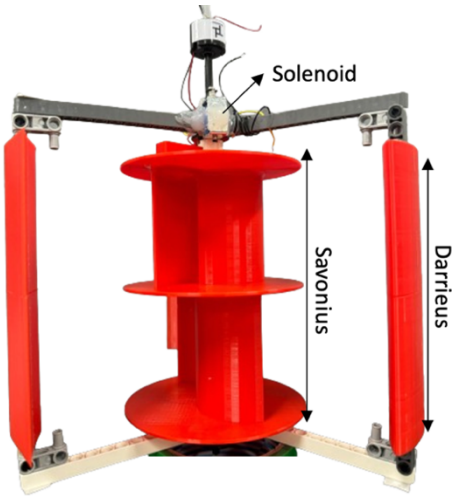

Fig. 5.2 Turbine Model

This innovative design combines the advantages of both Savonius and Darrieus turbines to enhance performance under varying wind conditions. With compact dimensions of 20 cm in width and 14 cm in height, the model is specifically designed for laboratory testing. It features a rotor radius ratio of 0.5, optimizing the balance between the Savonius and Darrieus components to improve initial torque. Furthermore, an overlap ratio of 0.2 is incorporated into the Savonius rotor, enhancing wind energy capture and overall efficiency. However, to estimate the wind power potential in the target area, it is assumed that the dimensions of the model are scaled up by a factor of four compared to the laboratory model. As a result, the dimensions become 120 cm in diameter and 64 cm in height.

A crucial element of this model is the solenoid mechanism, which is specifically designed to control the engagement and disengagement of the Savonius rotor from the Darrieus shaft the primary actuator in the switching rotor process. This feature becomes particularly important when the turbine reaches a high tip speed ratio (TSR), defined as the ratio of the rotor's rotational speed to the wind speed. By enabling selective connection or disconnection of the Savonius rotor, the solenoid mechanism ensures efficient turbine operation across different wind conditions, effectively regulating aerodynamic forces and maximizing energy capture.

5.4.2 Establishing the Ideal Switching Interval

In order to implement this turbine in regions with highly variable wind conditions, the frequent switching of the rotor, previously described as the coupling and decoupling of the Savonius and Darrieus components, can reduce the turbine's effectiveness. Therefore, a filtering mechanism is applied to determine the optimal timing for rotor switching. Based on theory, the turbine is expected to stability after completing at least 5 rotations. According to average wind speed data obtained from BMKG Indonesia, the average wind speed in Banjarmasin is approximately 2.9 m/s. Therefore, based on the experiment, the turbine takes around 15 seconds to complete 5 rotations.

Given that the initial turbine radius is 15 cm, and it completes 5 rotations in 15 seconds, the aim is to determine the required time if the radius is increased to 60 cm. Since angular velocity (ω) is inversely proportional to the radius (r) under constant wind energy input, the rotation period scales linearly with the radius [13]. The relationship can be expressed as:

$$\frac{t_2}{t_1} = \frac{r_2}{r_1} \tag{5.8}$$

Thus, when the turbine radius increases to 60 cm, the time required to complete 5 rotations is 60 seconds.

The method for filtering data is straightforward. Based on the wind speed database obtained, the transformation from Hybrid-Darrieus is identified as "Switch1," while from Darrieus-Hybrid is identified as "Switch2." If the subsequent rpm conditions remain stable for at least 60 seconds, then the switching process is executed. The thresholds used for determining switching are as follows:

- If rpm < 78.5 rpm, then Switch1
- If rpm >= 78.5 rpm rad/s, then Switch2

The switching method's flowchart is shown in Fig. 5.3.

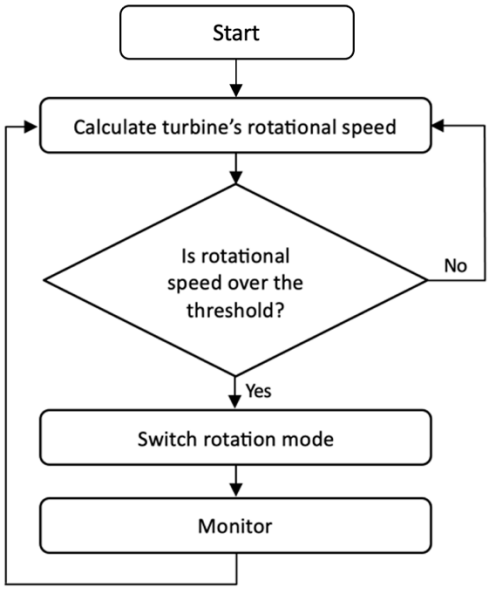

Fig. 5.3 Switching Method

5.5 RESULTS AND DISCUSSION

5.5.1 Switching Interval

The wind speed data obtained from BMKG (Badan Meteorologi, Klimatologi, dan Geofisika) Indonesia is recorded at one-minute intervals. To analyze rotor switching, data at one-second intervals is required. Therefore, interpolation was performed to generate new data, as presented in Fig. 5.4.

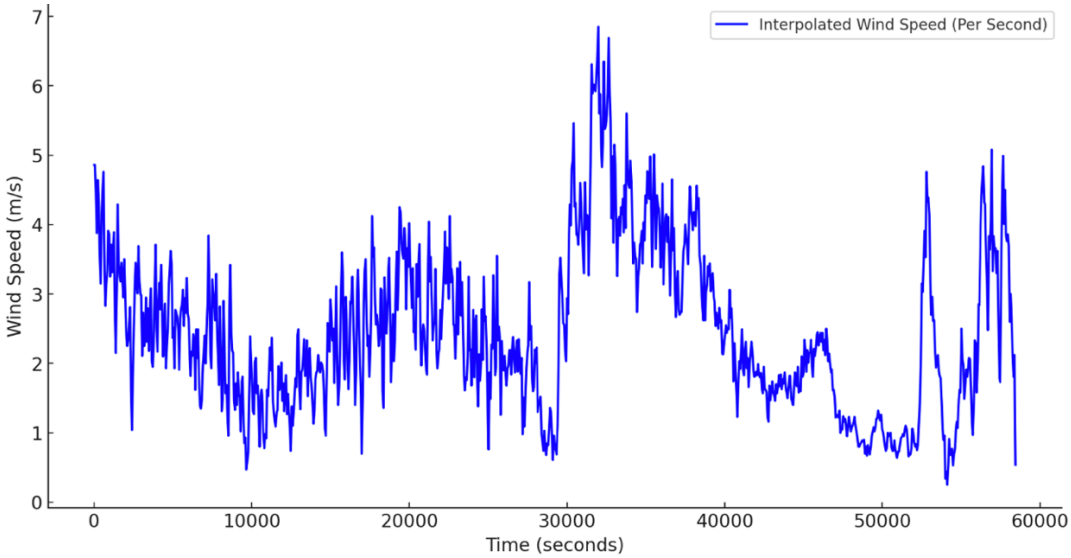

Fig. 5.4 Interpolated Wind Speed

The data in Fig. 5.4 is used to analyze the number of rotors switching that should occur, with the results presented in Fig. 5.5.

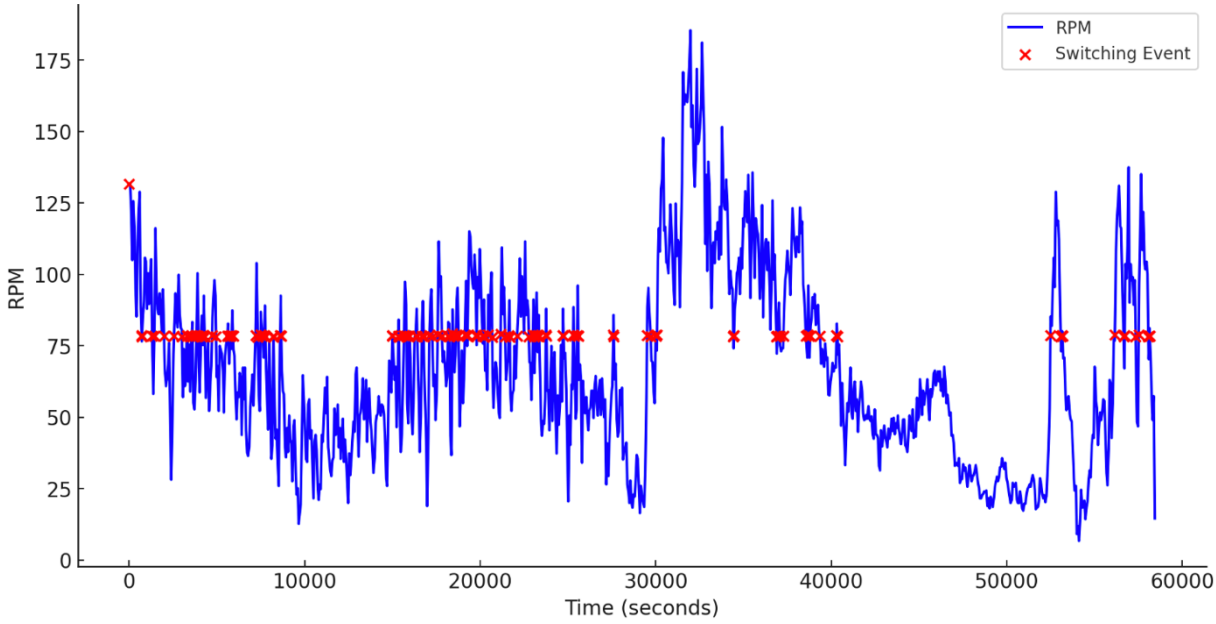

Fig. 5.5 The Number of Original Rotors Switching

The red dots depicted in the figure represent instances of switching, amounting to 120 occurrences within a single day. Such a high frequency of switching is not only inefficient but also adversely impacts the performance of the turbine by increasing mechanical wear and operational instability. The excessive switching is likely due to the turbine's sensitivity to fluctuating wind conditions, which triggers the switching mechanism more frequently than desired. This underscores the need for an optimized switching strategy to enhance turbine performance and longevity.

To address this issue, a hysteresis control and deadband method was implemented to smooth out transient fluctuations and stabilize the switching process. The method approach involves setting thresholds that allow for minor variations in wind speed and turbine rotation without triggering a switch, thereby reducing the frequency of switching events as shown in Fig. 5.6.

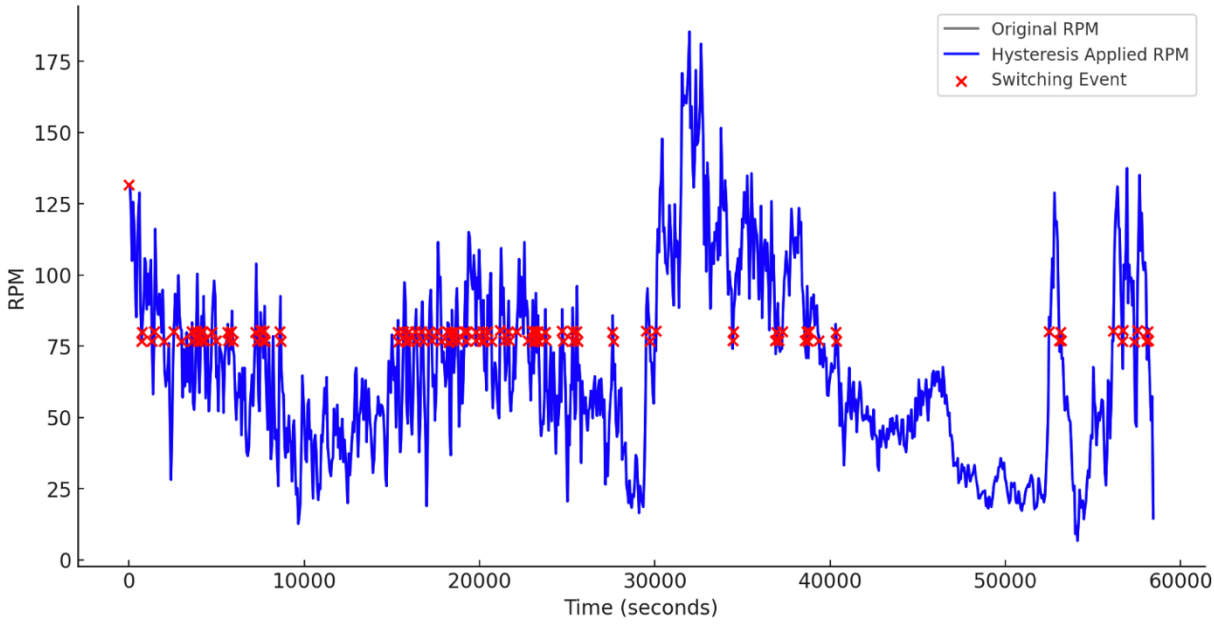

Fig. 5.6 The Number of Rotors Switching After Filtered

By incorporating this filtering method, the number of switching processes significantly decreased, leading to a more stable and efficient operation of the turbine. The number of switching events has now been reduced to only 37 times per day.

The implementation of filtering to reduce switching variability in wind turbines is a critical strategy for enhancing both performance and system longevity. By smoothing transient fluctuations in wind speed, the filter helps minimize unnecessary rotor switching, which in turn improves the turbine's operational stability and reduces mechanical stress. In the initial system (represented by Fig 5.5), 120 switching events per day were observed due to the turbine's sensitivity to fluctuating wind conditions. Frequent switching increases wear on mechanical components, particularly in the gearbox, bearings, and control systems. By applying the filtering method, the number of switching events is dramatically reduced to just 37 per day (as seen in Fig 5.4). This demonstrates a 69% decrease in switching frequency, which significantly reduces mechanical wear, extending the turbine's lifespan.

The refined switching strategy ensures that the turbine operates within its optimal performance range, minimizing wear and tear and maximizing energy output. This adjustment not only improves the overall efficiency of the turbine but also contributes to the reliability and durability of the system, which is crucial for sustainable energy generation.

5.5.2 Wind Energy Potential Estimation in Banjarmasin, Indonesia

To estimate the potential wind energy from this data, an ideal generator efficiency of 90% is assumed. The results are illustrated in Fig. 5.7.

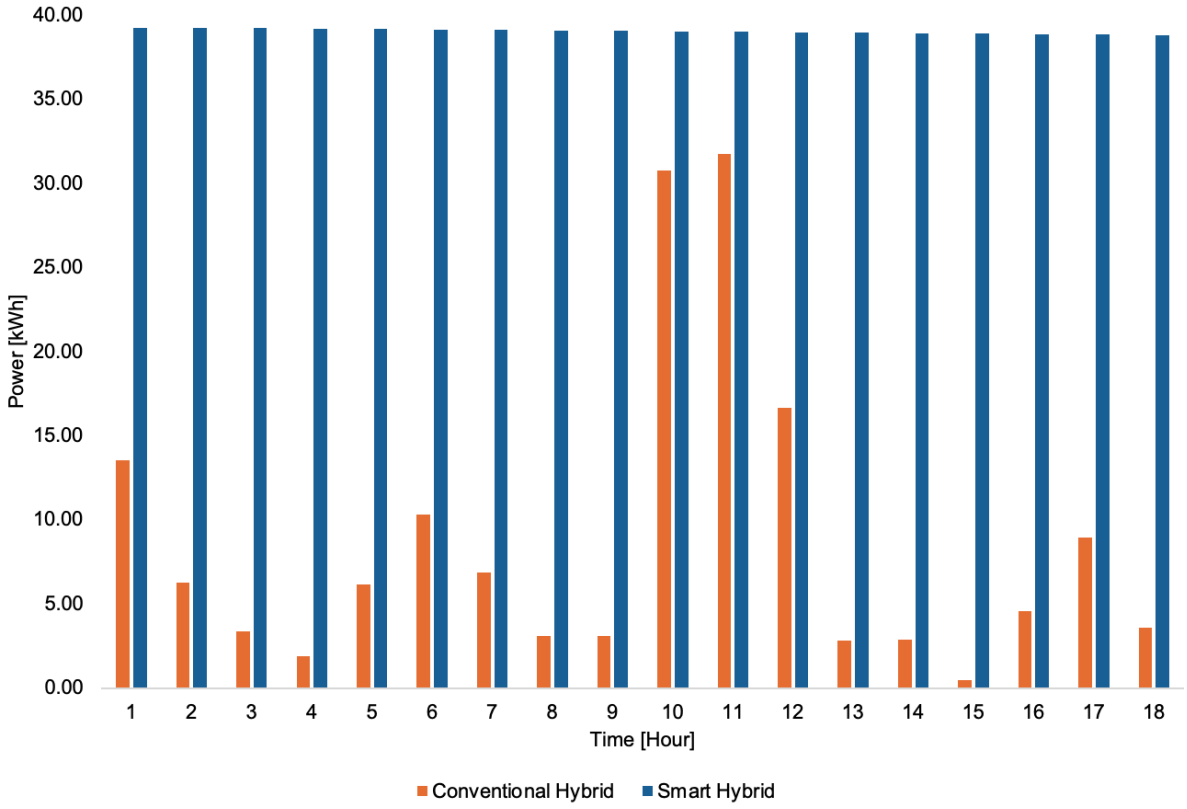

Fig. 5.7 Daily Wind Power Potential Estimation at Banjarmasin, Indonesia (January 2024)

Fig. 57 provides a comparison between the potential wind energy outputs of the smart hybrid turbine and the conventional hybrid turbine. The smart hybrid turbine exhibits a clear advantage, generating more power due to its ability to adapt to varying wind speeds. The Smart Hybrid system consistently achieves the maximum power output (~40 kWh) across all recorded hours, demonstrating its ability to maintain stable and efficient power generation. In contrast, the Conventional Hybrid system exhibits considerable fluctuations, with power output varying significantly over time. One of the key observations from this data is the stability and reliability of the Smart Hybrid system. The consistent power output suggests that it employs optimized control strategies and energy management techniques, ensuring continuous operation without significant downtime. Conversely, the Conventional Hybrid system experiences periods of low

or near-zero power output, indicating possible inefficiencies in energy conversion, resource availability, or system control mechanisms.

The daily average wind energy potential for the smart hybrid and conventional hybrid turbines is calculated to be 157.13 kWh and 703.07 kWh, respectively. This significant difference underscores the superior performance of the smart hybrid turbine in environments with fluctuating wind speeds, such as those observed in Banjarmasin. The smart hybrid turbine's ability to switch modes and optimize performance according to the wind conditions allows it to produce approximately 347.46% more power than the conventional hybrid turbine.

This analysis highlights the importance of adaptive turbine technologies in maximizing energy capture from wind resources. The smart hybrid turbine's design, which integrates both drag and lift principles and features a sophisticated rotor switching mechanism, demonstrates its potential to enhance renewable energy generation. By adjusting to wind speed variations, it ensures more consistent and higher energy output, contributing to the overall efficiency and viability of wind power as a sustainable energy source. Future research and development should continue to focus on optimizing such adaptive systems to further improve their performance and reliability under diverse environmental conditions.

5.6 CONCLUSION

In the transition to renewable energy, Indonesia's significant wind energy potential offers promising opportunities, particularly with the implementation of hybrid Savonius-Darrieus wind turbines. This study highlights the advantages of combining these turbine types, leveraging their complementary strengths to optimize performance across varying wind conditions. By incorporating an innovative solenoid mechanism for efficient mode switching and a filtering method to stabilize operation, the smart hybrid turbine significantly outperforms the conventional hybrid turbine, generating approximately 347.46% more power. This adaptability ensures efficient energy capture even in regions with fluctuating wind speeds, like Banjarmasin. Future research should focus on refining these adaptive systems to enhance their reliability and efficiency, further supporting the broader adoption of wind power as a sustainable energy source.

REFERENCES

[1] L. S. Paraschiv and S. Paraschiv, “Contribution of renewable energy (hydro, wind, solar and biomass) to decarbonization and transformation of the electricity generation sector for sustainable development,” *Energy Reports*, vol. 9, pp. 535–544, Sep. 2023, doi: 10.1016/j.egyr.2023.07.024.

[2] A. S. Darwish and R. Al-Dabbagh, “Wind energy state of the art: present and future technology advancements,” *Renew. Energy Environ. Sustain.*, vol. 5, p. 7, 2020, doi: 10.1051/rees/2020003.

[3] A. Y. I. Megawati *et al.*, “An overview of wind energy to optimize initial potential in Java,” *E3S Web Conf.*, vol. 475, p. 03001, 2024, doi: 10.1051/e3sconf/202447503001.

[4] H. Ardiansyah *et al.*, *Indonesia Post-Pandemic Outlook: Strategy towards Net-Zero Emissions by 2060 from the Renewables and Carbon-Neutral Energy Perspectives*. Penerbit BRIN, 2022. doi: 10.55981/brin.562.

[5] M. O. L. Hansen, “Chapter 9 - Aerodynamics and Design of Horizontal-Axis Wind Turbines,” in *Wind Energy Engineering*, T. M. Letcher, Ed., Academic Press, 2017, pp. 161–184. doi: 10.1016/B978-0-12-809451-8.00009-6.

[6] A. Winslow, “Urban Wind Generation: Comparing Horizontal and Vertical Axis Wind Turbines at Clark University in Worcester, Massachusetts,” *Sustainability and Social Justice*, May 2017, [Online]. Available: https://commons.clarku.edu/idce_masters_papers/127

[7] F. Toja-Silva, A. Colmenar-Santos, and M. Castro-Gil, “Urban wind energy exploitation systems: Behaviour under multidirectional flow conditions—Opportunities and challenges,” *Renewable and Sustainable Energy Reviews*, vol. 24, pp. 364–378, Aug. 2013, doi: 10.1016/j.rser.2013.03.052.

[8] A. Pallotta, D. Pietrogiacomi, and G. P. Romano, “HYBRI – A combined Savonius-Darrieus wind turbine: Performances and flow fields,” *Energy*, vol. 191, p. 116433, Jan. 2020, doi: 10.1016/j.energy.2019.116433.

[9] S. Chegini, M. Asadbeigi, F. Ghafoorian, and M. Mehrpooya, “An investigation into the self-starting of darrieus-savonius hybrid wind turbine and performance enhancement through innovative deflectors: A CFD approach,” *Ocean Engineering*, vol. 287, p. 115910, Nov. 2023, doi: 10.1016/j.oceaneng.2023.115910.

[10] E. N. Irawan, S. Sitompul, K.-I. Yamashita, and G. Fujita, “Computational Fluid Dynamics Analysis on the Improvement of Hybrid Savonius-Darrieus NREL S809 at Various Fluid Flows,” in *2023 4th International Conference on High Voltage Engineering and Power Systems (ICHVEPS)*, Aug. 2023, pp. 389–394. doi: 10.1109/ICHVEPS58902.2023.10257308.

[11] M. I. Faraz, “Strategic analysis of wind energy potential and optimal turbine selection in Al-Jouf, Saudi Arabia,” *Heliyon*, vol. 10, no. 20, p. e39188, Oct. 2024, doi: 10.1016/j.heliyon.2024.e39188.

[12] I. Caglayan, I. Tikiz, A. C. Turkmen, C. Celik, and G. (Gulsen) Soyhan, “Analysis of wind energy potential; A case study of Kocaeli University campus,” *Fuel*, vol. 253, pp. 1333–1341, Oct. 2019, doi: 10.1016/j.fuel.2019.05.123.

[13] M. E. Emetere, “Chapter 8 - Numerical interpolation in environmental research,” in *Numerical Methods in Environmental Data Analysis*, M. E. Emetere, Ed., Elsevier, 2022, pp. 169–190. doi: 10.1016/B978-0-12-818971-9.00005-3.

[14] Z. Ma, G. Mei, and N. Xu, “Generative deep learning for data generation in natural hazard analysis: motivations, advances, challenges, and opportunities,” *Artif Intell Rev*, vol. 57, no. 6, p. 160, May 2024, doi: 10.1007/s10462-024-10764-9.

[15] B. Jiang, X. Zhu, X. Tian, W. Yi, and S. Wang, “Integrating Interpolation and Extrapolation: A Hybrid Predictive Framework for Supervised Learning,” *Applied Sciences*, vol. 14, no. 15, Art. no. 15, Jan. 2024, doi: 10.3390/app14156414.

[16] S. P. Venkateshan and P. Swaminathan, “Chapter 5 - Interpolation,” in *Computational Methods in Engineering*, S. P. Venkateshan and P. Swaminathan, Eds., Boston: Academic Press, 2014, pp. 213–254. doi: 10.1016/B978-0-12-416702-5.50005-3.

[17] “Interpolation and Polynomial Curve Fitting,” *ResearchGate*, Oct. 2024, doi: 10.5951/mathteacher.108.2.0132.

[18] X. Zou, “Chapter 3 - Interpolation,” in *Atmospheric Satellite Observations*, X. Zou, Ed., Academic Press, 2020, pp. 23–47. doi: 10.1016/B978-0-12-820950-9.00003-9.

[19] X. Che *et al.*, “Linearly interpolating missing values in time series helps little for land cover classification using recurrent or attention networks,” *ISPRS Journal of Photogrammetry and Remote Sensing*, vol. 212, pp. 73–95, Jun. 2024, doi: 10.1016/j.isprsjprs.2024.04.021.

[20] A. M. Bayen and T. Siauw, “Chapter 14 - Interpolation,” in *An Introduction to MATLAB® Programming and Numerical Methods for Engineers*, A. M. Bayen and T. Siauw, Eds., Boston: Academic Press, 2015, pp. 211–223. doi: 10.1016/B978-0-12-420228-3.00014-2.

[21] D. Abdullah *et al.*, “Application of Interpolation Image by using Bi-Cubic Algorithm,” *J. Phys.: Conf. Ser.*, vol. 1114, p. 012066, Nov. 2018, doi: 10.1088/1742-6596/1114/1/012066.

[22] “Beyond trilinear interpolation: higher quality for free,” *ResearchGate*, Oct. 2024, doi: 10.1145/3306346.3323032.

[23] C. Chen, N. Zhao, T. Yue, and J. Guo, “A generalization of inverse distance weighting method via kernel regression and its application to surface modeling,” *Arab J Geosci*, vol. 8, no. 9, pp. 6623–6633, Sep. 2015, doi: 10.1007/s12517-014-1717-z.

[24] B. J. Lewis, E. N. Onder, and A. A. Prudil, “Chapter 9 - Numerical analysis,” in *Advanced Mathematics for Engineering Students*, B. J. Lewis, E. N. Onder, and A. A. Prudil, Eds., Butterworth-Heinemann, 2022, pp. 265–285. doi: 10.1016/B978-0-12-823681-9.00017-4.

[25] J. Ogniewski, “Spline Interpolation in Real-Time Applications using Three Control Points,” in *Computer Science Research Notes*, Západočeská univerzita, 2019. doi: 10.24132/CSRN.2019.2901.1.1.

[26] F. Gensun, “Whittaker–Kotelnikov–Shannon Sampling Theorem and Aliasing Error,” *Journal of Approximation Theory*, vol. 85, no. 2, pp. 115–131, May 1996, doi: 10.1006/jath.1996.0033.

[27] T. P. Syawitri, Y. Yao, J. Yao, and B. Chandra, “Assessment of stress-blended eddy simulation model for accurate performance prediction of vertical axis wind turbine,” *International Journal of Numerical Methods for Heat & Fluid Flow*, vol. 31, no. 2, pp. 655–673, Jun. 2020, doi: 10.1108/HFF-09-2019-0689.

[28] M. M. Salah, A. G. Abo-khalil, and R. P. Praveen, “Wind speed characteristics and energy potential for selected sites in Saudi Arabia,” *Journal of King Saud University - Engineering Sciences*, vol. 33, no. 2, pp. 119–128, 2021, doi: 10.1016/j.jksues.2019.12.006.

[29] K. Franke, F. Sensfuß, G. Deac, C. Kleinschmitt, and M. Ragwitz, “Factors affecting the calculation of wind power potentials: A case study of China,” *Renewable and Sustainable Energy Reviews*, vol. 149, p. 111351, Oct. 2021, doi: 10.1016/j.rser.2021.111351.

CHAPTER 6
CONCLUSION AND FUTURE WORK

6.1 CONCLUSION

This research has successfully explored the development and optimization of Smart Hybrid vertical axis wind turbines (VAWTs) as a viable renewable energy solution. Through a combination of computational analysis, experimental validation, and real-world performance evaluation, this study has provided significant insights into the aerodynamics, efficiency, and adaptability of hybrid Savonius-Darrieus wind turbines.

The aerodynamic performance of the hybrid VAWT was analyzed using computational fluid dynamics (CFD), where simulations demonstrated a 26.91% increase in power coefficient at a tip speed ratio (TSR) of 1.45. However, efficiency declined at higher TSRs due to the aerodynamic limitations of the Savonius rotor. To address this, additional deflectors were introduced, resulting in an efficiency enhancement of 30% at an optimal TSR of 2.6.

Further experimental testing at high TSRs revealed that increasing the rotor radius ratio ($\frac{R_S}{R_D}$) improved self-starting capabilities but reduced the maximum power coefficient. The optimal rotor radius ratio was determined to be 0.5, achieving a 12.5% increase in power coefficient compared to a conventional Darrieus turbine. Additionally, experimental studies validated a 6.26% deviation from CFD results, confirming the reliability of the numerical simulations.

A key innovation in this study was the introduction of a switching rotor mechanism, which transitions between hybrid and single Darrieus modes based on wind conditions. This approach successfully optimized performance by preventing aerodynamic losses at high TSRs, leading to a 21% improvement in power coefficient compared to conventional hybrid models. Furthermore, the Smart Hybrid VAWT extended the TSR range beyond 3.3, significantly improving efficiency under fluctuating wind conditions.

To evaluate real-world applicability, a case study was conducted in Banjarmasin, Indonesia. The Smart Hybrid VAWT demonstrated 347.46% higher power output than traditional hybrid turbines. These results underscore the potential of Smart Hybrid VAWTs in regions with variable wind patterns.

6.2 FUTURE WORK

To further enhance the performance and applicability of Smart Hybrid VAWTs, several key areas of future research and development are proposed:

6.2.1 Implementation of Maximum Power Point Tracking (MPPT):

a) Integrating MPPT algorithms to optimize power extraction under varying wind conditions.

b) Developing adaptive control strategies for real-time tracking of optimal power coefficients.

6.2.2 Advanced Aerodynamic Optimization:

a) Exploring novel blade designs and flow control techniques to reduce drag and improve efficiency.

b) Utilizing active flow control mechanisms to enhance lift generation and power output.

6.2.3 AI-Driven Control Strategies:

a) Implementing machine learning algorithms for real-time turbine performance optimization.

b) Enhancing predictive maintenance capabilities to extend turbine lifespan and reliability.

6.2.4 Scalability and Field Deployment:

a) Conducting large-scale field tests to validate laboratory findings in real-world conditions.

b) Assessing the economic feasibility and environmental impact of Smart Hybrid VAWT deployment in various locations.

RESEARCH ACHIEVEMENTS

Throughout my doctoral studies, I have actively engaged in various research activities, including publications, conference presentations, and collaborative projects. These achievements reflect my dedication to advancing knowledge in the field of power systems and renewable energy integration. The following is a summary of my research contributions, which include journal articles, conference proceedings, and other scholarly engagements that have significantly shaped the outcomes of this thesis.

JOURNAL ARTICLES:

[J.1] E. N. Irawan, S. Sitompul, K.-I. Yamashita, and G. Fujita, "The Effect of Rotor Radius Ratio on The Performance of Hybrid Vertical Axis Wind Turbine Savonius-Darrieus NREL S809," Journal of Energy and Power Technology, vol. 5, no. 1, Art. no. 1, Jan. 2023, doi: 10.21926/jept.2301001.

[J.2] E. N. Irawan et al., "Analyzing the growth and trends of vertical axis wind turbine research: Insight from a bibliometric study," Journal of Mechatronics, Electrical Power, and Vehicular Technology, vol. 14, no. 1, Art. no. 1, Jul. 2023, doi: 10.14203/j.mev.2023.v14.55-61.

[J.3] E. N. Irawan, K. Shibuya, K.-I. Yamashita, and G. Fujita, "Unlocking the power of the wind: Innovations in smart hybrid vertical axis wind turbines," International Journal of Renewable Energy Development, vol. 13, no. 5, pp. 974–981, Sep. 2024, doi: 10.61435/ijred.2024.60354.

INTERNATIONAL CONFERENCE PROCEEDINGS

[C.1] E. N. Irawan, S. Sitompul, K.-I. Yamashita, and G. Fujita, "Computational Fluid Dynamics Analysis on the Improvement of Hybrid Savonius-Darrieus NREL S809 at Various Fluid Flows," in 2023 4th International Conference on High Voltage Engineering and Power Systems (ICHVEPS), Aug. 2023, pp. 389–394. doi: 10.1109/ICHVEPS58902.2023.10257308.

[C.2] E. N. Irawan et al., “Development of a Simple Open-Loop Wind Tunnel for Small-Scale Wind Turbine Testing,” in The 18th Southeast Asian Technical University Consortium (SEATUC), Feb. 2024, pp. 38–42.

[C.3] E. N. Irawan, K. Shibuya, K.-I. Yamashita, and G. Fujita, “Enhancing Vertical Axis Wind Turbine Performance Investigation at Low Wind Speed Using Electrical Approach,” in 2024 8th International Conference on Green Energy and Applications (ICGEA), Mar. 2024, pp. 1–5. doi: 10.1109/ICGEA60749.2024.10561142.

[C.4] E. N. Irawan, K. Shibuya, K.-I. Yamashita, and G. Fujita, “Solidity Effects on Small Hybrid Savonius-Darrieus Wind Turbine Performance: Experimental Analysis with NREL S809 Airfoil,” in 2024 10th International Conference on Applied System Innovation (ICASI), Apr. 2024, pp. 163–165. doi: 10.1109/ICASI60819.2024.10547931.

[C.5] E. Nensy Irawan, K.-I. Yamashita, and G. Fujita, “Comparison of Non-Overlap and Overlap Savonius Wind Turbines in the Physics Aspect Using Computational Fluid Dynamics Method,” J. Phys.: Conf. Ser., vol. 2780, no. 1, p. 012031, Jun. 2024, doi: 10.1088/1742-6596/2780/1/012031.

[C.6] E. N. Irawan, K.-I. Yamashita, and G. Fujita, “A Novel Rotor Switching Theory for Optimizing Small Vertical Axis Wind Turbine Performance: Insights from Experimental Study,” in 2024 International Conference on Electrical, Computer and Energy Technologies (ICECET, Jul. 2024, pp. 1–5. doi: 10.1109/ICECET61485.2024.10698090.

[C.7] E. N. Irawan, M. Miyagawa, M. Putra, K.-I. Yamashita, and G. Fujita, “Estimating Wind Energy Potential: Advanced Smart Hybrid VAWT Analysis in Banjarmasin, Indonesia,” in 2024 6th International Conference on Power Engineering and Renewable Energy (ICPERE), Nov. 2024, pp. 1–6. doi: 10.1109/ICPERE63447.2024.10845584.

AWARDS

[A.1] **Award** : Best Presentation

Conference Name : 3rd International Symposium on Physics and Applications 2023 (ISPA 2023)

Paper Title : Comparison of Non-Overlap and Overlap Savonius Wind Turbines in the Physics Aspect Using Computational Fluid Dynamics Method

Date Awarded : 2023/11/23

AUTHOR BIOGRAPHY

The author, born on January 27, 1997, is a young lecturer at the Indonesia University of Education (Universitas Pendidikan Indonesia), serving since October 2021. The academic journey began with undergraduate studies in Physics at Sepuluh Nopember Institute of Technology (ITS), Indonesia, in 2015. This was followed by a Master of Science degree in Physics from the same institution, awarded in 2021. In 2022, the author commenced doctoral studies at Shibaura Institute of Technology, Japan, in the Department of Functional Control Systems.

The author's doctoral research, titled "Advancing Hybrid Vertical Axis Wind Turbines: Computational, Experimental, and Smart Technology Innovations for Wind Energy Optimization," reflects a multidisciplinary approach combining computational fluid dynamics, experimental validation, and smart control systems to enhance wind energy performance. The research outcomes have been published in peer-reviewed journals and presented at international conferences in the fields of renewable energy and control engineering.

Throughout the academic and professional career, the author has also contributed to several innovative projects, resulting in multiple patent publications related to smart energy systems, AI-driven fatigue and mental health monitoring, and vertical axis wind turbine optimization. In recognition of academic excellence and impactful research, the author has received several accolades, including the Best Presentation Award at the 3rd International Symposium on Physics and Applications (ISPA 2023), and First Prize in the National Scientific Essay Competition "Event of Gold Generation" (2020). With a strong foundation in both theoretical and applied sciences, the author continues to contribute to the advancement of sustainable technologies and science education.